UNIVERSIDADE FEDERAL DO RIO GRANDE DO SUL

INSTITUTO DE FÍSICA

Design of Integrable Quantum Devices

Daniel Schneider Grün

Dissertation submitted in partial fulfillment of the
requirements for the degree of
Master in Science.
Supervisor: Prof. Dr. Angela Foerster
Co-supervisor: Prof. Dr. Leandro Hayato Ymai

Porto Alegre - RS

August, 2021

Agradecimentos

Sinto, ao mesmo tempo, desconforto e euforia ao saber que o maior mistério de todos - o da existência - eu jamais poderei desvendar. Aqui me resta a Fé. Com ela, agradeço Àquele que É: pelo que há.

Muitas são as pessoas que merecem meu reconhecimento e minha gratidão. Devo iniciar agradecendo à Vitória, minha esposa, pelo carinho, companheirismo, paciência e amor. Aprendi (e aprendo) muito contigo, e sou grato a Deus pela tua disposição em fazer parte das minhas loucuras. Te amo.

Aos meus pais, Egídio e Joana, e aos meus irmãos, Thalita e Felipe, que sempre me ampararam e estiveram prontos a me ajudar em qualquer instante: vocês são exemplo de amor e perdão para mim, e eu agradeço profundamente a vocês por todo o suporte material e emocional durante estes anos. Amo vocês.

Agradeço também à minha orientadora, Profª. Angela, ao meu coorientador, Prof. Leandro, e a todos os integrantes do grupo de Física Matemática. Vocês permitiram que eu desse os primeiros passos rumo à investigação de forma independente e curiosa, e eu agradeço muito pelos ensinamentos que propiciaram meu desenvolvimento pessoal e intelectual.

Sou profundamente grato aos meus colegas e amigos (não vou citar nomes para não esquecer de ninguém), com quem dividi momentos de tristeza e alegria. Esperar pelo dia do vôlei valia a pena por causa de vocês.

I am also deeply grateful to Prof. Francesca Ferlaino, from Universität Innsbruck, for my warm welcoming in the Erbium Group as an international Master's Student. The opportunity you gave me is invaluable, and I will never forget (God help me) everything I learned while I was under your supervision. Thank you for letting me work in the lab :)

My time in Innsbruck was mainly divided between the lab and Kolpinghaus. At both places, I met incredible people to whom I'm grateful for the friendship and for the funny moments. With you guys, I would hike in the ice, have warm beer and play volleyball for a short time - I'm happy we did all of this.

Gabriele and Alex: thank you for everything you guys taught me. I hope some day I become as good an experimental physicist as you guys are.

Resumo

Apresentamos um modelo integrável de quatro poços que descreve a interação e o tunelamento quântico de bósons em uma plaqueta quadrada. Esse modelo apresenta quatro quantidades conservadas e independentes, das quais duas podem ser empregadas para derivar um Hamiltoniano efetivo. Com isso, é possível derivar fórmulas analíticas para a dinâmica quântica, contanto que a energia do sistema esteja em uma região de formação de bandas (o que chamamos "regime ressonante"). Empregando o Hamiltoniano efetivo, pode-se prever analiticamente tanto a atividade interferométrica do sistema, com a possibilidade de alcançar sensitividade de Heisenberg, quanto o uso do sistema como um gerador de estados NOON com codificação arbitrária de fase (através de quebra de integrabilidade). Então, calculamos os parâmetros do Hamiltoniano, demonstrando a equivalência entre esse modelo e o já conhecido Hamiltoniano de Bose-Hubbard extendido, quando este satisfaz uma condição especial entre o termo de interação interna a um poço e o termo de interação entre poços diagonais. Assim, providenciamos um possível design para o sistema de forma a demonstrar sua viabilidade experimental. Com os parâmetros calculados, nós mostramos que, sob condições ideais, o sistema pode alcançar altas fidelidades na geração do estado NOON e alta correspondência nas probabilidades dos procedimentos de leitura dos estados, comparando os valores numéricos obtidos com o Hamiltoniano de Bose-Hubbard extendido e as expressões analíticas obtidos com o Hamiltoniano efetivo. Espera-se que os resultados apresentados aqui abram novos caminhos na interação entre integrabilidade e atomotrônica.

Abstract

We present an integrable four-well model that describes the interaction and quantum tunneling of bosons in a square plaquette. This model possesses four conserved and independent quantities, of which two can be employed to derive an effective Hamiltonian. This allows for the derivation of analytical formulae for the quantum dynamics, provided that the system's energy is in a band-formation region (which we call "resonant regime"). By employing the effective hamiltonian, we analytically predict both the interferometric activity of the system, with the possibility of achieving Heisenberg sensitivity, and the employment of the system as a NOON state generator with arbitrary phase-encoding (through breaking of integrability). Then, we calculate the hamiltonian parameters, demonstrating the equivalency between this model and the already known extended Bose-Hubbard hamiltonian, when the latter satisfies a special condition between its onsite and second-nearest-neighbors interaction terms. Thus, we provide a possible design for the system to demonstrate its experimental feasibility. With the calculated parameters, we show that, under ideal conditions, the system can achieve high fidelities in the NOON state generation and high probability-matching in the read-out procedures, by comparing the numerical results obtained with the Extended Bose-Hubbard hamiltonian and the analytical results obtained with the effective hamiltonian. The findings presented here are expected to open new avenues in the interplay between integrability and atomtronics.

Press release

Os dispositivos que utilizamos - desktops, notebooks, celulares etc. - tiverem seu desenvolvimento baseado nas leis da Mecânica Quântica. Com a sua formulação, foi possível descrever o comportamento conjunto de vários elétrons em um sólido. No caso de um material semicondutor (como é o caso do silício), é possível manipular o comportamento destes elétrons e criar os chamados "transistores", que têm a função de relacionar uma corrente elétrica na placa do computador com uma unidade de informação - 0 ou 1. Este desenvolvimento tecnológico culminou na "primeira revolução quântica": embora a descrição e manipulação do material em questão dependa do conhecimento acerca das leis da Mecânica Quântica, a informação que é gerada, armazenada e transmitida é totalmente "clássica" - isto é, não quântica.

A "segunda revolução quântica", momento que estamos vivendo atualmente, surgiu como uma forma de tentar realizar cálculos, processos de medida e transmissão de informação de forma completamente "quântica". A ideia por trás disso está na noção de "superposição de estados" - o que significa que um dado sistema apresenta duas ou mais configurações simultâneas. Ao realizar uma medida sobre o sistema, este adquire uma das configurações possíveis. Estas propriedades permitem que dispositivos quânticos sensíveis sejam desenvolvidos, como, por exemplo, detectores de campo magnéticos e interferômetros. Diferente do que foi feito na "primeira revolução quântica", outras plataformas (além de placas de silício) estão sendo investigadas para a construção destes dispositivos. Entre elas, destaca-se a "atomotrônica", que busca utilizar os átomos (ao invés de elétrons) para compor a unidade fundamental da informação.

Átomos - em conjunto ou individualmente - podem ser desacelerados e aprisionados com potentes lasers, formando um sistema composto do que chamamos de "átomos ultrafrios". Ao fazer isso, propriedades que vão desde desde a estrutura interna destes até o seu movimento tornam-se acessíveis e manipuláveis em laboratório. Dentre as configurações em que pode-se colocar o feixe de laser encontra-se a "rede ótica", que é formada quando um laser é direcionado em um espelho de forma completamente perpendicular a este, o que gera uma estrutura cristalina feita de luz, permitindo um alto controle sobre o movimento e a interação dos átomos. Com isso, pode-se construir dispositivos atomotrônicos com propriedades semelhantes aos dispositivos eletrônicos, mas com maior grau de controle e sensibilidade. Entre estes dispositivos, destaca-se o "interferômetro".

A técnica de interferometria consiste em verificar interferências construtivas e destrutivas em uma onda resultante da soma de duas ondas. Geralmente, esta onda é eletromagnética, já que os interferômetros costumam ser feitos de luz (como por exemplo o LIGO, que detecta ondas gravitacionais através deste método). Entretanto, de acordo com a Mecânica Quântica, toda a matéria possui, em certo grau, *comportamento* ondulatório. Tal propriedade permite que átomos também sejam utilizados, o que pode ser muito vantajoso. Diferentemente de fótons - as partículas associadas à luz -, átomos possuem massa, o que os tornam mais sensíveis a certos efeitos (por exemplo, em medidas de campos gravitacionais fracos).

Neste trabalho, exploramos possibilidades de se realizar interferometria com sistemas atomotrônicos com a maior sensibilidade permitida pela natureza - limitada pelo Princípio da Incerteza de Heisenberg. Para isto, estudamos um modelo quântico que descreve o movimento e a interação de átomos bosônicos entre quatro poços. Este modelo também apresenta a propriedade de "integrabilidade", que permite que equações analíticas para a dinâmica quântica dos átomos sejam desenvolvidas. Ao final, apresentamos uma possível realização experimental para o modelo, conectando o modelo estudado com o aprisionamento via feixes de laser e calculando explicitamente os valores resultantes para a intensidade com que os átomos se movimentam e interagem entre si.

Press release

The devices we use - desktops, laptops, cell phones, etc. - had their development based on the laws of Quantum Mechanics. Due to its formulation, it was possible to describe the group behavior of several electrons in a solid. In the case of a semiconductor (silicon, for example), one can manipulate the behavior of these electrons and create the so-called "transistors", whose function is to relate an electric current on the computer circuit with a unit of information - 1 or 0. This technological development culminated in the "first quantum revolution": although the description and manipulation of a given material depend on the knowledge regarding the laws of Quantum Mechanics, the information that is generated, stored and transmitted is totally "classical" - i.e., not quantum.

The "second quantum revolution" that we are currently living emerged as a way to engage on calculations, measurement processes, and information transmission on a completely "quantum" basis. The idea behind it relies on the notion of "state superposition" - which means that a given system simultaneously presents two or more different configurations. When an attempt to measure the system is made, it acquires one of the possible configurations. These properties allow for the development of sensitive quantum devices, as, for example, magnetic-field detectors and interferometers. Differently from what happened in the "first quantum revolution", other platforms (besides the silicon wafers) are being investigated for the construction of such devices. Amongst them, we highlight the "atomtronics", which intends to use atoms (instead of electrons) for making-up the fundamental unit of information.

Atoms - individually or as an ensamble - can be slowed down and trapped with powerful laser beams, resulting in a system composed of what we call "ultracold atoms". At this point, properties beyond their internal structure become accessible and manipulable in the lab. One of the configurations in which a laser beam can be employed is the "optical lattice", which is generated when a beam is directed towards a mirror, arriving perpendicularly to its surface, giving raise to a crystal-like structure made up of light, allowing for a high level of control on the movement and interaction of the atoms. This allows for the construction of atomtronic devices that present similar properties to electronics, but with a higher degree of control and sensitivity. Amongst these devices, we highlight the "interferometer".

Interferometry is a technique that consists of the verification of constructive and destructive interferences on a wave that results from the sum of other two waves. Usually, this wave is of the electromagnetic kind, since the interferometers tend to work with light (as, for example, the LIGO, which detects gravitational waves with this method). However, according to Quantum Mechanics, all matter possesses, up to a certain degree, wave-*like behavior*. Such property enables atoms to be used on interferometry, too, which comes with certain advantages. Differently that photons - the particles associated with light -, atoms have mass, making them more sensitive to certain effects (for example, in measurements of weak gravitational fields).

In this work, we explore possibilities of realizing interferometry on atomtronics systems with the highest sensitivity allowed by nature - limited by the Heisenberg's Uncertainty Principle itself. For this, we study a quantum model that describes the movement and interaction of bosonic atoms between four wells. This model also presents the property of "integrability", which allows for the development of analytical equations for the system's quantum dynamics. In the end, we present a possible experimental realization of the model, linking it with a laser-trapped atomic configurations and calculating the resulting values explicitly for the intensities of the atomic movement and interaction.

"(...) et ex Patre natum ante omnia sæcula."
Symbolum Nicænum

Contents

Chapter 1

Introduction

Se a meta principal de um capitão fosse preservar seu barco,
ele o conservaria no porto para sempre.
– São Tomás de Aquino

In research labs around the world, hadrons are daily smashed against each other on high-energy processes and atoms and molecules are spatially trapped and cooled down to highly denegerate configurations. Although contrasting at first, these pictures exemplify the ability of Quantum Mechanics, one of the most specifically tested theories in the history of science, in describing nature (in the low-mass regime) down to the (sub)atomic level.

Among the predictions made by the quantum theory, the ones from Bose [1] and Einstein [2] are within the most prominent ones for the investigation of several properties of light, matter and information. Being a consequence of the statistical distribution of bosons (particles with integer spin, whose complete wavefunction has even parity), the Bose-Einstein Condensate (BEC) is expected to occur from a phase-transition when all the particles go to the same ground-state of a given potential. In the context of a grand-canonical statistical description, this means that the temperature T of the sample should approach 0K. Although relatively simple in conceptualization, it was not until roughly seventy years after their prediction that the first BEC's were experimentally confirmed in Boulder, by Cornell and Wieman [3], and in the MIT, by Ketterle [4], for which they ended up winning the 2001 Physics Nobel Prize. To achieve this, previously-developed laser-cooling systems and trapping schemes had to be employed in order to reach the low temperatures required ($\sim$ 170 nK for ^{87}Rb). Some of these developments had already resulted in Cohen-Tannoudji, Chu and Phillips winning the Physics Nobel Prize in 1997.

Since their first observation, a complete new range of experiments with BECs have been realized. Amongst them, we highlight an experiment from the group of Oberthaler in Heidelberg [5], where a bosonic Josephson-junction and the nonlinear self-trapping regime were observed for the first time on a system composed of two BECs on a double-well potential. These effects are qualitatively well described by a Bose-Hubbard (BH) model [6, 7, 8] of two sites. Such a model has been thoroughly used to describe certain features in experiments of cold atoms in optical lattices - such as the phase-transition from superfluid to Mott Insulator (SF to MI) [9] and matter-wave dynamical collapses [10].

However, another interesting characteristics of the BH model is the fact that it is integrable in the two-site configuration.

The first notions of quantum integrability seem to have originated with Schrödinger's first papers [11, 12] on "his" Wave Mechanics. In these works, Schrödinger treats the quantization as an eigenvalue problem and exactly solves the just-demonstrated wave equation for several different potentials - amongst which the non-relativistic hydrogen atom. The studied examples were all (approximately) composed of one particle in the presence of a potential - therefore constituting one-body systems. When it comes to several particles, however, it is much harder to come up with exact solutions that describe the systems. The Heisenberg model encounters itself within the ones that allow for such treatment. Especially important for studies on magnetism, this model describes a system of interacting spins in the presence of a magnetic field, having been employed, for example, in the investigation of quantum phase-transitions at finite temperature [13] and criticality [14]. Such a many-body configuration was shown by Bethe to be exactly solvable [15] and, since then, the "Bethe ansatz" has been employed in order to obtain the eigenstates and eigenvalues of a Bethe-ansatz-solvable model, constituting a self-consistent category of integrable models. Motivated by such a breakthrough, other researchers [16, 17, 18, 19] engaged in the development of the field of exactly-solved models, which nowadays spans different areas of physics - from statistical mechanics [19] and field theory [20, 21] to condensed-matter physics [22, 23] and ultracold atoms [24], among others.

In atomic, molecular and optical (AMO) physics, the so-called "Quantum inverse scattering method" (QISM) has been employed to solve the two-site Bose-Hubbard model in terms of its eigenstates and energies [25, 26], with the predicted phase-transitions being associated with the anomalous behavior of the Bethe-ansatz equations' (BAE) solutions [27] [1]. Since the BH model is not integrable in the configuration with $n > 2$ sites, a new family of models was proposed to study the dynamics between multiple wells [31]. This required an extension of the QISM in order for all the system's energies to be found, and also enabled the model's completeness through the obtention of the whole set of independent conserved quantities. Within these models, one particular example is the one describing the quantum tunneling between three wells [32], which was shown to work as a switching device with analogical control [33], indicating integrability as a benefical approach for prototyping atom-based quantum devices.

The advent of quantum mechanics enabled the development of accurate and reliable modelling of technological components, which allowed for the emergence of devices such as transistors [34] and lasers [35], culminating into a technological revolution in the twentieth century. The technologies that came forth, however, would still rely on the classical use of information [36], therefore not fully harnessing the power of quantum mechanics. Nowadays, we are living the first stages of the second quantum revolution, with the aim of building actual quantum technologies [37]. Although not yet completely understood, its potential applications vary from faster algorithms on quantum computations [38] to simulating many-body quantum systems themselves [39]. Ultracold-atomic systems have been shown to potentially realize such applications [40, 41], accounting for a milestone in the advancement

[1] We observe that integrable models for atomic-molecular BECs have also been solved in this context, see for instance [28, 29, 30]

of technology towards a quantum-equivalent to classical systems. This constitutes the idea behind the so-called atomtronics, a field emerged from investigations of atom analogs for electronic devices [42] that is currently regarded as a suitable platform for a diverse range of applications [43, 44, 45] - as atomic SQUIDs (superconducting quantum interference devices) [46] and gravimeters [47], for example.

By going further in the merging of integrability and atomtronics [33], in this Dissertation we present two interferometric-related quantum-device applications for an integrable four-well model [48]. The Dissertation is divided in the following structure:

- Chapter 2 briefly reviews some concepts of classical and quantum integrability and introduces the model and its properties;
- Chapter 3 introduces the possible applications of the model as a quantum device, with analytical descriptions and numerical verifications on the fidelities and probabilities of the generated quantum states;
- Chapter 4 develops the entanglement-entropy properties of the four-well system;
- Chapter 5 presents the extended Bose-Hubbard Hamiltonian and, by comparing it with the integrable model, arrives at the conditions for integrability;
- Chapter 6 develops an idea for possible experimental realization of the quantum device based on existing experiments and for a specific atomic species, and the proposed setup is employed for the calculation of the Hamiltonian parameters;
- Chapter 7 presents some experimental results on beam-displacement at the Fourier plane with a Digital Micromirror Device, which is related to the nondestructive measurement proposed in Chapter 6;
- Chapter 8 synthetizes the main results and conclusions of this Dissertation.

Chapter 2

Four-well integrable model

The four-well integrable model, obtained by an extension of the Quantum Inverse Scattering Method, allows for analytical results of the system's quantum dynamics to be found. In this chapter, the model is introduced as we discuss its independent and conserved quantitites and the role they play on the quantum dynamics. The numerical evaluation of quantities related to the system's dynamics was performed using the Python package "cfwell"[1] developed by myself.

2.1 Integrability Overview

Classical integrability has had a clear definition since the 19th Century, when Poisson and Liouville (in 1837 and 1840, respectively) specifically demonstrated that a hamiltonian system, having two degrees of freedom, should also posess two constants of motion in involution, such that the equations of motion for the system should be solvable through the method of Quadratures. Such a framework is widely accepted, since its axiomatization proves it unequivocal.

Classical and Quantum physics, however, have some profound differences. The own Hamiltonian structure, completely different when comparing classical and quantum algebra, imposes contrasts between the two descriptions - although a (semi)classical treatment of expected values may give raise to possibilities of control [33] and even reveal features such as quantum phase-transitions [49, 50]. Differently than what happens in Classical physics, Quantum Integrability is a subject without a unique definition. With this, different definitions of quantum integrability happened to appear in the course of time [51].

In this work, we make use of the definition that we think most resembles the classical axioms imposed by the Liouville Theorem - which states that a system with n degrees of freedom is integrable if it has the same amount n of independent conserved quantities.

[1] https://github.com/danielsgrun/cfwell

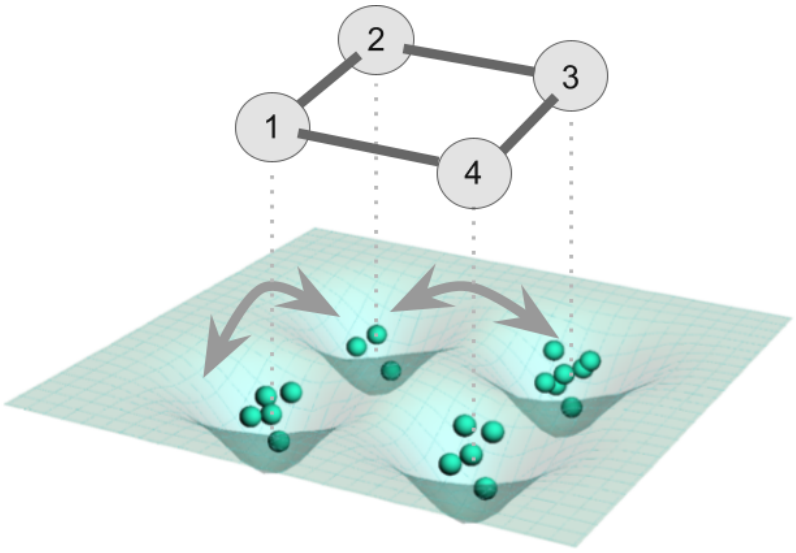

Figure 2.1: Four-well integrable model. The particles are restricted to four different sites (or "wells"), depicted as the four enumerated spheres. Sites "1 and 3" constitute "Class A", whereas sites "2 and 4" constitute "Class B". The solid lines connecting the wells represent the hopping terms of the Hamiltonian of Eq. 2.2.2. There is no direct hopping between sites of the same class.

2.2 INTEGRABLE HAMILTONIAN

The four-well integrable model [48] is part of a larger family of multi-well quantum tunneling integrable models [31, 52], that describes the interaction and tunneling of bosons between $n+m$ wells. The Hamiltonian has a generalized bipartite structure: N_A atoms are distributed in n sites that belong to a specific set (class A), while N_B atoms are distributed in m sites of class B. The atoms do not tunnel (as a first-order state transition) within a class. The Equation 2.2.1 summarizes it while considering that the system has isotropic tunneling and a constant total number of particles N.

$$H = -U(N_A - N_B)^2 - \frac{J}{2}\sum_{i=1}^{n}\sum_{j=1}^{m}(a_i^\dagger b_j + a_i b_j^\dagger). \tag{2.2.1}$$

Above, U is the interaction parameter, $N_A = \sum_{i=1}^{n} N_{a,i}$ and $N_B = \sum_{j=1}^{m} N_{b,j}$, where $N_{a,i}$ and $N_{b,j}$ are, respectively, the number operator for the i-th site of class A and j-th site of class B. The term $J/2$ represents the hopping coupling, with $a_i, b_j^\dagger$ being, respectively, the annihilation operator for the i-th site of class A and the creation operator for the j-th site of class B. Through different choices of n and m, one may recover the Hamiltonians of known models, such as the two-well [8, 53, 54] ($n = m = 1$) and three-well [33] ($n = 2$, $m = 1$) models. By setting $n = m = 2$, we arrive with the (closed) four-well model:

$$H = -U(N_1 + N_3 - N_2 - N_4)^2 - \frac{J}{2}\left[(a_1^\dagger + a_3^\dagger)(a_2 + a_4) + (a_1 + a_3)(a_2^\dagger + a_4^\dagger)\right], \tag{2.2.2}$$

Fig. 2.1 illustrates the model.

2.2.1 Conserved quantities

From an extension of the Quantum Inverse Scattering Method (see, for instance, [48]), it is possible to find the four conserved and independent quantities of the four-well integrable model. Besides the two trivial ones - the hamiltonian H and the total number of particles N -, the system also has two "extra" conserved quantities - Q_1 and Q_2 -, called "conserved charges", whose expressions are given by:

$$\begin{aligned} Q_1 &= \frac{1}{2}\left[N_1 + N_3 - a_1^\dagger a_3 - a_1 a_3^\dagger\right]; \\ Q_2 &= \frac{1}{2}\left[N_2 + N_4 - a_2^\dagger a_4 - a_2 a_4^\dagger\right], \end{aligned} \tag{2.2.3}$$

where they satisfy

$$[H, Q_i] = [N, Q_j] = [Q_i, Q_j] = 0, \tag{2.2.4}$$

such that the system has four conserved quantities that commute among themselves, which characterizes the quantum equivalence of the classical involution demanded by Liouville's theorem.

An analysis of Eq. 2.2.3 reveals a tunneling structure that is different than the one expected from the Hamiltonian of Eq. 2.2.2. This leads to the physical interpretation of the charges as dynamically equivalent to the system's Hamiltonian (depending on the choice of parameters and initial state for the system). This will be thoroughly explored in the Section 2.3.

2.2.2 Resonant regime

By varying both the interaction (U) and the hopping (J) terms, the four-well integrable model is able to achieve different dynamical regimes. Such regimes are related to the model's energy distribution due to the formation of energy bands when the hamiltonian's eigenvalues are varied by changing U (keeping J constant). Here, we will pay special attention to the condition $UN/J \gg 1$. In this case, the expected values $\langle N_1 + N_3\rangle$ and $\langle N_2 + N_4\rangle$ do not change in time due to second-order tunneling (a demonstration in terms of semiclassical analysis can be found in [32, 33, 55]), and the energies coalesce into well-defined bands that correspond to the possible values of $N_1 + N_3$ and $N_2 + N_4$ on the initial state.

Hereby, the definitions $\langle N_1(0) + N_3(0)\rangle \equiv M$ and $\langle N_2(0) + N_4(0)\rangle \equiv P$ are made, making it possible to analyze the system in the context of resonant tunneling in a convenient manner. Figure 2.2 **(a)** demonstrates the band formation in the system with $N = 15$ and $J = 70$, for U in the interval $[0, 120]$. By analyzing the figure, one realizes that the energies start to coalesce into bands with the increase of the ratio $\chi \equiv U/J$, up to the point ($U/J \approx 0.5$) where the energies split into $(N+1)/2$ regions. These correspond ultimately to the 8 possible initial distributions of bosons between the classes "A" and "B" that effectively change the interaction energy of the hamiltonian of Eq. 2.2.2.

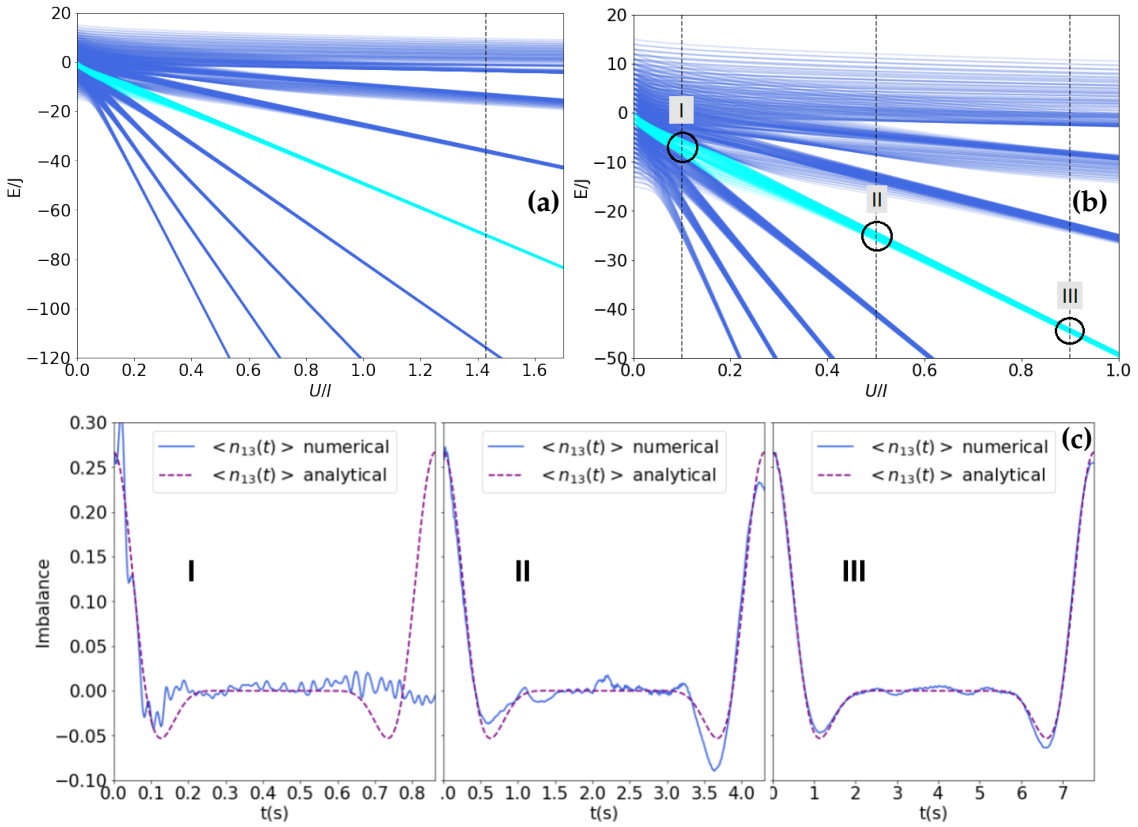

Figure 2.2: Energies of the four-well integrable model for $N = 15$, $J = 70$ and U varying from 0 to 120. For each value of U, the hamiltonian's eigenvalues were evaluated from direct diagonalization. The cyan energy-band depicts the energies for the initial state $|\Psi_0\rangle = |4,11,0,0\rangle$. On panel **(a)**, one sees the full picture of the system's energy band formation, with the dotted dashed grey line characterizing the usual choice of parameters $U/J \approx 1.42$. One can easily notice that the energies coalesce into eight different regions, accounting for each possible pure initial state $|\Psi_0\rangle$ related to different values of $\langle\Psi_0|H|\Psi_0\rangle$. The most negative energy is obtained with $N_A(0) = 15$ or $N_B(0) = 15$, whereas the less negative energy (and the one with a broader, in-formation band) is obtained with $N_A(0) = 8, N_B(0) = 7$ (or vice-versa). On panel **(b)**, the same figure is shown zoomed within a smaller region around $U/J = 0.5$. Here, one sees that the eight-region-energy-splitting fully starts taking place at $\sim U/J = 0.5$ (dashed gray line, region II). **(c)** Comparison between numerically-calculated quantum dynamics of $\langle n_{13}(t)\rangle \equiv 1/N\,\langle(N_1 - N_3)(t)\rangle$ and the analytical predictions of Eq. 2.4.4 for $|\Psi_0\rangle = |M,P,0,0\rangle$, with $M = 4$, $P = 11$, at the three different regions highlighted in panel **(b)**.

2.3 EFFECTIVE HAMILTONIAN

Similarly to the three-well case [56], the conserved charges of the four-well model also function as an effective hamiltonian when the system is on the resonant regime. For generalization, we may write the effective hamiltonian H_{eff} as:

$$H_{eff} = \lambda_1 Q_1 + \lambda_2 Q_2 + \lambda_{12} Q_1 Q_2. \tag{2.3.1}$$

The coefficients λ_1, λ_2 and λ_{12} depend ultimately on the hamiltonian parameters and the initial state and can be obtained through time-dependent perturbation theory (TDPT) treatment of the model. The charges Q_1 and Q_2 account, respectively, for the resonant transition of one particle between the sites of classes "A" *or* "B", respectively, while the term $\propto Q_1 Q_2$ is related to the *simultaneous resonant tunneling* between sites $1 \leftrightarrow 3$ and $2 \leftrightarrow 4$. Therefore, it is necessary to take three different state-transitions into account:

$$\begin{aligned}
|M-l,P-k,l,k\rangle &\rightarrow |M-l-1,P-k,l+1,k\rangle \\
|M-l,P-k,l,k\rangle &\rightarrow |M-l,P-k-1,l,k+1\rangle \\
|M-l,P-k,l,k\rangle &\rightarrow |M-l-1,P-k-1,l+1,k+1\rangle
\end{aligned} \tag{2.3.2}$$

We notice that, for any of the aformentioned state-transitions, the first order TDPT with the hamiltonian H (Eq. 2.2.2) vanishes, while it is nonzero for the effective hamiltonian H_{eff} (Eq. 2.3.1). Therefore, in order to compare the lowest nonzero orders of perturbation of both hamiltonians, we consider that, in the resonant regime, the second-order transition of H must be equal to the first-order transition of H_{eff} for the state-transitions given by Eq. 2.3.2. Such calculation demands a few lines of algebra, which is thoroughly presented in [57]. This results in analytical expressions for the coefficients λ_1, λ_2 and λ_{12}, given by:

$$\begin{aligned}
\lambda_1 &= \lambda_2 = (N+1)\Omega, \\
\lambda_{12} &= -2\Omega,
\end{aligned}$$

where Ω is defined as follows:

$$\Omega \equiv \frac{J^2}{4U\left[(M-P)^2-1\right]}. \tag{2.3.3}$$

By analyzing Eq. 2.3.3, one sees that the expression for Ω depends both on the hamiltonian parameters U, J and also on the initial distribution of bosons in classes A (M) and B (P). Now, we will show that it is possible to come up with analytical formulae for the system's quantum dynamics based on the expressions presented for the effective hamiltonian.

2.4 QUANTUM DYNAMICS

In this section, we demonstrate how to obtain analytical formulae for the quantum dynamics of the integrable four-well model. These are always obtained by employing the effective hamiltonian H_{eff}, which is dynamically equivalent to the "original" hamiltonian H when the system is on the resonant regime. For this, we will make use of the eigenbasis of the conserved charges Q_1 and Q_2 for our analysis. Denoting it by $\{|M,P,q_1,q_2\}\}$, we write these states in terms of the sites Fock states as:

$$|M,P,q_1,q_2\} = \frac{C}{2^N}\left(a_1^\dagger + a_3^\dagger\right)^{M-q_1}\left(a_1^\dagger - a_3^\dagger\right)^{q_1}\left(a_2^\dagger + a_4^\dagger\right)^{P-q_2}\left(a_2^\dagger - a_4^\dagger\right)^{q_2}|0\rangle\,, \tag{2.4.1}$$

such that $C = \frac{1}{\sqrt{q_1!(M-q_1)!q_2!(P-q_2)!}}$ is the normalization factor, and $H_{eff}|M,P,q_1,q_2\} = \mathfrak{e}_{q_1,q_2}|M,P,q_1,q_2\}$, where the energy eigenvalues of the effective hamiltonian are given by:

$$\mathfrak{e}_{q_1,q_2} = (N+1)\Omega(q_1+q_2) - 2\Omega q_1 q_2. \tag{2.4.2}$$

With this, we can calculate analytically the system's quantum dynamics. Only the main intermediate results of the demonstration will be shown in this subsection, and more details can be found in Appendix A.1.

We begin by evaluating the expressions of $(N_1-N_3)(t)$, $(N_2-N_4)(t)$ and their square. This will serve as a starting point for calculating both the quantum dynamics and the variance of the imbalances (N_1-N_3) and (N_2-N_4). By decomposing the effective hamiltonian in terms of its eigenvectors and eigenvalues, the aforementioned expressions can be evaluated within the Heisenberg Picture:

$$\begin{aligned}(N_1-N_3)(t) &= e^{-iH_{eff}t/\hbar}(N_1-N_3)e^{iH_{eff}t/\hbar}\\ &= \sum_{q_1=0}^{M}\sum_{q_2=0}^{P}\Bigg(e^{-i(\mathfrak{e}_{q_1,q_2}-\mathfrak{e}_{q_1-1,q_2})t/\hbar}\sqrt{q_1(M-q_1+1)}|N,P,q_1-1,q_2\}\\ &\qquad + e^{-i(\mathfrak{e}_{q_1,q_2}-\mathfrak{e}_{q_1+1,q_2})t/\hbar}\sqrt{(M-q_1)(q_1+1)}|N,p,q_1+1,q_2\}\Bigg)\{N,P,q_1,q_2|,\end{aligned} \tag{2.4.3}$$

where the same holds for the population imbalance between sites 2 and 4 through the exchange $M \leftrightarrow P$. Then, supposing an initial state given by $|\Psi_0\rangle = |M,P,0,0\rangle$, the quantum dynamics can be calculated through $\langle N_1-N_3\rangle(t) = \langle\Psi_0|(N_1-N_3)(t)|\Psi_0\rangle$. Using the expression from Eq. 2.4.3 and its equivalent for $(N_2-N_4)(t)$, we obtain:

$$\begin{aligned}\langle N_1 - N_3\rangle(t) =& M\cos\left[(M+1)\left(\frac{\Omega t}{\hbar}\right)\right]\left[\cos\left(\frac{\Omega t}{\hbar}\right)\right]^P \\ \langle N_2 - N_4\rangle(t) =& P\cos\left[(P+1)\left(\frac{\Omega t}{\hbar}\right)\right]\left[\cos\left(\frac{\Omega t}{\hbar}\right)\right]^M.\end{aligned} \tag{2.4.4}$$

In panel **(c)** of Fig. 2.2, it is possible to see that, as (U/J) approaches a region with band-coalescing energies for an initial state given by $|\Psi_0\rangle = |M,P,0,0\rangle$, with $M = 4$ and $P = 11$, the analytical dynamics from Eq. 2.4.4 and the numerical dynamics using the hamiltonian H of Eq. 2.2.2 start to become similar, which characterizes a resonant tunneling regime. Now, considering an entangled initial state given by $|\Psi_0\rangle = \frac{1}{\sqrt{2}}\left[|M,P,0,0\rangle + \exp(i\phi)\,|M,0,0,P\rangle\right]$, we calculate the expressions for quantum dynamics and fluctuations of the population imbalances. Defining $n_i \equiv N_i/N$, we obtain:

$$\begin{aligned}\langle n_1 - n_3\rangle(t) \equiv \langle n_{13}(t)\rangle =& \frac{M}{N}\cos[(M+1)\Omega t/\hbar][\cos(\Omega t/\hbar)]^P \\ &+ \frac{M}{N}\cos(\phi)[\sin(\Omega t/\hbar)]^P\cos\left[(M+1)\Omega t/\hbar + \frac{P\pi}{2}\right];\end{aligned} \tag{2.4.5}$$

$$\begin{aligned}\langle (n_1 - n_3)^2(t)\rangle \equiv \langle n_{13}^2(t)\rangle =& \frac{M}{2N^2}\left\{(M+1) + (M-1)\cos\left[2(M+1)\Omega t/\hbar\right][\cos(2\Omega t/\hbar)]^P\right\} \\ &+ \frac{M(M-1)}{2N^2}\cos\left[2(M+1)\Omega t/\hbar + \frac{\pi}{2}P\right][\sin(2\Omega t/\hbar)]^P\cos\phi.\end{aligned} \tag{2.4.6}$$

As we will see in Chapter 3, the expressions of Equations 2.4.5 and 2.4.6 are of huge importance to characterize the interferometric sensitivity contained in the four-well integrable model. By choosing $U/\hbar = 100$ Hz, $J/\hbar = 70$ Hz (such that $U/J \approx 1.42$), $M = 4$, $P = 11$ and $\phi = \pi/4$, it is possible to show that the numerical dynamics and fluctuations obtained with hamiltonian H become similar to the analytical ones, for an initial state given by $|\Psi_0\rangle = 1/\sqrt{2}\left[|M,P,0,0\rangle + \exp(i\phi)\,|M,0,0,P\rangle\right]$. Figure 2.3 shows the general picture of the system's behavior for this initial state, and compares the results obtained numerically with H with the ones obtained analytically, where we notice that they agree with each other (in principle, these results should agree for any initial state and set of parameters that satisfy the condition for resonance).

Together with the results from Eqs. 2.4.5 and 2.4.6, it is possible to notice, by analyzing Panels **(a)** and **(c)** from Fig. 2.3, that the phase ϕ of the initial state causes an oscillation on the population imbalance dynamics (at $t = \pi/(2\Omega) \equiv t_m \sim 6.15$ s) and fluctuations (at $t = t_m/2$ and $t = 3t_m/2$). In the next chapter, we will explore these features and demonstrate that they are the underlying mechanism that allows the integrable four-well system to function as both a Heisenberg-sensitive interferometer and a NOON state generator.

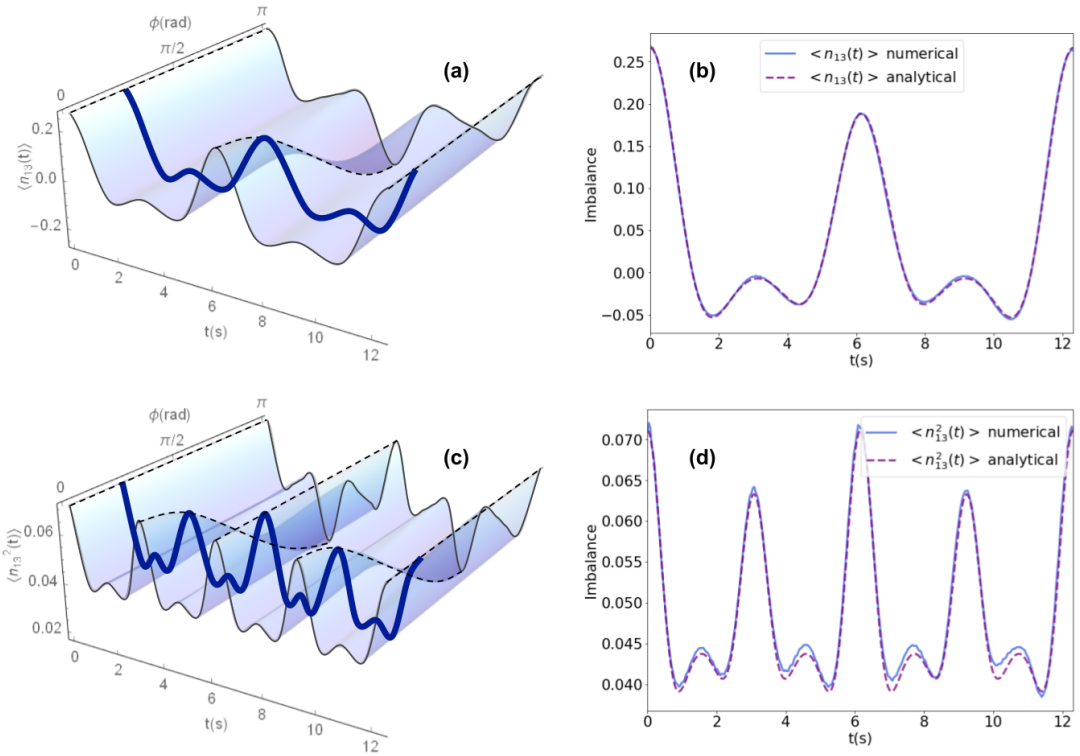

Figure 2.3: Quantum dynamics and fluctuations of the population imbalance. The calculations were made considering the hamiltonian parameters $U/\hbar = 100$ Hz, $J/\hbar = 70$ Hz and an initial state given by $|\Psi_0\rangle = 2^{-1/2}\left(|M,P,0,0\rangle + \exp(i\phi)\,|M,0,0,P\rangle\right)$, with $M = 4$ and $P = 11$. Panels **(a)** and **(c)** show, respectively, the behavior of $\langle n_{13}(t)\rangle$ and $\langle n_{13}^2(t)\rangle$ as function of t and ϕ, from the expressions of Equations 2.4.5 and 2.4.6. The solid lines depict the variation of $\langle n_{13}(t)\rangle$ and $\langle n_{13}^2(t)\rangle$ with respect to time, for a fixed ϕ, whereas the dashed lines show the behavior of $\langle n_{13}(t')\rangle$ and $\langle n_{13}^2(t')\rangle$ as a function of ϕ, for a fixed t'. Panels **(b)** and **(d)** depict the comparison between the analytically-predicted behavior of Equations 2.4.5 and 2.4.6 and the numerically-evaluated dynamics and fluctuations with the integrable hamiltonian H. These calculations were performed with $\phi = \pi/4$, and correspond to the blue (thick) curves of the figures depicted in panels **(a)** and **(c)**.

Chapter 3

Quantum device applications

In this Chapter, the applications of the four-well integrable model as quantum devices will be presented. While the first section is be devoted to interferometry (employing both classical and quantum states), Sections 3.2 and 3.3 are devoted, respectively, to the applications of the model as a quantum interferometer and a NOON state generator.

3.1 INTERFEROMETRY

Interferometry is a technique that consists on the verification of constructive and destructive interferences on a wave pattern that results from two contributions. Such an effect has several practical applications - amongst which path length measurements [58] and rotation sensing [59], and an improved version of the Michelson-type interferometer is currently being used by LIGO [60, 61] to measure gravitational waves.

According to [62, 63], a classical interferometer has a phase-sensitivity $\Delta\vartheta_{SN}$ that is limited by the "shot-noise". In order to provide a simple explanation for this, we will consider the interferometric setup depicted on Fig. 3.1. In the single-photon limit, the photon state after the beam-splitter (BS) can be written as:

$$|\gamma\rangle = \frac{1}{\sqrt{2}}\left[|\mathrm{L}\rangle + e^{i\vartheta}|\mathrm{R}\rangle\right], \tag{3.1.1}$$

where $|\mathrm{L}\rangle$ and $|\mathrm{R}\rangle$ are related, respectively, to the left and right paths, and $e^{i\vartheta}$ is the phase-difference acquired between the interferometer's arms. Then, the photon detector can be represented as [64] $\mathcal{D} = |\mathrm{L}\rangle\langle\mathrm{R}| + |\mathrm{R}\rangle\langle\mathrm{L}|$, which yields the "classical" interference pattern given by

$$\langle\gamma|\mathcal{D}|\gamma\rangle = \cos\vartheta. \tag{3.1.2}$$

Then, W repetitions of the same experiment, *with the same phase-difference between the arms*, leads to an interference pattern statistics given by:

$$\langle\gamma_W|\langle\gamma_{W-1}|\ldots\langle\gamma_1|\underbrace{\bigoplus_{i=1}^{W}\mathcal{D}_i}_{\equiv\mathcal{D}_W}|\gamma_1\rangle\ldots|\gamma_{W-1}\rangle|\gamma_W\rangle = W\cos\vartheta. \tag{3.1.3}$$

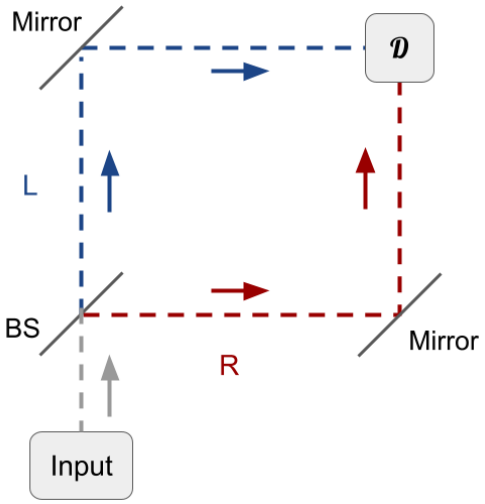

Figure 3.1: Interferometric scheme. The photons are sent from the input through the interferometric arms L and R. A 50/50 mirror works as a beam-splitter (BS), separating the photons between the two arms (with the same probability), which generates the state $|\gamma\rangle$ (see main text for more details). A phase-difference of $e^{i\vartheta}$ is acquired between the paths of the interferometer's arms (which can be caused by transmitting the light through a sample, a difference in length etc.), leading to an interference pattern in the detector $\mathcal{D}$, whose behavior differs for classical (Eq. 3.1.3) and quantum (Eq. 3.1.7) states of light.

We notice that $\mathcal{D}^2 = \mathbb{1}_2$, implying $\mathcal{D}_W^2 = \mathbb{1}_{2W}$, where $\mathbb{1}_j$ refers to the identity operator of dimension j. The variance of $\mathcal{D}_W$ can then be calculated as: $(\Delta\mathcal{D}_W)^2 = W\sin^2\vartheta$. Therefore, following the estimation theory [63], we evaluate the phase-sensitivity $\Delta\vartheta$ through:

$$\Delta\vartheta = \frac{\Delta\mathcal{D}_W}{\left|\frac{d\langle\mathcal{D}_W\rangle}{d\vartheta}\right|} = \frac{\sqrt{W}\sin\vartheta}{W\sin\vartheta} = \frac{1}{\sqrt{W}} \equiv \Delta\vartheta_{SN}. \tag{3.1.4}$$

The phase-sensitivity derived in Eq. 3.1.4 is the so-called "shot-noise limit". It immediately follows from its expression that, in order to make $\Delta\vartheta_{SN}$ twice as small, one should increase W by a factor of four. Later on, it was demonstrated that quantum mechanics could improve the sensitivity limit of an interferometer by employing a specific class of entangled states - called NOON states.

Being an "all-and-nothing" superposition, NOON states are a very special type of entangled states that take the form:

$$|NOON\rangle = \frac{1}{\sqrt{2}}\left[|W,0\rangle + |0,W\rangle\right], \tag{3.1.5}$$

where W is the number of photons/particles, which can be in one of two modes of a given system (usually a $^1/_2$-spin system, a two-level atomic system etc.). According to [65, 66], the employment of NOON states for interferometry leads to a new limit for phase-sensitivity (called "Heisenberg sensitivity"), which is governed by the quantum-mechanical uncertainty.

We will assume the same interferometric scheme of Fig. 3.1, with the difference that, now, the photons at the input are in a NOON state. Specifically in this case, we write the multi-photon quantum

state $|\gamma_W\rangle$ as:

$$|\gamma_W\rangle = \frac{1}{\sqrt{2}}\left[|W\rangle_R|0\rangle_L + e^{iW\vartheta}|0\rangle_R|W\rangle_L\right], \tag{3.1.6}$$

where the phase-argument was now multiplied by the total number of photons W (since each one of them must acquire a phase-difference). With the equivalence $|W\rangle \leftrightarrow |0\rangle_1|0\rangle_2...|0\rangle_W$ and $|\mathrm{L}\rangle \leftrightarrow |1\rangle_1|1\rangle_2...|1\rangle_W$, the detector can be expressed as $\mathcal{D} = |W\rangle\langle 0| + |0\rangle\langle W|$, and the interference pattern reads:

$$\langle\gamma_W|\mathcal{D}|\gamma_W\rangle = \cos W\vartheta. \tag{3.1.7}$$

Now, the variance will be given by $(\Delta\mathcal{D})^2 = \sin^2 W\vartheta$, and the phase-sensitivity can be calculated in a similar way to Eq. 3.1.4, which leads to:

$$\Delta\vartheta = \frac{\Delta\mathcal{D}}{|\frac{d\langle\mathcal{D}\rangle}{d\vartheta}|} = \frac{\sin W\vartheta}{W\sin W\vartheta} = \frac{1}{W} \equiv \Delta\vartheta_{HL}, \tag{3.1.8}$$

which corresponds to an improvement of the shot-noise limit by a factor of W. This tells us basically that, for making $\Delta\vartheta_{HL}$ twice as small, one should increase W by two (instead of four, as in the classical interferometer).

In the next two sections, we demonstrate two applications of the four-well integrable model that are related to the interferometry results demonstrated here.

3.2 Heisenberg-limited interferometer

The previously-demonstrated interferometric results take into account a photonic state. However, due to the wave-like behavior of matter, similar arguments can be employed to construct a matter-wave interferometer [67, 68, 69, 70] (also called atom-interferometer). Besides constituting (another) proof-of-principle of quantum-mechanical behavior, these systems can also be helpful for tests such as microgravity [71] and precision measurements [72].

In this section, we analyze the four-well integrable model in the context of Heisenberg-sensitive interferometry. As mentioned before, such sensitivity is usually achieved by considering a NOON-like state. Therefore, in our analysis, we will consider an initial state given by

$$|\Psi_0\rangle = \frac{1}{\sqrt{2}}\left[|M,P,0,0\rangle + \exp(iP\theta)|M,0,0,P\rangle\right], \tag{3.2.1}$$

Assuming that the four-well system works as a black-box interferometer, let us assign the function of "detector" (normalized with respect to the total number of particles) to the measurement operator $n_{13} = (N_1 - N_3)/N$. In the resonant regime, the expected value of this operator is given by the quantum dynamics of Eq. 2.4.5 with the identification $\phi \to P\theta$. To calculate the phase-sensitivity $\Delta\theta$, we need to first evaluate the variance $(\Delta n_{13}(t))^2 = \langle n_{13}^2\rangle - \langle n_{13}\rangle^2$. By setting $t = t_m$ on Eqs. 2.4.5 and 2.4.6, we arrive with:

$$\langle n_{13}(t_m)\rangle = \frac{M}{N}\cos(P\theta)(-1)^{(N+1)/2}, \qquad \langle n_{13}^2(t_m)\rangle = \frac{M^2}{N^2},$$

such that $(\Delta n_{13})^2$ can be evaluated, at $t = t_m$, as:

$$\Delta n_{13} = \sqrt{\langle n_{13}^2\rangle - \langle n_{13}\rangle^2} = \frac{M}{N}|\sin(P\theta)|. \tag{3.2.2}$$

Therefore, the phase-sensitivity $\Delta\theta$ can be calculated as:

$$\Delta\theta = \frac{\frac{M}{N}|\sin(P\theta)|}{|-\frac{M}{N}\,P\,P\sin(P\theta)|} = \frac{1}{P}\ , \tag{3.2.3}$$

indicating that, if the measurements of the interferometric results are done at $t = t_m$, the four-well integrable model works as a Heisenberg-sensitive interferometer [73], provided that the conditions that lead to Eq. 2.4.5 are satisfied (refer to Sec. 2.4).

3.2.1 Interferometric task

Here, we analyze how the system behaves on a simple interferometric task. Starting with an initial state given by $|\Psi_0\rangle = \frac{1}{\sqrt{2}}\left(|M,P,0,0\rangle + \exp(i\phi)\,|M,0,0,P\rangle\right)$, with $N \equiv M + P$ odd, it is possible to show that the state at time $t = t_m$, as predicted by the effective Hamiltonian, will be (see Appendix A.2 for more details):

$$\begin{aligned}|\Psi(t_m)\rangle &= e^{-\frac{iH_{eff}t_m}{\hbar}}|\Psi(0)\rangle \\ &= \frac{1+\beta e^{i\phi}}{2\sqrt{2}}\left[\beta\,|M,P,0,0\rangle + |M,0,0,P\rangle\right] + \frac{1-\beta e^{i\phi}}{2\sqrt{2}}\left[|0,P,M,0\rangle - \beta\,|0,0,M,P\rangle\right],\end{aligned} \tag{3.2.4}$$

where $\beta \equiv (-1)^{(N+1)/2}$. By analyzing Eq. 3.2.4, we conclude that an initial phase-difference converts into a population imbalance after $t = t_m$ (Fig. 3.2 illustrates the working device). In the limiting cases, no atom (M atoms) is (are) expected to be found on "site 3" if the phase-difference on the initial NOON state is $\phi = 0$ ($\phi = \pi$), for $\beta = 1$, and the oposite way around for $\beta = -1$. Such a result is also in agreement with Eq. 2.4.5. It is also worth noticing that, after the measurement procedure, the state will collapse again in a NOON state across "Sites 2 and 4", but without the phase-difference $e^{i\phi}$ factor. This allows us to probe the interferometric capabilities of the system in a very simple manner.

By employing the hamiltonian H, the state $|\Phi(t_m)\rangle$ is numerically calculated from the initial NOON state $|\Psi_0\rangle$ previously defined, with $U/\hbar = 100$ Hz, $J/\hbar = 70$ Hz, $M = 4$ and $P = 11$, for different values of $P\theta$. Then, at $t = t_m$, the probabilities of measuring different number of atoms at "Site 3" are evaluated. Differently than the ideal case, however, the probabilities of measuring $N_3 = r \neq 0, M$ will *not* be necessarily zero at $t = t_m$ - although they will be typically very small. Then, it is possible to take into account the possibility of generating NOON states for different atom numbers measured at "Site 3". The following states are now defined:

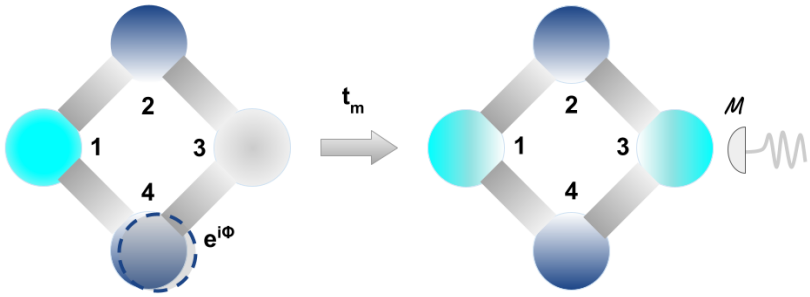

Figure 3.2: Interferometer. The spheres represent the wells and the thick lines depict the tunneling between them, and the dashed circle (displaced from the sphere center) represents a phase-difference on the respective site. The populations of $0, M$ and P atoms are illustrated, respectively, in white, cyan and blue. The initial state $|\Psi_0\rangle = \left(|M,P,0,0\rangle + e^{i\phi}|M,0,0,P\rangle\right)/\sqrt{2}$ (left) becomes the superposition of Eq. 3.2.4 after a time-evolution of t_m (right); then, a locally-projective measurement is performed in Site "3".

$$
\begin{aligned}
|\mathrm{NOON}_1^{(r)}\rangle &= |M-r,r\rangle_A \otimes \overbrace{\frac{1}{\sqrt{2}}\left(|P,0\rangle_B + \beta\,|0,P\rangle_B\right)}^{\text{NOON state definition}};\\
|\mathrm{NOON}_2^{(r)}\rangle &= |M-r,r\rangle_A \otimes \underbrace{\frac{1}{\sqrt{2}}\left(|P,0\rangle_B - \beta\,|0,P\rangle_B\right)}_{\text{NOON state definition}},
\end{aligned}
\tag{3.2.5}
$$

where $|a,b\rangle_X$ means that there are "a" atoms in site 1 and "b" atoms in site 3, if $X = A$ (i.e. class A), or "a" atoms in site 2 and "b" atoms in site 4, if $X = B$ (i.e. class B). Then, the fidelities between the resulting numerical states $|\Phi(t_m)_{N_3=r}\rangle$ after the collapse (after measuring $N_3 = r$) and both the predicted states of Eq. 3.2.5 are calculated, for $r = 0,1,...M$.

As can be seen in Fig. 3.3, a high fidelity $\mathcal{F}_{1(2)}(r) \equiv |\langle NOON_{1(2)}^{(r)}|\Phi(t_m)_{N_3=r}\rangle|$ is obtained for $r = 0, M$, even in the cases where the probability of measuring $r = 0, M$, for a given ϕ, is very low (but not theoretically zero). The reason behind this is the renormalization that occurs during the collapse of the system's state after a measurement procedure. By expanding the quantum state of Eq. 3.2.4 in the ket-state basis - with a constant total atom number - we get:

$$
|\Psi(t_m)\rangle = \sum_{i=0}^{N}\sum_{j=0}^{N-i}\sum_{k=0}^{N-i-j} c_{ijk}(t_m)\,|i,j,k,N-i-j-k\rangle\,,
\tag{3.2.6}
$$

where $\sum_{i=0}^{N}\sum_{j=0}^{N-i}\sum_{k=0}^{N-i-j}|c_{ijk}|^2 = 1$. Then, the probability of measuring $N_3 = r$ will be given by:

$$
\begin{aligned}
P(r) &= \sum_{i=0}^{N}\sum_{j=0}^{N-i}\sum_{k=0}^{N-i-j}|c_{ijk}(t_m)|^2\delta_{kr}\\
&= \sum_{i=0}^{N}\sum_{j=0}^{N-i}|c_{ijr}(t_m)|^2.
\end{aligned}
\tag{3.2.7}
$$

The resulting collapsed state after the measurement, $|\Psi(t_m)_{N_3=r}\rangle$, can be written as:

$$|\Psi(t_m)_{N_3=r}\rangle = \frac{1}{\sqrt{P(r)}} \sum_{i=0}^{N} \sum_{j=0}^{N-i} c_{ijr}(t_m) \, |i,j,r,N-i-j-r\rangle \,, \tag{3.2.8}$$

such that $\langle \Psi(t_m)_{N_3=r} | \Psi(t_m)_{N_3=r} \rangle = 1$. Here, one can also perform an identification between the states of Eqs. 3.2.5 and 3.2.8, yielding $|\Psi(t_m)_{N_3=0(M)}\rangle = |\mathrm{NOON}_{1(2)}^{(0(M))}\rangle$.

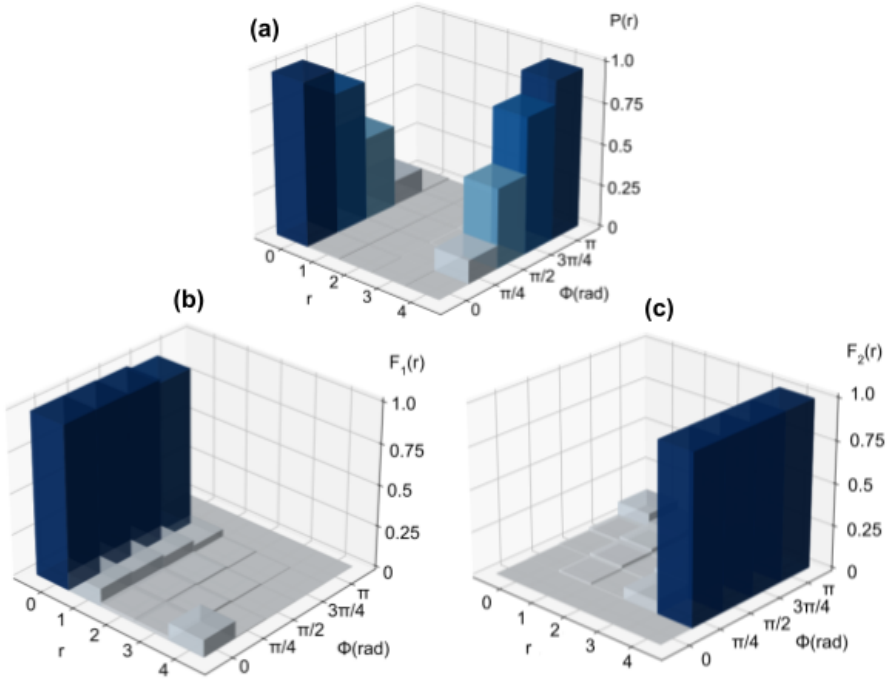

Figure 3.3: Probabilities and fidelities of the quantum interferometer. For the calculations, we consider $U/\hbar = 100$ Hz, $J/\hbar = 70$ Hz and $M, P = 4, 11$, with an initial state given by $|\Psi_0\rangle = 2^{-1/2}(|M,P,0,0\rangle + \exp(i\phi)\,|M,0,0,P\rangle)$. On the three panels, we vary r from 0 to M and ϕ from 0 to π. Panel **(a)** shows the probabilities of measuring $N_3 = r$ at $t = t_m$ for the different r and ϕ. Panels **(b)** and **(c)** depict, respectively, the fidelities $\mathcal{F}_1(r)$ and $\mathcal{F}_2(r)$ between the resulting collapsed state and $|\mathrm{NOON}_1^{(r)}\rangle$ and $|\mathrm{NOON}_2^{(r)}\rangle$, for different r and ϕ.

3.3 NOON STATE PROCESSOR

As shown in the previous section, the Four-well integrable model is able to function as a Heisenberg-sensitive interferometer, which requires the use of a special entangled state - called "NOON state". As seen before, a measurement procedure at $t = t_m$, for an initial NOON state, keeps the system in this configuration. It is still necessary, however, to be able to generate such state from an initial "Fock state" of the kind $|N_1, N_2, N_3, N_4\rangle$, which is, in principle, feasible with the current technology [74, 75]. Here, we disclose that this model also predicts the natural generation of the NOON states [76] throughout the system's quantum dynamics, provided that some conditions are taken into account when preparing the initial state.

In order to work as a NOON state generator, it is necessary for the system to be on the resonant regime and for the interaction between the charges Q_1, Q_2 in the effective hamiltonian of equation

2.3.1 to be nonzero, which translates into two conditions. The first one would be $\lambda_{12} \neq 0 \implies \Omega \neq 0$, which can be always achieved by choosing appropriate parameters while still on the resonant regime. The second one is $Q_1 Q_2 \neq 0$, such that neither Q_1 nor Q_2 can be zero. Since Q_1 (Q_2) algebraically depends on the number of particles in sites of class A (B) and the tunneling of particles between those sites, this implies that the initial state should contain bosons on at least one site of each class.

Considering an initial state given by $|\Psi_0\rangle = |M,P,0,0\rangle$, we evaluate its time-evolution $|\Psi(t)\rangle$ with the effective hamiltonian as $|\Psi(t)\rangle = e^{-iH_{eff}t}|\Psi_0\rangle$. By employing the eigenbasis of the conserved charges as defined in Equation 2.4.1 and supposing that the total number of particles $N = M + P$ is odd, we obtain, for the time t_m [73] (more details on Appendix A.2):

$$\begin{aligned} |\Psi(t_m)\rangle &= \frac{1}{2}\left[\beta|M,P,0,0\rangle + |M,0,0,P\rangle + |0,P,M,0\rangle - \beta|0,0,M,P\rangle\right] \\ &= \frac{1}{\sqrt{2}}\left(\beta|NOON_1^{(0)}\rangle + |NOON_2^{(M)}\rangle\right). \\ &\equiv |\text{uNOON}\rangle\,. \end{aligned} \tag{3.3.1}$$

From the quantum state of Equation 3.3.1, we propose that either $|NOON_1\rangle$ or $|NOON_2\rangle$ may be obtained by means of a measurement protocol, arbitrarily considering that the number of bosons in site 3 should be measured. Therefore, for each preparation of an initial state $|\Psi_0\rangle = |M,P,0,0\rangle$, both the probabilities of measuring $N_3 = 0$ and $N_3 = M$ (denoted $\mathcal{P}(0)$ and $\mathcal{P}(M)$, respectively) are equal to 0.5. However, since we are considering the analytical state of Equation 3.3.1, this result is only strictly valid for the effective Hamiltonian (Equation 2.3.1). Therefore, in order to evaluate that such NOON states could also be obtained from reasonable parameters $\{U,J\}$, we compare the NOON states obtained numerically with H with the ones of Eq. 3.3.1 (obtained with H_{eff}) in a similar way to what was done on previous section.

By considering $U/\hbar = 100$ Hz, $J/\hbar = 70$ Hz and $|\Psi_0\rangle = |M,P,0,0\rangle$, with $M = 4$, $P = 11$, and defining $|\Phi(t)\rangle = \exp(-iHt/\hbar)|\Psi_0\rangle$, we evaluate the probability $\mathcal{P}(r)$ of measuring $N_3 = r$, $r = 0,1...M$, from $|\Phi(t_m)\rangle$, and the fidelities $\mathcal{F}_{1(2)}(r)$ of the collapsed state with respect to $|NOON_1^{(r)}\rangle$ and $|NOON_2^{(r)}\rangle$. The results are shown in Table 3.1. In Figure 3.4, the contribution of every Fock-basis state is depicted, showing four clear peaks related to the the four states predicted in the superposition of Equation 3.3.1.

r	$\mathcal{P}(r)$	$\mathcal{F}_1(r)$	$\mathcal{F}_2(r)$
0	0.4978	0.9874	0.0099
1	0.0051	0.0883	0.0313
2	0.0028	0.0200	0.0158
3	0.0074	0.0105	0.1018
4	0.4799	0.0019	0.9961

Table 3.1: Probabilities of measuring $N_3 = r$ on $|\Phi(t_m)\rangle$ and fidelities of the collapsed state with respect to $|NOON_1^{(r)}\rangle$ and $|NOON_2^{(r)}\rangle$ ($\mathcal{F}_1(r)$ and $\mathcal{F}_2(r)$, respectively).

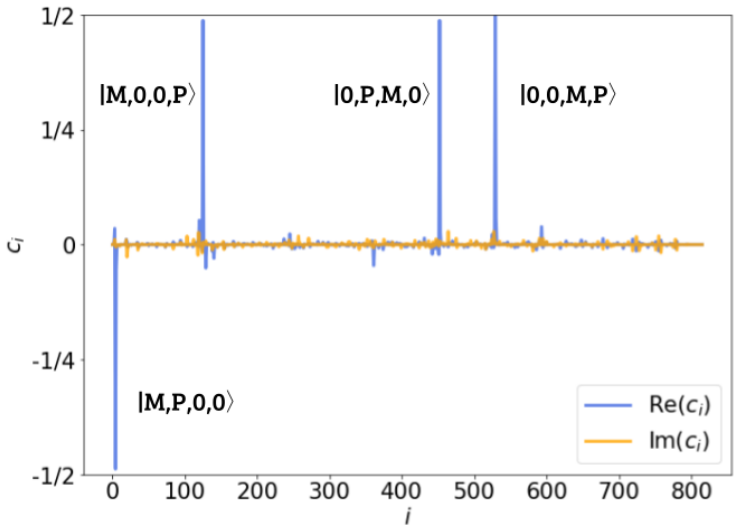

Figure 3.4: Fock-basis state coefficient distribution of $|\Phi(t_m)\rangle$, for $U/\hbar = 100$ Hz, $J/\hbar = 70$ Hz, $M = 4$ and $P = 11$. As expected from Eq. 3.3.1, there are four major contributions whose coefficient c_i are such that $c_i \in \mathbb{R}, |c_i| = 0.5$. In the employed matrix representation, the first coefficient refers to the state $|0,0,M,P\rangle$, whereas the other three are related to $|0,P,M,0\rangle$, $|M,0,0,P\rangle$ and $|M,P,0,0\rangle$, in order. The noisy background is due to the fact that the system is not perfectly resonant - so that states other than the four major contributions are also present in the superposition of $|\Phi(t_m)\rangle$.

Since $N = M + P = 15$ leads to $\beta = 1$, it is possible to relate the NOON states generated by this procedure with: $2^{-1/2}(|P,0\rangle + \exp(i\phi)|0,P\rangle)$, such that $\phi = 0$ for $N_3 = 0$ ($|NOON_1\rangle$) or $\phi = \pi$ for $N_3 = M$ ($|NOON_2\rangle$). Although limited in this sense, we emphasize here that the NOON states - or the superposition of both possibilities - are generated in a natural way, such that, for odd N, it is enough to just choose an appropriate set of parameters and let the system evolve up to the time $t = t_m$. Now, we ought to come up with a procedure for generating NOON states with arbitrary phase-encoding. As is shown in the next Subsection, this is done by simply considering small periods within the time evolution in which the system evolves with a controllable breaking of integrability.

3.3.1 Phase-encoding

As shown before, the integrable time-evolution of a system of described by H may result, on a time t_m, in the superposition of two NOON states, as described by Equation 3.3.1, where each of the NOON states is related to a phase-difference of either $\phi = 0$ or $\phi = \pi$. In order to extend this procedure such as to include arbitrary possibilities of phase-encoding, two protocols are proposed, taking breakings of integrability into account. Following [33], we choose the breaking of integrability that acts on two sites of the same class, causing the particles to stop (resonantly) tunneling between those sites. Such situation can be achieved through the introduction of the terms $\nu(N_1 - N_3)$ and $\mu(N_2 - N_4)$, which induce the breaking of integrability on classes A and B, respectively. The action of one of those terms in the state of Eq. 3.3.1 during a time $t_\mu(t_\nu)$ results in:

$$\begin{aligned}
&\exp\left(-\frac{i\nu t_\nu}{\hbar}(N_1-N_3)\right)|uNOON\rangle \\
&\qquad=\frac{1}{\sqrt{2}}\Big[\beta\,|M,P,0,0\rangle+|M,0,0,P\rangle+e^{iM\varphi}\,|0,P,M,0\rangle-\beta e^{iM\varphi}\,|0,0,M,P\rangle\Big]; \\
&\exp\left(-\frac{i\mu t_\mu}{\hbar}(N_2-N_4)\right)|uNOON\rangle \\
&\qquad=\frac{1}{\sqrt{2}}\Big[\beta\,|M,P,0,0\rangle+e^{iP\theta}\,|M,0,0,P\rangle+|0,P,M,0\rangle-\beta e^{iP\theta}\,|0,0,M,P\rangle\Big],
\end{aligned} \tag{3.3.2}$$

where $\theta = 2\mu t_\mu/\hbar$ and $\varphi = 2\nu t_\nu/\hbar$. However, it is strictly not possible to act only those terms on $|\Psi(t_m)\rangle$. Rather, one has to take the full hamiltonian into account, plus the breaking-of-integrability terms, for a physically meaningful phase-encoding protocol. We define a generalized time-evolution operator as

$$\mathcal{U}(t,\mu,\nu)=\exp\left[-\frac{it}{\hbar}\left(\mathcal{H}+\mu(N_2-N_4)+\nu(N_1-N_3)\right)\right], \tag{3.3.3}$$

which should replace the operators of Eq. 3.3.2 as $\mathcal{U}(t',0,\nu)$ and $\mathcal{U}(t',\mu,0)$. In the previous equation, $\mathcal{H}$ is the hamiltonian (which can be either H or H_{eff}). Now, since both the system's hamiltonian and the phase-encoding operators will take place simultaneously, one has to take some sort of "synchronization" into account, such that both the $|\text{uNOON}\rangle$ formation and the phase-enconding occur approximately at the same time. One may notice that, for $\mathcal{H}=H_{eff}$, $|\text{uNOON}\rangle=\mathcal{U}(t_m,0,0)\,|\Psi_0\rangle$, where $|\Psi_0\rangle = |M,P,0,0\rangle$. By considering a small displacement on $t_m \to t_m - \Delta t$, our total time-evolution operator for the case where $\mu\neq 0$, $\nu=0$ will be:

$$\begin{aligned}
\mathcal{U}(t_\mu,\mu,0)\mathcal{U}(t_m-\Delta t,0,0)&=\exp\left[-iH_{eff}\frac{t_\mu}{\hbar}-i\mu(N_2-N_4)\frac{t_\mu}{\hbar}\right]\exp\left[-iH_{eff}\frac{(t_m-\Delta t)}{\hbar}\right] \\
&=\exp\left[-i(H_{eff}+\mu(N_2-N_4))\frac{t_\mu}{\hbar}\right]\exp\left[-iH_{eff}\frac{(t_m-\Delta t)}{\hbar}\right] \\
&=\underbrace{\exp\left[-i(H_{eff}+\mu(N_2-N_4))\frac{t_\mu}{\hbar}\right]\exp\left[iH_{eff}\frac{\Delta t}{\hbar}\right]}_{\equiv Z}\exp\left[-iH_{eff}\frac{t_m}{\hbar}\right].
\end{aligned}$$

By employing the Baker–Campbell–Hausdorff's formula on the first two exponentials ($= Z$), we get, for small t_μ and Δt:

$$Z\approx\exp\left[-iH_{eff}\frac{(t_\mu-\Delta t)}{\hbar}-i\mu(N_2-N_4)\frac{t_\mu}{\hbar}\right].$$

Hence, we notice that, by choosing $\Delta t = t_\mu$, it is possible to obtain a final time-evolution operator which approximately decouples the integrable time-evolution and the breaking-of-integrability operator - i.e. decouples the formation of $|uNOON\rangle$ and its phase-encoding -, ending up with:

$$\mathcal{U}(t_\mu,\mu,0)\mathcal{U}(t_m-t_\mu,0,0)\approx\exp\left[-i\mu(N_2-N_4)\frac{t_\mu}{\hbar}\right]\exp\left[-iH_{eff}\frac{t_m}{\hbar}\right],\ \text{for } t_\mu\ll t_m. \tag{3.3.4}$$

Two things should be highlighted here. The first one is that the same analysis can be done for the case where $\mu=0$ and $\nu\neq 0$. And finally, t_μ should not be thought of as a fixed value. Rather, the purpose of this protocol is to allow the encoding of arbitrary phases on $|uNOON\rangle$ (and, by consequence, on $|NOON_1\rangle$ and $|NOON_2\rangle$) by varying either μ (ν) or t_μ. Once $|uNOON\rangle$ is generated and has a phase encoded, the same procedure described in Section 3.3 follows for obtaining either $|NOON_1\rangle$ or $|NOON_2\rangle$ with the desired phase encoded. Henceforward, it will be always considered a NOON state with phases of the kind $e^{iP\theta}$ encoded. The justification for this choice is simply the fact that, as the system may also work as a Heisenberg-sensitive interferometer (as shown in Section 3.2), it makes sense to encode phases which produce the most sensitive result for the phase-sensitivity (Eq. 3.2.3). As we will be considering $P=11$ and $M=4$ in every calculation, a phase-encoding that envolves $P\theta$ will be more sensitive than one using $M\varphi$.

3.3.1.1 Protocols

Now, two protocols are presented for the generation of NOON states with arbitrary phase encoding. The first one - Protocol I - relies on the same measurement procedure previously presented. Therefore, it can be divided in three steps. Using H_{eff} on the time-evolution operator:

(i) $|\Psi_1^I\rangle=\mathcal{U}(t_m-t_\mu,0,0)\,|\Psi_0\rangle$;

(ii) $|\Psi_2^I\rangle=\mathcal{U}(t_\mu,\mu,0)\,|\Psi_1^I\rangle$;

(iii) $|\Psi_3^I\rangle=\mathcal{M}\,|\Psi_2^I\rangle$.

In step (i), the integrable time-evolution approximately generates the uber-NOON state (exactly, if $t_\mu\to 0$), given by Eq. 3.3.1. The arbitrary phase-encoding occurs in step (ii), which results in the same state as the one obtained with the μ-breaking in Eq. 3.3.2. A measurement procedure of site 3 takes place in step 3. The outcomes of either 0 or M will result in a collapsed state $|\Psi_3^I\rangle$ given by either $|\mathrm{NOON}_1^{(0)}\rangle$ or $|\mathrm{NOON}_2^{(M)}\rangle$ of Eq. 3.2.5.

It is important to remember that these results are obtained by employing the effective hamiltonian (ensuring perfect resonant tunneling regime) and by considering $t_\mu\to 0$ (leading to a complete decoupling between the integrable time-evolution and the phase-encoding). We define $|\Phi_3^I\rangle$ as the state obtained numerically, by calculating all the steps with H. Therefore, in order to quantify how well the hamiltonian H is able to reproduce this protocol, we evaluate the fidelity $\mathcal{F}_I\equiv|\,\langle\Phi_3^I|\Psi_3^I\rangle\,|$, for t_μ varying between 0 and $\hbar\pi/(2P\mu)$ (hence varying $P\theta$ between 0 and π). These results are shown in Fig. 3.6 **(a)**, where we used $U/\hbar=100$ Hz, $J/\hbar=70$ Hz, $M=4$, $P=11$ and $\mu/\hbar=30$ Hz.

On the other hand, site-selective measurement, although already a reality in some experimental procedures [74, 75, 77], is somewhat still difficult to achieve, since it relies on a very precise Zeeman-splitting scheme, hence requiring the employment of extremely controllable and low-noise magnetic

field. Therefore, we also present another protocol for generating NOON states (with arbitrary phases) without the need of a measurement protocol. To achieve this, we propose that, in Protocol II, both breakings-of-integrability act on the system nonsimultaneously. Similarly to what was presented for Protocol I, here we split the procedure in five steps:

(i) $|\Psi_1^{II}\rangle = \mathcal{U}(t_m - t_\nu, 0, 0)\,|\Psi_0\rangle$;

(ii) $|\Psi_2^{II}\rangle = \mathcal{U}(t_\nu, 0, \nu)\,|\Psi_1^{II}\rangle$;

(iii) $|\Psi_3^{II}\rangle = \mathcal{U}(t_m - t_\mu, 0, 0)\,|\Psi_2^{II}\rangle$.

(iv) $|\Psi_4^{II}\rangle = \mathcal{U}(t_\mu, \mu, 0)\,|\Psi_3^{II}\rangle$.

In step (i), the integrable time-evolution approximately generates the uber-NOON state (exactly, if $t_\mu \to 0$), given by Eq. 3.3.1. In step (ii), the arbitrary phase-encoding occurs results in the same state as the one obtained with the ν-breaking in Eq. 3.3.2. Then, differently from the proposed scheme for Protocol I, we let the system once again time-evolve under the integrable hamiltonian for a time $t_m - t_\mu$, which results in:

$$|\Psi_3^{II}\rangle = \cos\left(\frac{M\varphi}{2}\right)|M,P,0,0\rangle - i\beta\sin\left(\frac{M\varphi}{2}\right)|M,0,0,P\rangle\,. \tag{3.3.5}$$

Although the state of Eq. 3.3.5 is not a NOON state, this can be easily achieved by "transforming" both the $\cos(...)$ and $\sin(...)$ into $1/\sqrt{2}$. Therefore, for any value of ν, we fix $t_\nu = \hbar\pi/(4M\nu)$, such that $\cos(M\varphi/2) = \sin(M\varphi/2) = 1/\sqrt{2}$. Then, the final phase-encoding is effectively achieved in step (iv), resulting in:

$$|\Psi_4^{II}\rangle = \frac{1}{\sqrt{2}}\left[|M,P,0,0\rangle + \beta e^{i(P\theta - \pi/2)}\,|M,0,0,P\rangle\right], \tag{3.3.6}$$

where the displacement $-\pi/2$ in the phase is due to the incorporation of i. We define $|\Phi_4^{II}\rangle$ the state obtained at step (iv) by performing all the steps numerically, with H. Then, similarly to the previous case, we evaluate the fidelities $\mathcal{F}_{II} \equiv |\,\langle\Phi_4^{II}|\Psi_4^{II}\rangle\,|$ for $P\theta$ varying between 0 and π (through the variation of t_μ). The results are depicted in Fig. 3.6 **(b)**, and an illustration of both protocols is presented in Fig. 3.5.

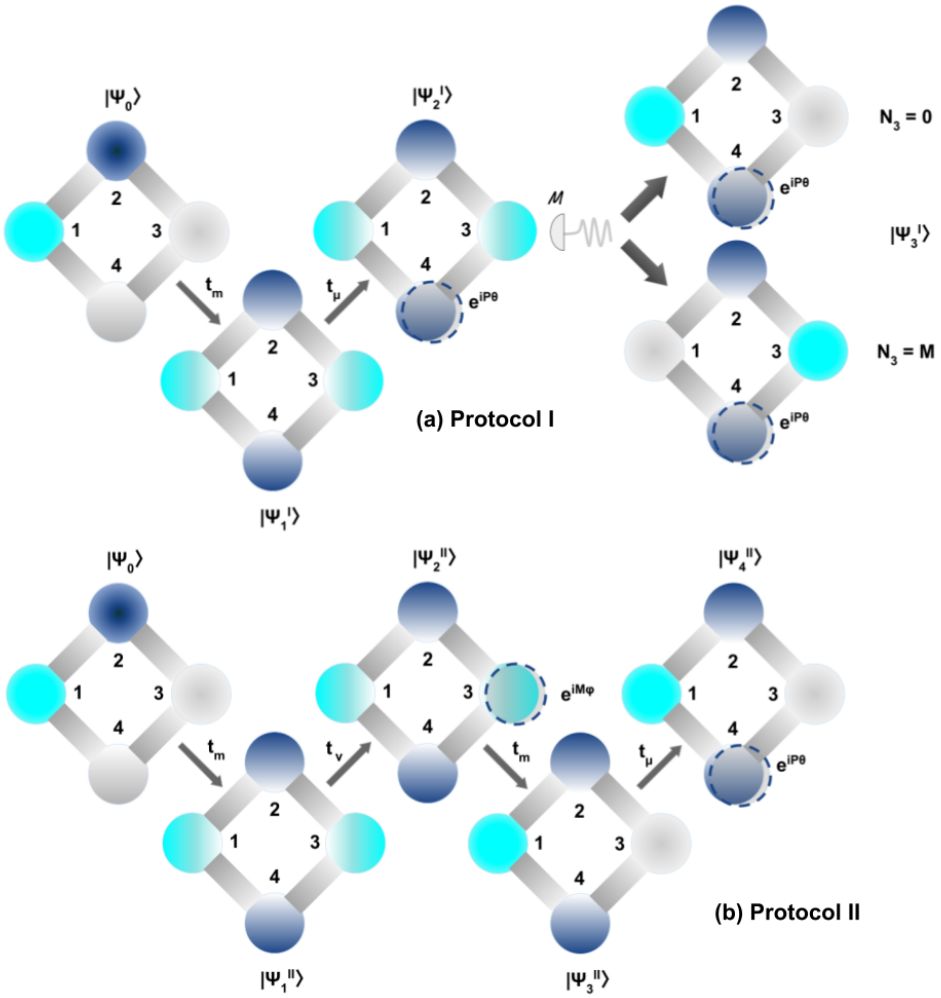

Figure 3.5: Protocols for NOON state generation. The spheres represent the wells and the thick lines depict the tunneling between them. The populations of $0, M$ and P atoms are illustrated, respectively, in white, cyan and blue, and the dashed circle (displaced from the sphere center) represents a phase-difference on the respective site. On Panel **(a)**, the Protocol I for NOON state generation is shown. Starting from a pure state $|\Psi_0\rangle = |M,P,0,0\rangle$, a time-evolution of $t = t_m$ yields the formation of the u-NOON state, followed by a phase-encoding through a breaking of integrability across sites "2-4" during t_μ. Afterwards, a local projective measurement $\mathcal{M}$ selects one of the two possible NOON states. With the same initial state, Protocol II (Panel **(b)**) does not depend on the measurement procedure. Instead, after the u-NOON formation, the breaking of integrability ν is turned-on during a time $t_\nu = \hbar\pi/(4M\nu)$, imprinting a phase-difference of $\pi/2$ between sites "1-3". Then, a NOON state across sites "2-4" is created after another time-evolution during t_m, with the final phase-encoding being done through a breaking of integrability across sites "2-4" during t_μ.

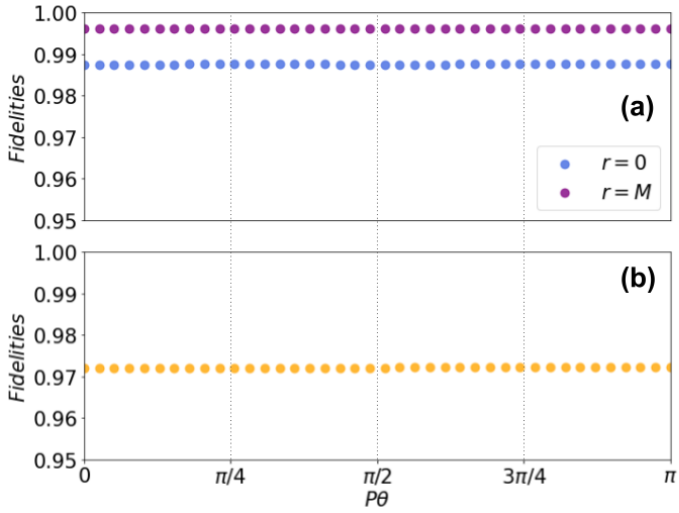

Figure 3.6: Fidelities of the generated NOON states through Protocols I **(a)** and II **(b)**, for different phases $P\theta$ encoded. The calculations were performed by considering an initial state $|\Psi_0\rangle = |M,P,0,0\rangle$, with $M = 4$ and $P = 11$, $U/\hbar = 100$ Hz, $J/\hbar = 70$ Hz and breaking-of-integrability parameters $\mu/\hbar = \nu/\hbar = 30$ Hz. By varying t_μ between 0 and $\hbar\pi/(2P\mu)(\sim 4.8$ ms$)$, we numerically generate the NOON states employing H on the time-evolution operator, with $P\theta$ ranging from 0 to π. In **(b)**, the time-interval t_ν was kept constant at $t_\nu = \hbar\pi/(4M\nu) \sim 6.5$ ms in order to generate a balanced superposition, which results in a NOON state (see text for more details).

Although we predicted the the model's ability to generate and encode phases on NOON states, its performance is directly related to the "level of resonance" in which the model is found (i.e. if the energies, for a given set of parameters and initial condition, are approximately equally spaced in one energy band of Fig. 2.2). Therefore, since both the band formation and the integrable time-evolution t_m depend on the parameters $\{U,J\}$, the existance of a trade-off between protocol time and fidelity becomes natural.

3.3.1.2 Fidelity vs protocol-time trade-off

In order to see how the fidelities $\mathcal{F}_I$ and $\mathcal{F}_{II}$ change with the protocol time, we vary $U/\hbar$ between 0 Hz and 140 Hz. Supposing an initial state $|\Psi_0\rangle = |M,P,0,0\rangle$, with $M = 4$, $P = 11$ and fixing $\mu/\hbar = \nu/\hbar = 30$ Hz and $J/\hbar = 70$ Hz, t_m becomes a parametrization of U, and varies accordingly between 0 s and 8.62 s. The results are shown in Figure 3.7.

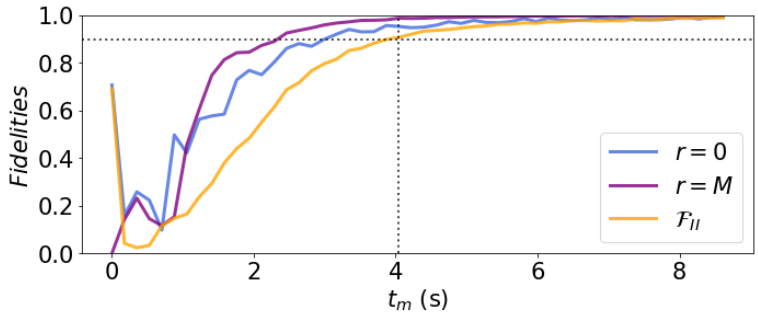

Figure 3.7: Fidelities of the NOON states obtained in Protocols I and II as a function of t_m. By employing the initial state $|\Psi_0\rangle = |M,P,0,0\rangle$, with $M = 4$ and $P = 11$, we evaluate the fidelities for $U/\hbar$ varying between 0 Hz and 140 Hz, while keeping $J/\hbar = 70$ Hz, $\mu/\hbar = \nu/\hbar = 30$ Hz, $t_\nu = \hbar\pi/(4M\nu) \sim 6.5$ ms and $t_\mu = \hbar\pi/(4P\mu) \sim 2.4$ ms ($P\theta = \pi/2$) fixed. The dotted lines highlight the lowest value of t_m for which the fidelities $\mathcal{F}_I(0(M))$ and $\mathcal{F}_{II}$ are all above 0.9 - approx. 4.044 s. Since the parametrization is done with a fixed J, this results in $U/\hbar \sim 65$ Hz as the lowest value for the interaction parameter that enables the system to produce NOON states with high fidelities.

By analyzing Fig. 3.7, it is noticeable that, for $t_m = 0$ ($U = 0$), $\mathcal{F}_I(0) = \mathcal{F}_{II} = 1/\sqrt{2}$. This is due to the fact that, when employing the protocols with $t_m = 0$, the system effectively barely performs a time-evolution, remaining at the initial state $|M,P,0,0\rangle$. Since this is one of the two states in the superpositions of $|\text{NOON}_1^{(0)}\rangle$ and $|\Psi_4^{II}\rangle$, the only nonzero component of the fidelity evaluation will be $1/\sqrt{2}$.

3.3.2 Phase read-out

One of the advantages of the proposed quantum device is the ability to check the reliability of the interferometer and the phase-encoding protocols on a self-consistent way, within the same system (in what we call "phase read-out"). This is done exactly by employing the interferometric capability of the four-well model at the end of Protocols I and II.

Protocol I ends with either $|\text{NOON}_1^{(0)}\rangle$ or $|\text{NOON}_2^{(M)}\rangle$ being generated (in case an outcome other than 0 or M is obtained at "step 3", this can just be discarded by post-selection). Then, in order to verify the phases encoded, we let the system evolve during another time-interval of $t = t_m$. This results (analytically) either in $|\Psi_{\text{RO}}^{I(0)}\rangle$ or $|\Psi_{\text{RO}}^{I(M)}\rangle$, which read:

$$\begin{aligned} |\Psi_{\text{RO}}^{\text{I},(0)}\rangle &= \frac{c(\theta)}{\sqrt{2}}(|M,P,0,0\rangle + \beta|M,0,0,P\rangle) + \frac{is(\theta)}{\sqrt{2}}(\beta|0,P,M,0\rangle - |0,0,M,P\rangle),\ r = 0, \\ |\Psi_{\text{RO}}^{\text{I},(M)}\rangle &= \frac{c(\theta)}{\sqrt{2}}(|M,P,0,0\rangle - \beta|M,0,0,P\rangle) - \frac{is(\theta)}{\sqrt{2}}(\beta|0,P,M,0\rangle - |0,0,M,P\rangle),\ r = M, \end{aligned} \tag{3.3.7}$$

where $c(\theta) \equiv \cos(P\theta/2)$ and $s(\theta) \equiv \sin(P\theta/2)$ and r stands for the measurement outcome at "step 3". Then, the complete set of measurements on Protocol I $\mathcal{P}_I(r,s)$ (state generation, readout) is expected to follow:

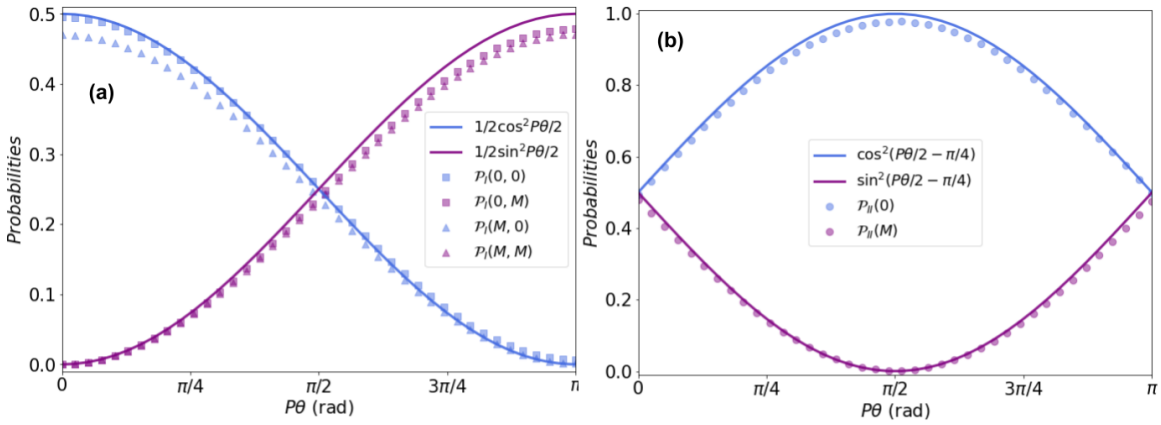

Figure 3.8: Readout procedure. Comparison between analytical expressions of Eqs. 3.3.8 and 3.3.10 and the respective numerically-obtained results with H. Panel **(a)** depicts the composed readout probabilities for Protocol I, and panel **(b)** shows the readout probabilities of Protocol II. The solid lines represent the analytical results on both cases. For the calculations, we considered the hamiltonian parameters $U/\hbar = 100$ Hz, $J/\hbar = 70$ Hz and $\mu/\hbar = \nu/\hbar = 30$ Hz, with an initial state given by $|M,P,0,0\rangle$, with $M = 4$ and $P = 11$.

$$\begin{aligned} \mathcal{P}_I(0,0) = \mathcal{P}_I(M,0) &= \frac{1}{2}\cos^2\left(\frac{P\theta}{2}\right); \\ \mathcal{P}_I(0,M) = \mathcal{P}_I(M,M) &= \frac{1}{2}\sin^2\left(\frac{P\theta}{2}\right). \end{aligned} \tag{3.3.8}$$

These results are shown alongside with the numerical ones on Panel **(a)** of Fig. 3.8. Protocol II, on the other hand, predicts the generation of only one possible NOON state. By letting $|\Psi_4^{II}\rangle$ also evolve during t_m, one obtains:

$$\begin{aligned} |\Psi_{\mathrm{RO}}^{II}\rangle = &\frac{1}{\sqrt{2}}c\left(\theta - \frac{\pi}{2P}\right)\left(|M,P,0,0\rangle + \beta\,|M,0,0,P\rangle\right) \\ &- \frac{i}{\sqrt{2}}s\left(\theta - \frac{\pi}{2P}\right)\left(\beta\,|0,P,M,0\rangle - |0,0,M,P\rangle\right), \end{aligned} \tag{3.3.9}$$

such that the two final possible outcomes - 0 and M - are expected with probabilities $\mathcal{P}_{II}$ given by:

$$\mathcal{P}_{II}(0) = \cos^2\left(\frac{P\theta}{2} - \frac{\pi}{4}\right), \qquad \mathcal{P}_{II}(M) = \sin^2\left(\frac{P\theta}{2} - \frac{\pi}{4}\right). \tag{3.3.10}$$

A comparison between these results and the numerical calculations with H are shown on Panel **(b)** of Fig. 3.8. By looking at the comparison for both Protocols I and II, it is clear that the predicted curves are usually slightly higher than the ones obtained numerically with H. This is, once again, an effect of the non-perfect resonant regime in which the system is with the employed hamiltonian parameters, such that contributions from other states are also present. As we will see on next Chapter, a similar feature occurs due to the same reason on the quantification of the system's entanglement.

Chapter 4

Entanglement

One of the most important features of the NOON state relies on the fact that it is an "all-or-nothing" superposition. Such characteristics enables it to be employed for interferometric purposes with a sensitivity limited by the Heisenberg Principle. An immediate consequence for this kind of superposition is that the state also presents a high level of entanglement. Although being in the core of the new developing quantum technologies, entanglement, only by itself, does not guarantee the usefulness of a given quantum state.

In this Chapter, we discuss the entanglement generated by the Four-well integrable system in the context of its two previously-addressed applications as a quantum device.

4.1 Von-Neumann entropy

Among several methods to quantify the "degree of entanglement" present on a given quantum system, one of the most employed ones is the so-called Von-Neumann entropy S. This method is based on the idea of diving the quantum system in two "partitions" - e.g. X and Y - and evaluating the entanglement between them.

If a given system is described by the density operator ρ, it is possible to obtain the operator ρ_X that describes its X partition by taking the partial trace of ρ over Y: $\rho_X = \mathrm{tr}_Y\, \rho$. Then, the entanglement between these partitions - $S(\rho_X) = S(\rho_Y)$ - is given by:

$$S(\rho_X) = -\mathrm{tr}\, \{\rho_X \log_2\, \rho_X\}. \tag{4.1.1}$$

The minimum value for $S(\rho_X) = S(\rho_Y)$ will is achieved when ρ_X (and, consequently, ρ_Y) is a pure state, such that it can be decomposed as $\rho_X = |\Psi_X\rangle \langle\Psi_X|$. In this case, ρ can be completely represented in the basis of $|\Psi_X\rangle$ as a 1x1 matrix, $\Gamma(\rho_X)$, and $S(\rho_X) = 0$. Its maximum value, on the other hand, occurs when ρ_X is a maximally-mixed state, reading $\rho_X = \frac{1}{d_X}\sum_i |\psi_i\rangle \langle\psi_i|$, d_X being the dimension of the X-partition Hilbert Space. This results in $S(\rho_X) = \log_2 d_X$. The next section contains an analysis of the Von-Neumann entropy for the four-well integrable model.

4.2 ENTANGLEMENT PRODUCTION OF THE SYSTEM

In this section, the production of entanglement by the four-well model is analyzed in the frame of the Von-Neumann entropy. Both the entanglement between classes A and B ("interclass entanglement") and the entanglement within one class ("intraclass entanglement") will be explored in the context of the NOON state generation and readout by the four-well system.

4.2.1 Entropy of interferometric states

As demonstrated in Sec. 3.2, when the initial state is given by a NOON state, the system works as a Heisenberg-sensitive interferometer, with the state obtained after a time-evolution up to $t = t_m$ given by Eq. 3.2.4 and a corresponding density operator $\rho(t_m) = |\Psi(t_m)\rangle \langle\Psi(t_m)|$. It is possible to show that the reduced operator $\rho_A(t_m)$ will be:

$$\begin{aligned}\rho_A(\phi) &= \mathrm{tr}_B\, \rho(\phi) = \mathrm{tr}_{24}\, \rho(\phi) \\ &= \sum_{u=0}^{N} \sum_{w=0}^{N-u} \langle u,w|\rho(\phi)|u,w\rangle_{2,4} \\ &= \frac{1+\beta cos\phi}{2} |M,0\rangle \langle M,0| + \frac{1-\beta\cos\phi}{2} |0,M\rangle \langle 0,M|\,,\end{aligned} \tag{4.2.1}$$

where $\langle x,y|A|x,y\rangle_{a,b}$ means that the state $|x,y\rangle$ is related to sites a and b. Since $\rho_A(\phi)$ is already decomposed in terms of an eigenbasis, the related Von-Neumann entropy $S(\rho_A(\phi))$ will be simply given by:

$$S(\rho_A(\phi)) = -\cos^2\frac{\phi}{2}\log_2\left(\cos^2\frac{\phi}{2}\right) - \sin^2\frac{\phi}{2}\log_2\left(\sin^2\frac{\phi}{2}\right). \tag{4.2.2}$$

By looking at the expression of Eq. 4.2.2, it is possible to see that $S(\rho_A(\phi))$ is π-periodic, being bounded between 0 and 1 for ϕ (accordingly) between 0 and $\pi/2$. This demonstrates that the entanglement production by the interferometric activity at $t = t_m$ (prior to measurement) depends on the phase ϕ initially encoded in the NOON state. This is as expected, since the working principle of the interferometer is the conversion ϕ from a phase-difference to a population-imbalance, which is directly related to different coefficients for the superposition of Eq. 4.2.2, yielding different values for $S(\rho_A(\phi))$.

After the measurement procedure is employed (as defined in Subsec. 3.2.1), the state will collapse to either of the two NOON states of Eq. 3.2.5, ideally with $r = 0$ or $r = M$. Taking $|NOON_1^{(0)}\rangle$ as an example, the equivalent density operator - $\rho^{(0)}$ - will read:

$$\rho^{(0)} = \frac{1}{2}|M,0\rangle \otimes \Big[|P,0\rangle \langle P,0| + |P,0\rangle \langle 0,P| + |0,P\rangle \langle P,0| + |0,P\rangle \langle 0,P|\Big] \otimes \langle M,0|\,. \tag{4.2.3}$$

Then, reduced density operator will be simply given by $\rho_A^{(0)} = |M,0\rangle \langle M,0|$. From this, we see

immediatly that the entanglement entropy between classes "A" and "B" is $S(\rho_A^{(0)}) = 0$, which means that there is no remaining on the entanglement between classes. However, such a result does not quantify the entanglement *within* a given class (i.e. the "intraclass" entanglement). To evaluate it for both classes "A" and "B", it is necessary to consider, respectively, the reduced matrices $\rho_1^{(0)} = \mathrm{tr}_3\, \rho_A^{(0)}$ and $\rho_2^{(0)} = \mathrm{tr}_4\, \rho_B^{(0)}$. Their calculation can be carried out in a similar that was done in Eq. 4.2.1 (with the necessary changes for $\rho_B(\phi)$), resulting in:

$$\begin{aligned} \rho_1^{(0)} &= |M\rangle\langle M|; \\ \rho_2^{(0)} &= \frac{1}{2}\left(|P\rangle\langle P| + |0\rangle\langle 0|\right). \end{aligned} \tag{4.2.4}$$

The evaluation of the Von-Neumann entropy for the previous density operators leads to $S(\rho_1^{(0)}) = 0$ and $S(\rho_2^{(0)}) = 1$. From these results, it is possible to conclude that, employed on Site "3", the measurement procedure on the state of Eq. 3.2.4 breaks both the entanglement between classes "A" and "B" and the entanglement *within* class "A", *leaving intact the entanglement within class "B"*. This agrees to the fact that the collapsed state after measuring $N_3 = r$ is also a NOON state across sites 2-4 (class "B").

A similar development could be done for the u-NOON state generated at $t = t_m$ with $|\Psi_0\rangle = |M,P,0,0\rangle$. This would result in an equivalent representation of $\rho_A(t_m)$ as the one of Eq. 4.2.1 with $\phi = \pi/2$, resulting in a Von-Neumann Entropy for the u-NOON of $S(\rho_A(t_m)) = 1$. The supression of such development was done to avoid repeatedness.

4.2.2 Entanglement dynamics: analytical results

For $|\Psi_0\rangle = 2^{-1/2}(|M,P,0,0\rangle + \exp(i\phi)\,|M,0,0,P\rangle)$, it is possible to write $|\Psi(t)\rangle$ in terms of the basis $|M,P,q_1,q_2\}$ defined in Eq. 2.4.1, resulting in:

$$\begin{aligned} |\Psi(t)\rangle &= e^{-iH_{eff}t}\,|\Psi_0\rangle \\ &= \frac{1}{\sqrt{2}}\sum_{q_1=0}^{M}\sum_{q_2=0}^{P} e^{-it\epsilon_{q_1,q_2}}|M,P,q_1,q_2\}\sqrt{\frac{C_{q_1}^M C_{q_2}^P}{2^N}}(1+(-1)^{q_2}e^{i\phi}), \end{aligned} \tag{4.2.5}$$

where $C_n^m = \frac{m!}{n!(m-n)!}$, if $n \in \{0,...m\}$, and $C_n^m = 0$ otherwise. Here, we will consider $\hbar = 1$ for simplicity. Then, the reduced density operator $\rho_A(t)$ will be given by (see Appendix A.3 for more details):

$$\begin{aligned}\rho_A(t) &= \mathrm{tr}_B\ |\Psi(t)\rangle\langle\Psi(t)| \\ &= \sum_{m,n=0}^{N} \langle m,n|\Psi(t)\rangle\langle\Psi(t)|m,n\rangle \\ &= \frac{1}{2^{N+1}} \sum_{q_1,p_1=0}^{M} e^{2it\Omega[N]_+(p_1-q_1)} \sqrt{C_{q_1}^M C_{p_1}^M} \left[1+e^{-2it\Omega(p_1-q_1)}\right]^P |\chi(q_1)\rangle\langle\chi(p_1)|, \\ &+ \frac{\cos\phi}{2^{N+1}} \sum_{q_1,p_1=0}^{M} e^{2it\Omega[N]_+(p_1-q_1)} \sqrt{C_{q_1}^M C_{p_1}^M} \left[1-e^{-2it\Omega(p_1-q_1)}\right]^P |\chi(q_1)\rangle\langle\chi(p_1)|\end{aligned} \tag{4.2.6}$$

with the definition $|\chi(q)\rangle = \frac{1}{\sqrt{(M-q)!q!}} \left(\frac{a_1^\dagger + a_3^\dagger}{2}\right)^{M-q} \left(\frac{a_1^\dagger - a_3^\dagger}{\sqrt{2}}\right)^q |0\rangle_A$. Finally, for $t = t_m = \pi/(2\Omega)$, the reduced density operator reads:

$$\rho_A(t_m) = \frac{1+\cos\phi}{2} |\Psi_+\rangle\langle\Psi_+| + \frac{1-\cos\phi}{2} |\Psi_-\rangle\langle\Psi_-|, \tag{4.2.7}$$

where $|\Psi_\pm\rangle = 2^{-M/2} \sum_{q=0}^{M} e^{\mp iq\pi[N]_\pm} \sqrt{C_q^M}\, |\chi(q)\rangle$, with $[N]_\pm \equiv (N \pm 1)/2$. These states are orthonormalized, since:

$$\begin{aligned}\text{(i)}\ \langle\Psi_\pm|\Psi_\pm\rangle &= \frac{1}{2^M} \sum_{p,q=0}^{M} e^{-iq\pi[N]_\pm} e^{ip\pi[N]_\pm} \sqrt{C_q^M C_p^M} \underbrace{\langle\chi(p)|\chi(q)\rangle}_{\delta_{p,q}} \\ &= \frac{1}{2^M} \sum_{q=0}^{M} C_q^M = 1; \\ \text{(ii)}\ \langle\Psi_+|\Psi_-\rangle &= \frac{1}{2^M} \sum_{p,q=0}^{M} e^{-iq\pi[N]_+} e^{ip\pi[N]_-} \sqrt{C_q^M C_p^M} \underbrace{\langle\chi(p)|\chi(q)\rangle}_{\delta_{p,q}} \\ &= \frac{1}{2^M} \sum_{q=0}^{M} C_q^M (-1)^q = 0,\end{aligned}$$

and hence may constitute a basis on Eq. 4.2.7. With this, it is possible to represent $\rho_A(t_m)$ of Eq. 4.2.7 as $\frac{1}{2}\mathbb{1}_2$, where $\mathbb{1}_2$ is the identity matrix o dimension 2. Then, the Von-Neumann entropy in this case will be simply given by $S(\rho_A(t_m)) = -\cos^2\phi \log_2 \cos^2\phi - \sin^2\phi \log_2 \sin^2\phi$. Through a similar development, it can be demonstrated that the same expression of Eq. 4.2.7 results for $\rho_B(t_m)$, with the exchange $M \to P$ on $|\Psi_\pm\rangle$ expressions, which is in agreement with the bipartite-system equivalency $S(\rho_A) = S(\rho_B)$.

The results above are independent from the total number of particles, and just require the system to be in the band-formation regime (resonant regime), with an initial state with atoms on both classes A and B. This is quite surprising when one takes into account the results of the previous Subsection regarding the Von-Neumann entropy for the (u)NOON states. As shown on Sec. 3.2, the prediction of (u)NOON state formation is directly linked to the total number of atoms N in the system, being generated only if N is odd. The results shown previously seem to contradict it, as the prediction of $S(\rho_A(t_m))$

occurs with the same value for both N odd and even. What it suggests, however, is that the generation of entanglement *per se* is not at all necessarily useful, and one should investigate beyond such quantification in order to prepare quantum states that are interesting for a desired application (as noted in [78]).

To quantify the entanglement between one site - for example, "3" - and the other three, it is necessary to first evaluate the reduced operator ρ_3. Such an operator has a simplified expression given by:

$$\rho_3(t_m) = \sum_{j=0}^{N} \mathcal{P}_3(j) \left|j\right\rangle \left\langle j\right|, \tag{4.2.8}$$

where $\mathcal{P}_3(l)$ is the probability of measuring l particles at site "3", at $t = t_m$. The generalized expression for the $\mathcal{P}_3(l)$ can be obtained by calculating $\mathcal{P}_3(l) = \langle M-l,l|\rho_3(t_m)|M-l,l\rangle$. The previous expression can be decomposed into two inner products, whose development can be found in Appendix A.3, leading to:

$$\mathcal{P}_3(l) = \frac{1}{2} b_{M,l}(\sin^2(\pi[N]_+/2)) + \frac{1}{2} b_{M,l}(\sin^2(\pi[N]_-/2)). \tag{4.2.9}$$

with $b_{W,r}$ being the Bernstein polynomials, given by $b_{W,r}(x) = C_r^W x^r (1-x)^{W-r}$. Contrary to the numerical values for $S(\rho_A(t_m))$ (and $S(\rho_B(t_m))$), the measurement probabilities are not the same for N odd and even, leading to:

$$\begin{aligned} \mathcal{P}_3(l) &= \frac{1}{2}\delta_{0,l} + \frac{1}{2}\delta_{M,l}, && \text{for } N \text{ odd}, \\ \mathcal{P}_3(l) &= \frac{C_l^M}{2^M}, && \text{for } N \text{ even}. \end{aligned} \tag{4.2.10}$$

The probability distribution for N odd implies on probabilities of $1/2$ both for measuring $N_3 = 0$ and $N_3 = M$. This is in accordance with the u-NOON formation at $t = t_m$ (Eq. 3.3.1). The different behavior in the case of N even is due to the fact that a u-NOON state is not generated at $t = t_m$, leading to a different distribution of measurement probabilities with more than two possible outcomes after measuring N_3.

4.2.3 Entanglement dynamics: numerical evaluation

At a time t, the system's density operator can be written as:

$$\begin{aligned} \rho(t) &= \left|\Phi(t)\right\rangle \left\langle\Phi(t)\right| \\ &= \sum_{i_1,i_2} \sum_{j_1,j_2} \sum_{k_1,k_2} c_{i_1,j_1,k_1}(t)(c_{i_2,j_2,k_2}(t))^* \left|i_1,j_1,k_1,N-i_1-j_1-k_1\right\rangle \left\langle i_2,j_2,k_2,N-i_2-j_2-k_2\right|, \end{aligned} \tag{4.2.11}$$

where the following definitions were made:

- $\sum_{i_1,i_2} \equiv \sum_{i_1=0}^{N} \sum_{i_2=0}^{N}$;
- $\sum_{j_1,j_2} \equiv \sum_{j_1=0}^{N-i_1} \sum_{j_2=0}^{N-i_2}$;

- $\sum_{k_1,k_2} \equiv \sum_{k_1=0}^{N-i_1-j_1} \sum_{k_2=0}^{N-i_2-j_2}$.

Then, the calculation of $\rho_B(t') = \mathrm{tr}_A\, \rho(t')$ reads:

$$\begin{aligned}\rho_B(t) &= \sum_{s=0}^{N} \sum_{p=0}^{N-s} \langle s,p|\rho(t)|s,p\rangle \\ &= \sum_{s=0}^{N} \sum_{p=0}^{N-s} \sum_{j_1,j_2=0}^{N-s-p} c_{s,j_1,p}(t)(c_{s,j_2,p}(t))^* \left|j_1, N-s-j_1-p\right\rangle \left\langle j_2, N-s-j_2-p\right|\end{aligned} \tag{4.2.12}$$

Now, by rearranging the summations $\sum_{s=0}^{N}\sum_{p=0}^{N-s} \to \sum_{p=0}^{N}\sum_{s=0}^{p}$, we can rewrite Eq. 4.2.12 as:

$$\begin{aligned}\rho_B(t) &= \sum_{p=0}^{N} \sum_{j_1,j_2=0}^{N-p} \sum_{s=0}^{p} c_{j_1,s,N-p-j_1}(c_{j_2,s,N-p-j_2})^* \left|j_1, N-j_1-p\right\rangle \left\langle j_2, N-j_2-p\right| \\ &= \sum_{p=0}^{N} \rho_{B,p}\end{aligned} \tag{4.2.13}$$

with $\rho_{B,p} \equiv \sum_{j_1,j_2=0}^{N-p} \sum_{s=0}^{p} c_{j_1,s,N-p-j_1}(c_{j_2,s,N-p-j_2})^* \left|j_1, N-j_1-p\right\rangle \left\langle j_2, N-j_2-p\right|$ being a square matrix with dimensions $(N-p)$. A representation $\Gamma(\rho_B(t))$ can be written in terms of the direct sum of the representations of $\rho_{B,p}$,

$$\Gamma(\rho_B(t)) = \bigoplus_{p=0}^{N} \Gamma(\rho_{B,p}(t)), \tag{4.2.14}$$

from which it is easy to see that $S(\rho_B(t)) = -\sum_{p=0}^{N} \mathrm{tr}\left\{\rho_{B,p}(t)\log_2 \rho_{B,p}(t)\right\}$. Figure 4.1 depicts the numerically-evaluated Von-Neumann entropies $S(\rho_B(t_m))$ for both H and H_{eff} in comparison with analytical results, for N even ($M=3$, $P=11$) and odd ($M=4$, $P=11$).

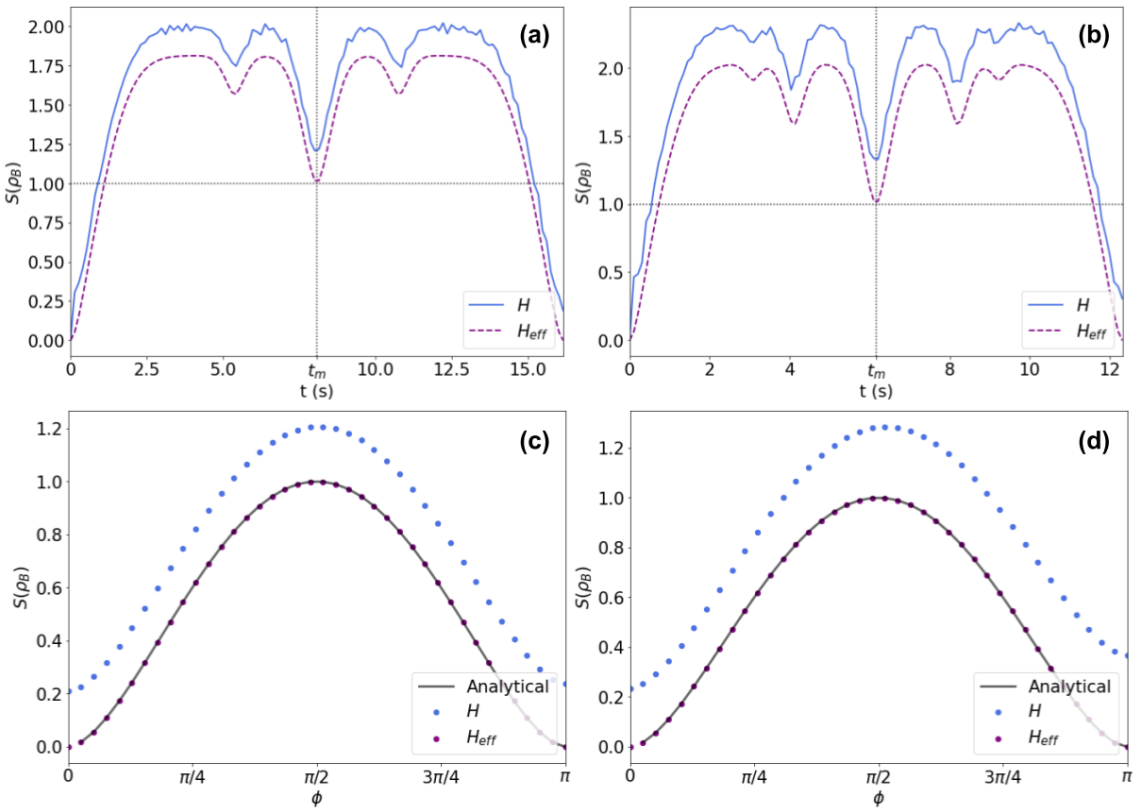

Figure 4.1: Von-Neumann entropy. The panels on the left (**(a)**, **(c)**) and right (**(b)**, **(d)**) correspond, respectively, to the atom-number distributions $\{M = 3,\ P = 11\}$ (N even) and $\{M = 4,\ P = 11\}$ (N odd). On top panels (**(a)**, **(b)**), we present the results $(\rho_B(t))$ for an initial state given by $|\Psi_0\rangle = |M,P,0,0\rangle$, while on the bottom panels (**(c)**, **(d)**) we consider $|\Psi_0\rangle = 2^{-1/2}\left(|M,P,0,0\rangle + \exp(i\phi)\,|M,0,0,P\rangle\right)$, and $S(\rho_B(t_m))$ is depicted for ϕ ranging between $[0,\pi]$. The data in purple (blue) was evaluated with the Hamiltonian H_{eff} (H). On panels **(c)-(d)**, the black, solid line illustrates the analytical results of Eq. 4.2.2.

Chapter 5

Extended Bose-Hubbard model

In this chapter, we begin by discussing the fact that the traditional Bose-Hubbard hamiltonian does not allow for a particular integrable set of couplings. Then, we show that this is possible by employing an extension of this model - called Extended Bose-Hubbard (EBH) hamiltonian -, which results in a specific integrability condition that must be fulfilled. We also develop expressions for the tunneling and interaction parameters for an (almost) arbitrary trapping potential.

5.1 Derivation and considerations

The Bose-Hubbard model describes the physics of ultracold bosonic atoms trapped in different sites or wells. It was demonstrated to be naturally integrable in the limits of two-sites and inifinite-sites systems, but not for an arbitrary number of wells different that those two. Its hamiltonian is generally given by

$$H = \frac{U_0}{2}\sum_i N_i(N_i-1) - j_t \sum_{\langle i,j\rangle} a_i^\dagger a_j - \mu \sum_i N_i,$$

where U_0 is the contact interaction between atoms at the same site, j_t represents the hopping amplitude between different nearest-neighbors sites - as stated by the $\langle i,j\rangle$ notation - and μ stands for the chemical potential. Also, N_i is the number operator, $a_i^\dagger$ is the creation operator for site i and a_j is the annihilation operator for site j. In the case of a fixed total number of particles, the last term becomes a global constant and can therefore be ignored for quantum dynamics.

The Hamiltonian above does not present long-range interactions and, therefore, it is not possible to connect it with the integrable four-well model. Hence, we must consider the system as made up with atoms that present the kind of interactions necessary to achieve an integrable point. By supposing that the system is composed of dipolar bosonic atoms in an ultracold regime, the Gross-Pitaevskii Energy Functional may be employed as a starting point for the model hamiltonian deduction. The functional is given by:

$$E[\Phi(\mathbf{r})] = \int d\mathbf{r}\, \Phi^*(\mathbf{r}) \left[-\frac{\hbar^2}{2m}\nabla^2 + V_{trap}(\mathbf{r}) + \frac{1}{2}\int d\mathbf{r'}\, \Phi^*(\mathbf{r'}) V(\mathbf{r}-\mathbf{r'}) \Phi(\mathbf{r'}) \right] \Phi(\mathbf{r}), \tag{5.1.1}$$

where we have already considered a fixed total number of particles N. There, $\Phi(\mathbf{r})$ is the collective wavefunction of the atoms, m is the atom's mass, $V_{trap}(\mathbf{r})$ is the potential generated by the trapping apparatus and depends on its physical realization, and $V(\mathbf{r}-\mathbf{r'}) = V_{sr}(\mathbf{r}-\mathbf{r'}) + V_{dd}(\mathbf{r}-\mathbf{r'})$ is the interaction potential between the atoms, such that $V_{sr}(\mathbf{r}-\mathbf{r'})$ and $V_{dd}(\mathbf{r}-\mathbf{r'})$ stand, respectively, for the short-range contact interaction and the dipole-dipole interaction (D.D.I). To discretize the system in different sites, we perform a second-quantization procedure:

$$\begin{aligned} \Phi(\mathbf{r}) &\to \Psi(\mathbf{r}), \\ \Phi^*(\mathbf{r}) &\to \Psi^\dagger(\mathbf{r}), \end{aligned} \tag{5.1.2}$$

where $\Psi(\mathbf{r})$ and $\Psi^\dagger(\mathbf{r})$ are, respectively, the bosonic annihilation and creation field operators. By considering localized wavefunctions for the atoms, we perform the four-site expansion $\Psi(\mathbf{r}) = \sum_{i=1}^{4} \phi_i(\mathbf{r}) a_i$, where $\phi_i(\mathbf{r})$ is the wavefunction of a single boson in site i, defined as the ground-state of $V_{trap}(\mathbf{r})$ in harmonic approximation. Hence, $\phi_i(\mathbf{r})$ must be a gaussian function, which means $\phi_i(\mathbf{r}) = \phi_i^*(\mathbf{r})$. This approximation is already driven by the assumption that the trapping potential for the atoms presents minima on four different spatial region - the corresponding potential for the experimental scheme proposed in the Dissertation will behave accordingly, as demonstrated in the next Chapter (see Eq. 6.3.1). By inserting it into Eq. 5.1.1, we obtain:

$$H = -\sum_{ij} J_{ij} a_i^\dagger a_j + \sum_{ij} \frac{U_{ijkl}}{2} a_i^\dagger a_j^\dagger a_k a_l, \tag{5.1.3}$$

with J_{ij} and U_{ijkl} being, respectively, the hopping and interaction couplings between atoms of different sites, whose expressions are given by:

$$\begin{aligned} J_{ij} &= \int d\mathbf{r}\, \phi_i(\mathbf{r}) \left[\frac{\hbar^2 \nabla^2}{2m} - V_{trap}(\mathbf{r}) \right] \phi_j(\mathbf{r}); \\ U_{ijkl} &= \int d\mathbf{r} \int d\mathbf{r'}\, \phi_i(\mathbf{r'}) \phi_j(\mathbf{r})\; V(\mathbf{r}-\mathbf{r'})\; \phi_k(\mathbf{r}) \phi_l(\mathbf{r'}). \end{aligned} \tag{5.1.4}$$

The expression for J_{ij} can be expanded as $J_{ij} + \epsilon_i$, where J_{ij} now implicitly means $i \neq j$ and is related to the particle hopping between sites, while $\epsilon_i \equiv J_{ii}$ represents a difference in the trapping energy in each site. If every site experiences the same trapping potential, then $\epsilon_i = \epsilon_j \; \forall \; i \neq j$, which means $\sum_i \epsilon_i a_i^\dagger a_i = \sum_i \epsilon_i N_i \propto N$ is a global constant, an can be ignored on the Hamiltonian. As will be shown later, such symmetry is not conserved anymore when one introduces a breaking of integrability in the system.

The interaction potential $V(\mathbf{r}-\mathbf{r'})$ is given by:

$$V(\mathbf{r}-\mathbf{r'}) = \underbrace{g\delta(\mathbf{r}-\mathbf{r'})}_{V_{SR}} + \underbrace{\frac{C_{dd}}{4\pi} \frac{1-3\cos^2\theta_P}{|\mathbf{r}-\mathbf{r'}|^3}}_{V_{DD}}.$$

In the contact interaction (V_{SR}), $g = \frac{4\pi\hbar^2 a}{m}$, where a is the s-wave scattering length, which can be positive or negative - yielding, respectively, a repulsive and attractive contact interaction -, and whose

values can be tuned through a magnetic field via a process called "Feshbach Resonance" [79]. In the DDI (V_{DD}), $C_{dd} = \mu_0 \mu^2$, where $\mu_0 = 4\pi \times 10^{-7} N/A^2$ is the vacuum magnetic permeability, μ is the atom's magnetic dipole moment and θ_P is the angle between the dipole orientation and the direction of $\mathbf{r} - \mathbf{r'}$. Now, we simplify the expressions for J_{ij} and U_{ijkl} through a few assumptions. First, let us suppose that the atoms are well confined, such that:

$$\int d\mathbf{r}\, \phi_i(\mathbf{r})\phi_j(\mathbf{r}) \text{ is nonzero only for } i = j \text{ and } i,j \text{ first-neighbors;}$$
$$\int d\mathbf{r}\, \phi_i(\mathbf{r})\phi_j(\mathbf{r})\phi_k(\mathbf{r})\phi_l(\mathbf{r}) \text{ is nonzero only for } i = j = k = l;$$
$$\int d\mathbf{r} \int d\mathbf{r'} \phi_i(\mathbf{r'})\phi_j(\mathbf{r})\phi_k(\mathbf{r})\phi_l(\mathbf{r'})|\mathbf{r} - \mathbf{r'}|^{-3} \text{ is nonzero only for } i = l \text{ and } j = k.$$

Also, Considering that the distance between each nearest-neighbor site is the same, we immediately obtain $J_{ij} = J_{ji}$. Hence, we rewrite the interaction term as $U_{ijkl} = U_{sr}\delta_{ij} + U_{ij}\delta_{il}\delta_{jk}$, where:

$$\begin{aligned} U_{sr} &= g \int d\mathbf{r}\, \phi^4(\mathbf{r}); \\ U_{ij} &= \frac{C_{dd}}{4\pi} \int d\mathbf{r} \int d\mathbf{r'} \phi_i^2(\mathbf{r})\phi_j^2(\mathbf{r'}) \frac{1 - 3\cos^2\theta_P}{|\mathbf{r} - \mathbf{r'}|^3}., \end{aligned} \tag{5.1.5}$$

and the hamiltonian of Equation 5.1.3 becomes

$$H = \frac{U_0}{2} \sum_i N_i(N_i - 1) + \sum_{i \neq j} \frac{U_{ij}}{2} N_i N_j - \sum_{\langle i,j \rangle} J_{ij} a_i^\dagger a_j, \tag{5.1.6}$$

which is the EBH hamiltonian [80] for the case where $[H, N] = \sum_i [H, N_i] = 0$. The parameter U_{ij} on Equation 5.1.6 stands for the D.D.I between bosons at different sites, while U_0 comprehends both the contact interaction and the D.D.I between bosons at the same site. Here, we highlight that, in the case of DDI$\to 0$, the hamiltonian of Eq. 5.1.6 becomes the Bose-Hubbard hamiltonian.

5.2 (Semi-)Analytical expressions

In harmonic approximation, the trapping potential around a minimum can be written as:

$$V_{trap}^{(h)}(\mathbf{r}) = \frac{1}{2} m(\omega_x^2 x^2 + \omega_y^2 y^2 + \omega_z^2 z^2).$$

For the reasons that will become clearer in the next Chapter, we will consider that trapping potential is symmetric on $x - y$, such that $\omega_x = \omega_y \equiv \omega_r$, where ω_r is called the "radial trapping frequency". Then, we can rewrite the above expression as:

$$V_{trap}^{(h)}(\mathbf{r}) = \frac{1}{2} m\omega_r^2 (x^2 + y^2) + \frac{1}{2} m\omega_z^2 z^2. \tag{5.2.1}$$

We assume that the single-atom wavefunction is localized in one of the potential minima, describing the ground-state of the hamiltonian $\mathcal{H}_0^{(h)} = -\frac{\hbar^2}{2m}\nabla^2 + V_{trap}^{(h)}(\mathbf{r})$. We then assume a gaussian ansatz of the form

$$\phi(x,y,z) = \left[\frac{2^3\kappa^2\eta^3}{\pi^3}\right]^{1/4} \exp\left[-\eta(x^2+y^2+\kappa^2z^2)\right], \tag{5.2.2}$$

where κ^2 was included to take into account the difference between ω_r and ω_z. By inserting the expression of Eq. 5.2.2 on the time-independent Schrödinger Equation with the hamiltonian given by $\mathcal{H}_0^{(h)}$, one obtains the equivalences $\eta = m\omega_r/(2\hbar)$ and $\kappa^2\eta = m\omega_z/(2\hbar)$, such that $\kappa^2 = \omega_z/\omega_r$, being called the "trap aspect ratio". In the following subsections, we analyze the expressions of the interaction and hopping parameters with the single-particle wavefunction just defined.

5.2.1 Interaction

The contact interaction, described by U_{sr} of Eq. 5.1.5, can be easily evaluated with the wavefunction $\phi(\mathbf{r})$ of Eq. 5.2.2 as:

$$\begin{aligned} U_{sr} &= g\int d\mathbf{r}\,\phi^4(\mathbf{r}) \\ &= g\left[\frac{2^3\kappa^2\eta^3}{\pi^3}\right]\int d\mathbf{r}\,\exp\left[-4\eta(x^2+y^2+\kappa^2z^2)\right] \\ &= g\kappa\left(\frac{\eta}{\pi}\right)^{3/2}. \end{aligned} \tag{5.2.3}$$

It is clear, from previous equation, that the signal of g immediately determines whether the contact interaction will be attractive (U_{sr} <0) or repulsive (U_{sr} >0). The fact that the s-wave interaction intensity grows with $\eta^{3/2}$ also makes sense, since it would mean that the two atoms involved are more closely-localized.

The evaluation of the dipole-dipole interaction yields a much more complicated scenario. The anysotropic and long-range natures of the interaction make difficult the task to come up with an analytical solution. However, as will shown now, it is still possible to reduce the dimensionality of the original integral involved from 6 to 1 and make the calculation easier. Since U_{ij} is a two-body effect, we will consider two single-particle functions $\phi_i(\mathbf{r})$ and $\phi_j(\mathbf{r'})$, separated by a distance $2d$. For simplicity, we take the axes (**x**, **y**, **z**) such that **y** connects the central region of both gaussian distributions. We also assume that both wavefunctions are centered at $z = z' = 0$ and that all the dipoles are aligned to the **z**-direction (see Fig. 5.1).

To evaluate integrals involving $|\mathbf{r}-\mathbf{r'}|^{-3/2}$, it is usually convenient to go to Fourier space - this is the case for U_{ij}. Therefore, we first define $n(\mathbf{r},d) \equiv \phi^2(x,y+d,z)$, such that the Fourier transform of $n(\mathbf{r},0)$ will be given by:

$$\tilde{n}(\mathbf{q}) = \int d\mathbf{q}\; n(\mathbf{r},0)e^{-i\mathbf{q}.\mathbf{r}} = \exp\left[-\frac{q_1^2+q_2^2}{8\eta} - \frac{q_3^2}{8\kappa^2\eta}\right]. \tag{5.2.4}$$

The Fourier transform of $V_{dd}(\mathbf{r}-\mathbf{r'})$ can be shown to be [81]:

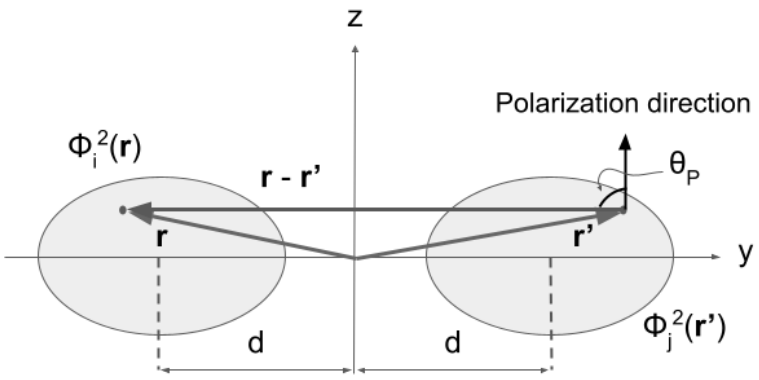

Figure 5.1: Illustration of the two-body, dipole-dipole interaction generically described by U_{ij} of Eq. 5.1.5. The apparent change of θ_P with both $\mathbf{r}$ and $\mathbf{r'}$ makes the anysotropic character of U_{ij} easily noticeable.

$$\tilde{V}_{dd}(\mathbf{q}) = \int d\mathbf{r}\; V_{dd}(\mathbf{r}-\mathbf{r'})e^{-i\mathbf{q}.\mathbf{r}} = C_{dd}\left(\cos^2\alpha - \frac{1}{3}\right), \tag{5.2.5}$$

where the dependence on $\mathbf{r}-\mathbf{r'}$ of Eq. 5.2.5 is reduced to a dependence on $\mathbf{q}$. With this, the total expression for U_{ij} can be rewritten as:

$$U_{ij} = \frac{1}{(2\pi)^3}\int d\mathbf{q}\; \tilde{V}_{dd}(\mathbf{q})\; \tilde{n}^2(\mathbf{q})\; e^{-2iq_2 d}. \tag{5.2.6}$$

In cylindrical coordinates, the above integral reduces to:

$$U_{ij} = \frac{C_{dd}}{4\pi}\int_0^\infty dr\; \left[\frac{4\kappa}{3}\sqrt{\frac{\eta}{\pi}} - e^{\frac{r^2}{4\kappa^2\eta}} r\;\mathrm{erfc}\left(\frac{r}{2\kappa\sqrt{\eta}}\right)\right] r\; e^{-\frac{r^2}{4\eta}} J_0(2rd), \tag{5.2.7}$$

where $\mathrm{erfc}(x) = 1-\mathrm{erf}(x)$ is the complementary error function and $J_p(x)$ is the Bessel function of first kind with index p. Here, it is valid to highlight that, for $d \to 0$ - i.e. the particles are located at the same site - the expression of Eq. 5.2.7 reduces to:

$$U_{dip} = \lim_{d\to 0} U_{ij} = -\frac{C_{dd}}{3g}\; f(\kappa)\; U_{sr}, \tag{5.2.8}$$

where the function $f(\kappa)$ associates the geometry of $\phi(\mathbf{r})$ with the dipolar interaction and is given by [81]:

$$f(\kappa) = \frac{1+2\kappa^2}{1-\kappa^2} - \frac{3\kappa^2\tanh^{-1}\sqrt{1-\kappa^2}}{(1-\kappa^2)^{3/2}}.$$

The previous equation predicts some interesting limiting cases for $f(\kappa)$. First, if $\kappa = 1$, $f(\kappa) = 0$. This would be the equivalent to a completely-symmetric wavefunction $\phi(\mathbf{r})$, and a vanishing D.D.I ($U_{dip} = 0$). Second, if $\kappa \to 0$ ("cigar"), $f(\kappa) \to 1$, which results in a maximally atractive D.D.I. ($U_{dip} < 0$). Finally, for $\kappa \to \infty$ ("pancake"), $f(\kappa) \to -2$, such that the D.D.I. is maximally repulsive ($U_{dip} > 0$). Fig. 5.2 illustrates the D.D.I. operator of the EBH Hamiltonian (Eq. 5.1.6).

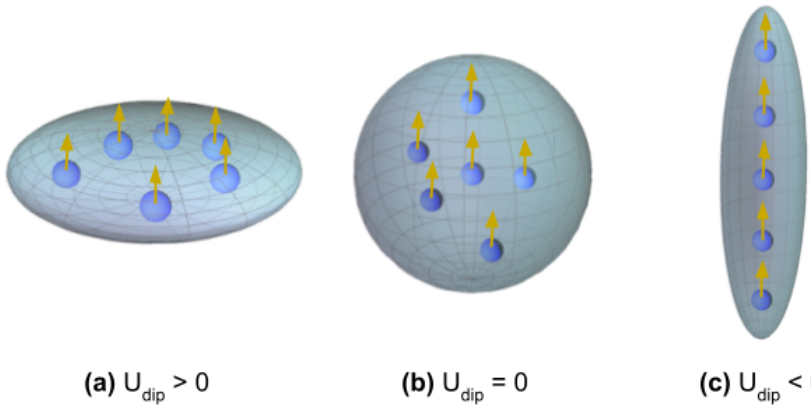

Figure 5.2: Illustration of the dipole-dipole interaction of the EBH Hamiltonian (Eq. 5.1.6). Panel **(a)** depicts a pancake-shaped trapping potential ($\kappa^2 > 1$), which implies in a repulsive D.D.I.. Panel **(b)** illustrates a symmetric (spherical) trapping potential ($\kappa^2 = 1$), such that the resulting dipolar interaction is zero. The case illustrated on panel **(c)** is related to a cigar-shaped trapping potential, such that $\kappa^2 < 1$, where the dipoles are in the so-called "head-to-tail" configuration, yielding an overall attractive dipolar interaction. For all the cases, the blue spheres represent (classically) the individual atoms on a potential minimum, with the yellow arrows being their permanent magnetic dipole. These atoms are surrounded by a plot of the corresponding single-atom density function $\phi^2(\mathbf{r})$ (not necessarily in scale).

5.3 INTEGRABLE COUPLING

After an algebrical manipulation, the hamiltonian of Equation 5.1.6 can be rewritten as:

$$H = \frac{U_0 - U_{12}}{4}(N_1 + N_3 - N_2 - N_4)^2 - \frac{J}{2}[(a_1 + a_3)(a_2^\dagger + a_4^\dagger) + \text{h.c.}] + (U_0 - U_{13})(N_1 N_3 + N_2 N_4) - \frac{U_{12} + U_0}{4} N^2. \tag{5.3.1}$$

Since $[H, N] = 0$, the last term in the previous equation can be ignored, since it is constant and would imply on a global phase to the system. Also, the hamiltonian of Equation 5.3.1 is the same as the one of Equation 2.2.2, provided that:

$$U_0 - U_{13} = 0. \tag{5.3.2}$$

The Equation 5.3.2 states the "integrability condition" for the physical system, described by the EBH hamiltonian, and is illustrated in Figure 5.3. Once fulfilled, the hamiltonian becomes the same as the one of Equation 2.2.2, where U is defined as: $U = \frac{1}{4}(U_{12} - U_0)$. As demonstrated in the next Chapter, by satisfying the condition stated on Equation 5.3.2 one also determines the required intensity of the trapping scheme.

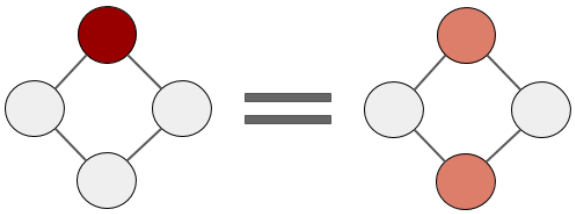

Figure 5.3: Illustration of the integrability condition. The circles represent the four sites, and the lines depict the nearest-neighbors tunneling. The onsite interaction (U_0), composed of dipole-dipole and contact interaction, is depicted in red; the dipolar interaction between diagonal sites (U_{13}) is depicted in orange. The system becomes integrable when $U_0 = U_{13}$ and J is recognized as $2J_{ij}$, with i, j nearest-neighbors. This can be done, in principle, by choosing a value for the s-wave scattering length a and varying the trapping frequencies of the system up to the point where the interaction energies U_0 and U_{13} match. Such method is presented with more details on Sec. 6.3.

5.3.1 Breaking of integrability

The protocols for NOON-state generation proposed on Sec. 3.3 rely on the ability to perform controllable breaks on the integrability. These are generated by introducing an imbalance in the trapping potential (see Sec. 6.3) $V_{\text{break}}(\mathbf{r})$ at specific times, "on purpose", giving raise to terms

$$\epsilon_i \equiv \int d\mathbf{r}\, \phi_i(\mathbf{r}) V_{\text{break}}(\mathbf{r}) \phi_i(\mathbf{r}) \tag{5.3.3}$$

that do not hold the same value for every i. This generates the operator $H_b = \sum_i \epsilon_i N_i$ that destroys the symmetry of the integrable Hamiltonian H, effectively breaking the system's integrability.[1]. The numerical values of $\{\epsilon_i\}$ and their relation with the terms μ and ν employed in the previous protocols are calculated on Sec. 6.3, taking into account a specific trapping scheme.

[1] We observe that the breaking of integrability has also been discussed in other physical scenarios (see, for instance [82, 83, 84])

Chapter 6

Experimental feasibility

In this chapter, we present a possible way of achieving integrability - and, ultimately, making our quantum device - on the lab. Based on the realization of ultracold atoms trapped in "optical lattices", we show how to fulfill the integrability condition by controlling the imbalance between contact and dipolar atomic interactions, and how this is related to the usual controllable trapping parameters. Finally, we also demonstrate specific calculations of the first-principles hamiltonian constants, whose values are similar to the ones employed in the previous Chapters. Some of the developments presented in this Chapter are based on private notes received from Prof. Leandro H Ymai.

6.1 Optical dipole trap

A usual sequence in experiments of ultracold atoms starts by cooling the atomic ensemble (which ultimately means lowering its average kinectic energy) with resonant light. Through absorption and (spontaneous) re-emission of light inciding on three perpendicular directions, the atoms on the ensemble become, on average, slower (and therefore, colder). Such a process does not trap the atoms at a specific region of space. Instead, it is usually employed as a preliminary step such that the atoms are captured by the desired trapping mechanism with a high probability and efficiency (which would not be the case with large velocities). The latter can be accomplished by different methods - including, for example, Magnetic Traps [85, 86] and Atom Chips [87] -; however, in this section I will briefly discuss a trapping scheme that is performed with off-resonant laser light.

The Optical Dipole Trap (ODT) [88] relies on the interaction between light (far from resonance) and the atom's electric dipole. The physics of the ODT is usually discussed in the context of the "AC Stark effect". In this case, the atom is thought to behave like an oscillator in the presence of radiation. We start by writing the electric field $\mathbf{E}$ as:

$$\mathbf{E}(\mathbf{r},t) = \left[\tilde{E}(\mathbf{r})e^{-i\omega t} + \tilde{E}^{*}(\mathbf{r})e^{i\omega t}\right]\hat{e}_{L}, \tag{6.1.1}$$

where $\tilde{E}(\mathbf{r})$ represents the amplitude of the electric field in space, ω is the oscillation frequency and $\hat{e}_{L}$ stands for the polarization vector. The atom-light coupling can then be described in terms of the electric dipole interaction:

$$V_{al} = -\mathbf{d}.\mathbf{E}, \tag{6.1.2}$$

where $\mathbf{d}$ stands for the atomic electric dipole operator. We consider that the atom is in the dressed-state [89] $|g\rangle$, with energy $E_g \pm \hbar\omega$. As mentioned before, this method is based on light with an off-resonance frequency, such that no real transitions between the ground- and excited-states are expected. Therefore, we employ a second-order time-independent perturbation theory to find the energy shift δE_g from the atomic ground-state energy. The generical expression reads:

$$\begin{aligned}\delta E_g &= \sum_e \left[\frac{\langle e|\mathbf{d}.\mathbf{E}^*|g\rangle\langle g|\mathbf{d}.\mathbf{E}|e\rangle}{E_g - E_e - \hbar\omega} + \frac{\langle e|\mathbf{d}.\mathbf{E}|g\rangle\langle g|\mathbf{d}.\mathbf{E}^*|e\rangle}{E_g - E_e + \hbar\omega}\right] \\ &= \sum_e \left[\frac{|\langle e|\mathbf{d}.\mathbf{e}_L|g\rangle|^2}{E_g - E_e - \hbar\omega} + \frac{|\langle e|\mathbf{d}.\mathbf{e}_L|g\rangle|^2}{E_g - E_e + \hbar\omega}\right]|\tilde{E}(\mathbf{r})|^2.\end{aligned} \tag{6.1.3}$$

From equation above, one notices that the off-resonant light that interacts with the atom induces virtual transitions between the ground-state $|g\rangle$ and the excited states $|e\rangle$, then decaying back to the ground-state. This can be compared to the classical picture of the eletric field inducing a dipole moment on the atom [90], which oscillates with the light intensity. The excited-state decaying rate is not being taking into account on Eq. 6.1.3, but it should be. This can be done by adding an imaginary energy related to the decay rate of the excited states. Considering Γ_e as the decaying rate from state $|e\rangle$, the lifetime of the excited states can be considered in the calculation through the simple transformation $E_e \to E_e - i\hbar\Gamma_e/2$. Then, defining $\omega_e \equiv (E_e - E_g)/\hbar$ as the frequency associated with the transition between the states $|g\rangle$ and $|e\rangle$, we can rewrite Eq. 6.1.3 as:

$$\begin{aligned}\delta E_g &= -\frac{1}{\hbar}\sum_e \left[\frac{|\langle e|\mathbf{d}.\mathbf{e}_L|g\rangle|^2}{\omega_e - \omega - i\Gamma_e/2} + \frac{|\langle e|\mathbf{d}.\mathbf{e}_L|g\rangle|^2}{\omega_e + \omega - i\Gamma_e/2}\right]|\tilde{E}(\mathbf{r})|^2 \\ &= -\alpha(\omega)|\tilde{E}(\mathbf{r})|^2,\end{aligned} \tag{6.1.4}$$

where the complex polarizability of the atom ($\alpha(\omega)$) was introduced. We now divide the analysis between the real and imaginary parts of the energy shift δE_g. Defining $V_{\mathrm{ODT}}(\mathbf{r})$ as the conservative potential generated by the atom-light interaction, we can related it with the real part of $\alpha(\omega)$, reading:

$$\begin{aligned}V_{\mathrm{ODT}}(\mathbf{r}) &= -\frac{1}{2\epsilon_0 c}\mathrm{Re}\{\alpha(\omega)\}\, I(\mathbf{r}) \\ &= \sum_e \frac{3\pi c^2}{2\omega_e^3}\left(\frac{\Gamma_e}{\omega - \omega_e} - \frac{\Gamma_e}{\omega + \omega_e}\right) I(\mathbf{r}), \\ &\approx \sum_e \frac{3\pi c^2}{2\omega_e^3}\left(\frac{\Gamma_e}{\Delta_e}\right) I(\mathbf{r}),\end{aligned} \tag{6.1.5}$$

where we defined $I(\mathbf{r}) \equiv 2\epsilon_0 c|\tilde{E}(\mathbf{r})|^2$ as the intensity of the electric field (and of the laser), $\Delta_e \equiv \omega - \omega_e$ as the detuning from resonance and we employed the rotating-wave approximation ($\Delta_e \ll \omega_e$). Even being off-resonant, the light field that interacts with the atom is still able to induce some photon scattering by the atom, causing its heating and potential lost from the trap [90]. The scattering rate -

$\Gamma_{sc}(\mathbf{r})$ - is related to the imaginary part of δE_g. With a similar calculation to the one employed at Eq. 6.1.5, one can arrive at:

$$\Gamma_{sc}(\mathbf{r}) \approx \sum_e \frac{3\pi c^2}{2\hbar\omega_e^3}\left(\frac{\Gamma_e}{\Delta_e}\right)^2 I(\mathbf{r}). \tag{6.1.6}$$

When comparing Eqs. 6.1.5 and 6.1.6, one may notice that, while $V_{ODT}(\mathbf{r})$ scales with $\sum_e I(\mathbf{r})/\Delta_e$, $\Gamma_{sc}(\mathbf{r})$ scales with $\sum_e I(\mathbf{r})/\Delta_e^2$, where ω_e was omitted just to increase readability. This has two interesting consequences. The first one is that $V_{ODT}(\mathbf{r})$ is attractive (i.e. provides trapping) only for $\sum_e 1/\Delta_e < 0$. By considering ω much closer to a given resonance $\omega_{e'}$ than the other ones, this would mean basically that $V_{ODT}(\mathbf{r})$ is attractive for $\Delta_{e'} < 0$, which is usually called a "red-detuned" condition. The second one is that, in order to increase $V_{ODT}(\mathbf{r})$ while decreasing $\Gamma_{sc}(\mathbf{r})$, one should increase simultaneously $I(\mathbf{r})$ and Δ_e.

In the case of a gaussian beam propagating towards the $\mathbf{z}$ direction, the intensity $I(\mathbf{r})$ is expressed by:

$$I(\mathbf{r}) = \frac{2P}{\pi w_0^2\left[1+\left(\frac{z}{z_R}\right)^2\right]}\exp\left[-\frac{2}{w_0^2}\frac{r^2}{1+\left(\frac{z}{z_R}\right)^2}\right],$$

where P is the power of the laser beam, w_0 is its minimum waist (see Figure 6.1 for more details), $z_R = \pi w_0^2/\lambda$ is the so-called "Rayleigth length" for which $I(0,0,z_R) = \frac{I_0}{2}$, where $I_0 \equiv \frac{2P}{\pi w_0^2[1+(z^2/z_R^2)]}$, and λ is the beam's wavelength. We may rewrite Equation 6.1.5 as:

$$V_{ODT}(\mathbf{r}) = -\frac{V_0}{\left[1+\left(\frac{z}{z_R}\right)^2\right]}\exp\left[-\frac{2}{w_0^2}\frac{1}{1+\left(\frac{z}{z_R}\right)^2}\right], \tag{6.1.7}$$

where we define the trapping potential depth V_0 in terms of the beam's power and waist and the atom's transitions:

$$V_0 = \frac{3Pc^2}{w_0^2}\sum_e \frac{1}{\omega_e^3}\left(\frac{\Gamma_e}{\omega-\omega_e} + \frac{\Gamma_e}{\omega_e+\omega}\right). \tag{6.1.8}$$

6.2 Optical Lattice

Due to the high levels of parameter control, "optical lattices" stand as one of the most prominent ways of performing atom-trapping. Is this method, the interference pattern of two or more counter-propagating laser beams generates an artificial "crystal of light", where the atoms get trapped on the potential minima (called "wells" or "sites").

Considering two counterpropagating beams on the $\mathbf{x}$ direction with a very large waist ($w \gg \lambda$), the laser field intensity can be written approximately as:

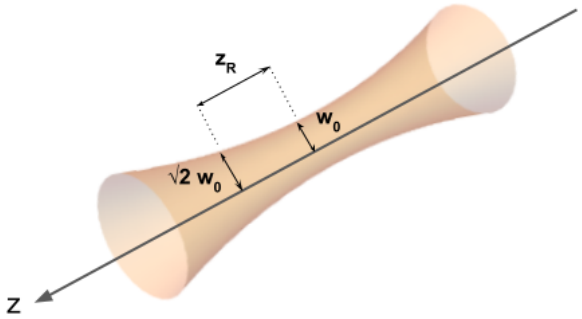

Figure 6.1: Illustration of a gaussian beam. The beam's waist, w_0, is given by the radius of the disk-section where the beam has the highest power, while z_R refers to the "distance" between the regions where the radius is w_0 and $\sqrt{2}w_0$.

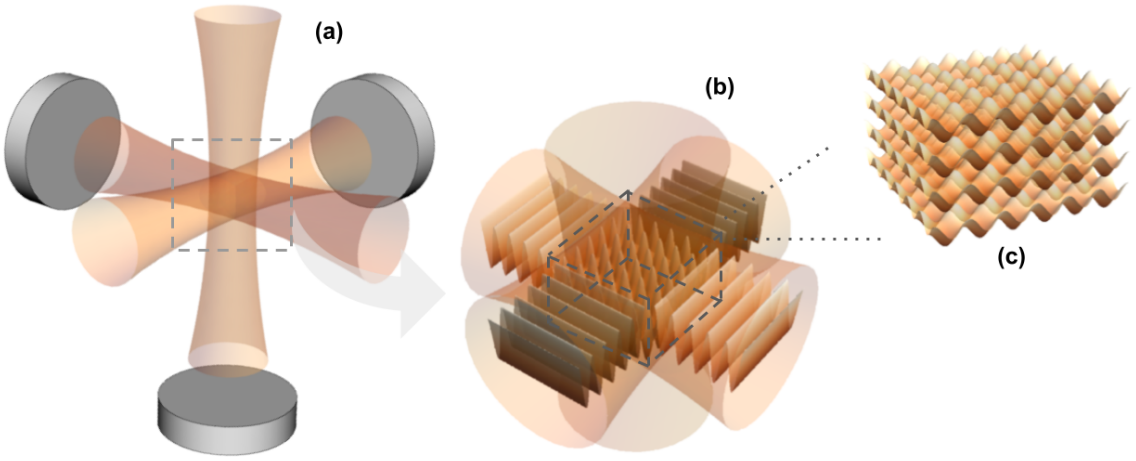

Figure 6.2: Representation of the 3D optical lattice. Panel **(a)** depicts the three sets of counter-propagating beams that cross each other at 90, where the silver cylinders represent the mirrors. A zoomed region is shown on Panel **(b)**, where the sine-like function the beam's electric field is drawn for the horizontal beams (for better visualization, this was not shown for the vertical one). The region at which the three beams encounter is where the 3D optical-lattice is located, as illustrated on Panel **(c)**, where each "slice" represent a 2D lattice for a fixed z.

$$\begin{aligned} I(x,t) &= \left(\sqrt{I_0}\cos(\omega t - kx) + \sqrt{I_0}\cos(\omega t + kx)\right)^2 \\ &= I_0\left[\cos^2(\omega t - kx) + \cos^2(\omega t + kx) + 2\cos(\omega t - kx)\cos(\omega t + kr)\right] \\ &= I_0\left[\cos^2(\omega t - kx) + \cos^2(\omega t + kx) + \cos(2\omega t) + \cos(2kx)\right], \end{aligned} \tag{6.2.1}$$

where $k \equiv 2\pi/\lambda$ is the wavevector, and λ is the beam's wavelength. By performing a time-average of the field $I(x,t)$, we obtain:

$$I(x) = \frac{\omega}{2\pi}\int_0^{2\pi/\omega} I(x,t) = I_0\left[1 + \cos\left(2kx\right)\right]. \tag{6.2.2}$$

A 3D optical lattice is obtained when three sets of counterpropagating beams cross each other at 90. In real experiments, these beams are usually retrorreflected with precisely aligned mirrors. Fig. 6.2 illustrates this process and the resulting 3D lattice. For all beams with the same wavelength, the potential V_{OL} generated will be given by:

$$\begin{aligned} V_{\mathrm{OL}}(\mathbf{r}) &= -\frac{V_0}{2}\left[3 + \cos(2kx) + \cos(2ky) + \cos(2kz)\right] \\ &= V_0\left[\sin^2(kx) + \sin^2(ky) + \sin^2(kz)\right]. \end{aligned} \tag{6.2.3}$$

It necessary to highlight that the expression of Equation 6.2.3 is strictly valid only on the central part of the optical lattice. This is due to the fact that the gaussian beam intensity varies along the beam, even in the cases where $w \gg \lambda$. In the next subsection, a special kind of optical lattice (called "superlattice") is introduced.

6.2.1 2D Superlattice

Being already a reality on cold-atoms experiments, the superlattice scheme is generated by the superposition of two optical lattices with wavelengths λ and 2λ - respectively refered to as "short" and "long" lattice. Following a similar procedure to the one employed for the Optical Lattice, it is possible to demonstrate that the trapping potential generated by a 2D superlattice is given by:

$$V_{\mathrm{SL}}^{2D}(\mathbf{r}) = -V_s\left[\sin^2(kx) + \sin^2(ky)\right] + V_l\left[\sin^2\left(\frac{kx}{2}\right) + \sin^2\left(\frac{ky}{2}\right)\right], \tag{6.2.4}$$

where V_s and V_l are, respectively, the "short" and "long" lattice potential depths. On Fig. 6.3, it is possible to see that the resulting structure resembles disconnected four-site plaquettes. This is very adequate for experimentally realizing systems of four wells on a closed configuration [74, 75]. In the next Section, a detailed proposal for an experimental setup will be provided along with the numerical evaluation of the Hamiltonian parameters.

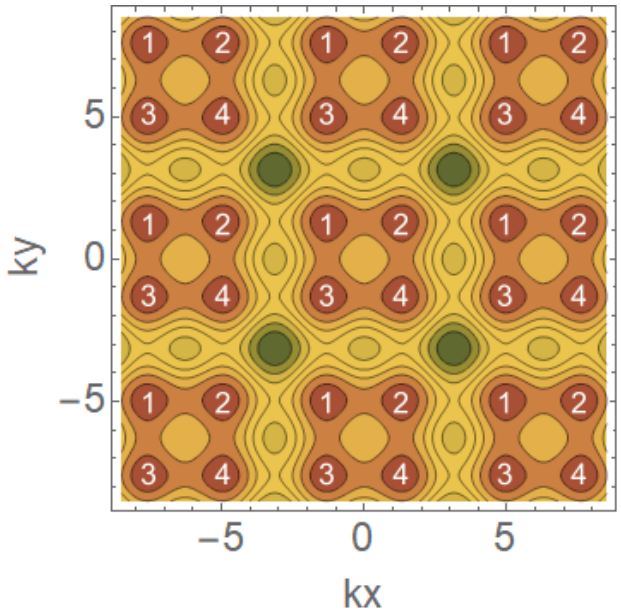

Figure 6.3: 2D superlattice. The disconnected four-site square plaquettes are generated by superimposing two complete, 2D optical lattices generated with beams with wavelengths λ and 2λ.

6.3 PHYSICAL DESIGN

The integrable model that describes our quantum device presents isotropic tunneling rates and the same interaction-energy scaling on each of the four sites. Due to the lifetime of the atoms in the lattice - and to increase usefulness for the proposed device applications -, one should consider a trapping scheme that provides the highest control on the hamiltonian parameters together with the lowest-possible values for the characteristic protocols time t_m, which depends not only on the initial number of atoms on classes "A" and "B" (respectively M and P), but also on the interaction and tunneling parameters. Therefore, in order to decrease t_m, it is necessary to simultaneously increase U and J. This justifies the choice realization that provides really short distances between the sites, which allows to enhance the D.D.I. and the tunneling rate simultaneously.

Hence, we propose that the four-well integrable model may be realized with the isotope ^{164}Dy of the highly magnetic atom Dysprosium [90], trapped in one of the square plaquettes generated by a superlattice with $V_s = V_l \equiv V_0$. The atom's permanent magnetic moment is given by $\mu \sim 9.93\ \mu_B$, where $\mu_B = 9.274 \times 10^{-24}$ J/T is the Bohr's magneton. For the trapping scheme, the characteristic wavelength used is $\lambda = 532$ nm, since both λ and 2λ had been already employed for optical-dipole trapping the isotope [91]. Besides that, in order to provide both **z**-confinement and controllability on the trap aspect ratio (and therefore in the system's interactions), an aditional 1D lattice on the **z**-direction with a wavelength 2λ is considered with a potential depth V_v given by $V_v/V_0 = 1.123$, implying $\kappa^2 \sim 0.53$ (cigar-shaped trap, see Fig. 5.2). Therefore, considered a single layer along z, we may write the trapping potential as:

$$V_{\text{trap}}(\mathbf{r}) = -V_0\left[\sin^2(kx) + \sin^2(ky)\right] + V_0\left[\sin^2\left(\frac{kx}{2}\right) + \sin^2\left(\frac{ky}{2}\right)\right] + \frac{1}{2}m\omega_z^2 z^2, \tag{6.3.1}$$

with $\omega_z \equiv (V_v k^2/(2m))^{1/2}$. The separation between the nearest-neighbors sites on a single plaquette is given by $l = \lambda/(2\delta)$, where $\delta \equiv (1 - 1/(2\pi))^{-1}$ is a correction obtained when expanding the previous equation in harmonic approximation, and causes the lattice sites within a plaquette to slightly approach each other. Figure 6.4 depicts the complete trapping scheme considered for the next calculations.

Measurement procedure

As assumed in Chapter 3, the measurements are done on a localized (site "3") and nondestructive manner, such that no atom losses are induced. This imposes some difficulties, since direct measurements on (super)lattice environments may easily induce the so-called photoassisted (PA) collisions, which causes the release of atom-pairs from the trap. Although undesired for the measurements of the proposed quantum devices, this effect can be used to selectively empty neighboring plaquettes to the one of interest. This is done by having a gradient of the magnetic-field strength on the **x-y** plane, causing a Zeeman-splitting that varies with the position of the atoms. Then, an adjustment of the laser frequency is done such that it matches the (chosen) transition frequency only in the desired lattice site [74, 75].

In order to avoid the PA effect, we propose that a off-resonant, Faraday Imaging is performed. This method is based on the Faraday effect, which states that a linearly-polarized light undergoes a rotation on the polarization direction when passing through a material with a magnetic field component along the light propagation axis. According to [77], the polarization rotation of a single site can be measured with linearly-polarized off-resonant light, and the allignment can be performed with a Digital Micromirror Device (DMD) (see Chapter 7 for more details).

6.3.1 Integrability condition

On the previous Chapter, the EBH model was introduced as a requirement for the realization of the integrable model with bosonic atoms. This is due to the fact that the model's Hamiltonian predicts interaction between atoms from different sites - as expressed in terms $\propto N_i N_j$, with $i \neq j$. An algebraic rearrangement of the Hamiltonian leads to the condition expressed on Eq. 5.3.2. As will be demonstrated now, the satisfaction of this equation not only guarantees integrability to the system, but also sets, automaticaly, the beams' intensities (by means of the trapping frequencies ω_r and ω_z).

Although very simple (and not at all optimized), the "method" to solve Eq. 5.3.2 is divided in four steps, in order to make the explanation clearer:

(i) set the value for the s-wave scattering length;
(ii) choose a value for the radial trapping frequency ω_r (since $\kappa^2 \sim 0.53$, ω_z is also set by this);
(iii) evaluate U_{13} and U_0 for the previous parameters and using the single-particle wavefunctions $\phi_i(\mathbf{r})$;
(iv) check if $U_{13} = U_0$; if not, repeat steps (ii) and (iii).

As the example that approximately reproduces the values for U and J employed in the calculations so far, we consider $a = 32.5\ a_0$, where a_0 is the Bohr's radius (~ 52.9 pm). Following the steps

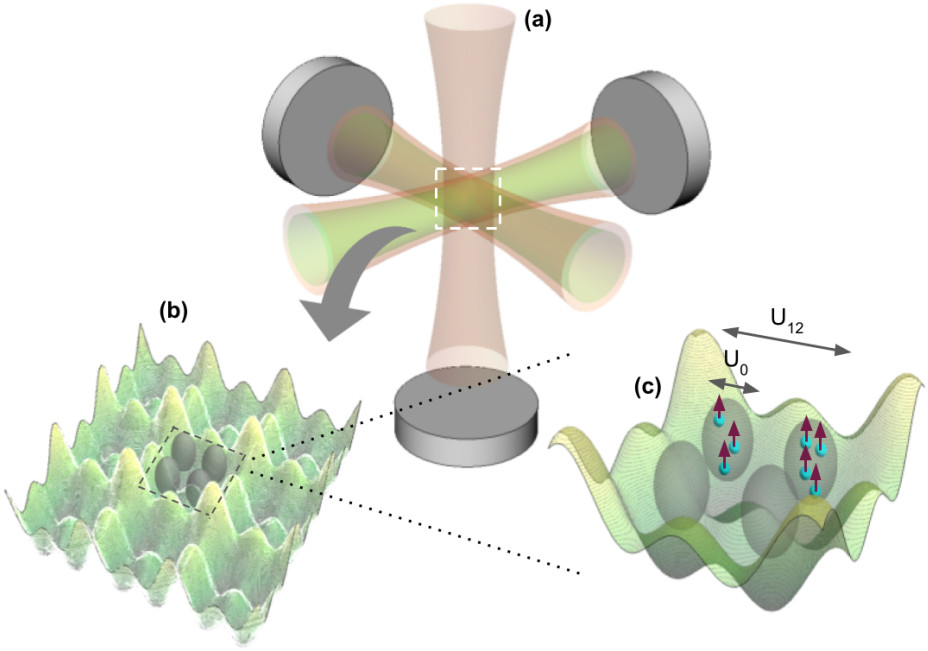

Figure 6.4: Complete trapping scheme. Graphic representation of the potential $V_{\text{trap}}(\mathbf{r})$ of Eq. 6.3.1. Panel **(a)** depicts the four sets of retrorreflected beams, which effectively generate two superimposed 2D optical lattices along **x-y**, with wavevectors k and $k/2$. The $\lambda = 1064$ nm and $\lambda = 532$ nm beams are illustrated, respectively, in orange and green. The vertical beam represents the 1D optical lattice along **z**. Panel **(b)** shows the general potential landscape generated in a single layer of the vertical lattice. Only one of the square plaquettes is occupied and realizes the four-well integrable model. On panel **(c)**, the gray ellipsoids represent $|\phi_i(\mathbf{r})|^2$ for $\kappa^2 \sim 0.53$. The atoms and their permanent magnetic dipole are alligned towards **z** and are depicted, respectively, as cyan spheres and purple arrows. The whole picture of this panel characterizes a Fock state $|4,3,0,0\rangle$, an onsite interaction given by U_0 and a nearest-neighbors D.D.I. given by U_{12} (which is the same for other nearest-neighbors). To keep readability, the diagonal D.D.I. was not depicted.

previously described, one obtains U_0 and U_{13} with respect to ω_r, which is depicted on Fig. 6.5. The point at which the two curves touch corresponds to $\omega_r \approx 2\pi \times 51.11$ kHz. By employing Eqs. 5.2.3, 5.2.7 and 5.2.8, the EBH parameters are evaluated to $U_0/\hbar = U_{13}/\hbar \approx 244.41$ Hz and $U_{12}/\hbar \approx 663.79$ Hz, which results in $U/\hbar \approx 104.85$ Hz. The hopping parameter J can be calculated with the expression for J_{ij} on Eq. 5.1.4, recognizing $J = 2J_{ij}$ with any i,j nearest-neighbors. This yields $J/\hbar \approx 71.62$ Hz.

6.3.2 Breaking of integrability

As described on Sec. 5.3, the controllable breaking of integrability can be generated by introducing an imbalance on the trapping potential at specific times. Based on the literature [75], we propose that this can be accomplished by means of a third, (much) weaker 2D optical lattice with a wavelength of 2λ. Calling V_b the depth of the potential generated by this third lattice, we can write its expression as:

$$V_{\text{break}}(\mathbf{r}) = V_b \left[\sin^2\left(\frac{kx}{2} + \varphi\right) + \sin^2\left(\frac{ky}{2} \pm \varphi\right) \right], \tag{6.3.2}$$

where the signal on the second φ depends on whether the imbalance is created between sites "1" and "3" or between sites "2" and "4". In order to conserve (on average) the potential depth, we consider

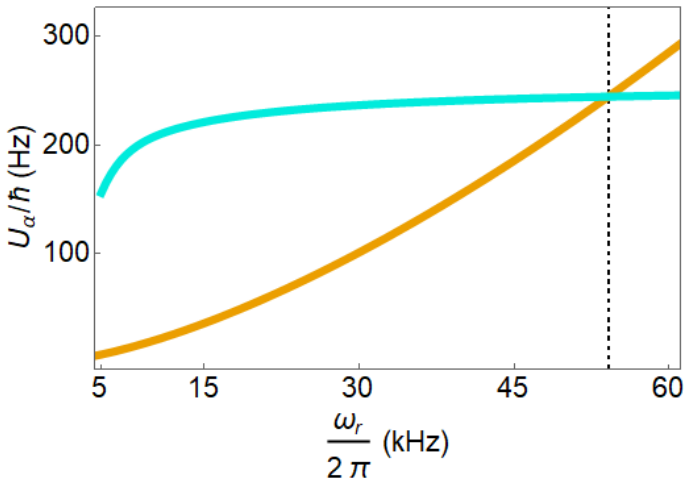

Figure 6.5: Fulfillment of integrability condition. After setting the s-wave scattering length $a = 32.5\ a_0$, the interaction parameters U_0 (orange line) and U_{13} (cyan line) are evaluated for different values of the radial trapping frequency ω_r. The value for ω_r that guarantees the system's integrability is extracted from the point where $U_0 = U_{13}$, and is given by $\omega_r \approx 2\pi \times 51.11$ kHz (dotted, black line). The Hamiltonian parameters can then be calculated from this point, resulting in $U/\hbar = 104.85$ Hz and $J/\hbar = 71.62$ Hz. See text for more details.

that V_l is lowered to $V_l - V_b$ when the third lattice is turned on. The introduction of this lattice then causes an effective imbalance of Δ between sites "1-3" or "2-4", where $\Delta \equiv 2V_b \sin(\pi/(2\delta))\sin(2\theta)$. This is illustrated in Fig. 6.6 (shown just for $k_x x$). By introducing the expression above for $V_{\text{break}}(\mathbf{r})$ with $-\varphi$ on Eq. 5.3.3, we can explicitly calculate the terms $\{\epsilon_i\}$, which read:

$$\epsilon_1 = \epsilon_3 = C \qquad \epsilon_2 = C + \frac{\Delta}{2} e^{-\frac{k^2}{8\eta}} \qquad \epsilon_4 = C - \frac{\Delta}{2} e^{-\frac{k^2}{8\eta}}, \tag{6.3.3}$$

where we defined $C \equiv V_b \left[1 - e^{-\frac{k^2}{8\eta}} \cos\left(\frac{\pi}{2\delta}\right)\cos(2\theta)\right]$. Then, the Hamiltonian implementation of these terms will be:

$$\begin{aligned} H_{\text{break}} &= \sum_i \epsilon_i N_i \\ &= CN + \underbrace{\frac{\Delta}{2} e^{-\frac{k^2}{8\eta}}}_{\equiv \mu} (N_2 - N_4)\,. \end{aligned} \tag{6.3.4}$$

The first term leads to a global phase and, therefore, can be ignored. In the second term, we identify $\mu \equiv \Delta\, e^{-k^2/8\eta}/2$. By considering $V_b = 10^{-3} V_0$ and $\varphi = 15$ mrad [75], the numerical evaluation of μ leads to $\mu/\hbar \approx 30$ Hz (the exact same procedure can be employed to evaluate ν).

6.3.3 Deviations from the integrability condition

The previousy-developed breaking of integrability comes from the introduction of an imbalance in the system's trapping potential on a controllable manner. There is, however, the possibility of the system having its integrability broken on an unintended manner, which can reduce its coherence time and mitigate its ability to perform interferometry and NOON-state generation with high fidelities

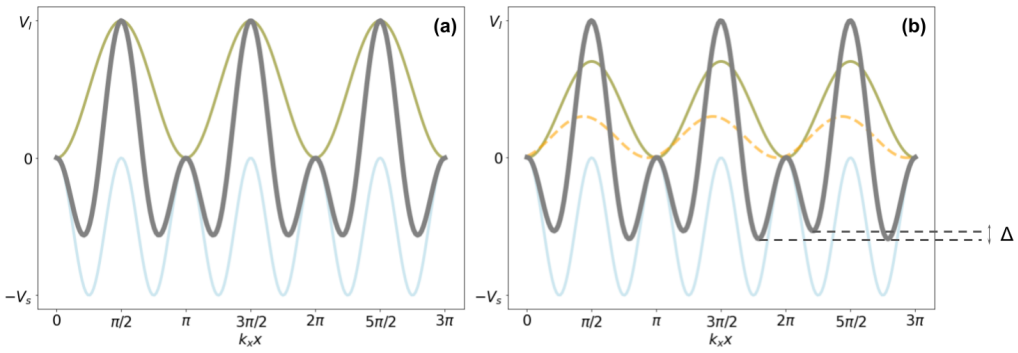

Figure 6.6: Breaking of integrability in the superlattice. Panel **(a)** illustrates a single vertical layer of the trapping potential $V_{\text{trap}}(\mathbf{r})$ generated by the superlattice along **x**. The potential of the long and short lattices are represented, respectively, in green and blue, resulting in the total potential given by the gray line. On panel **(b)**, the contribution of a third, weaker and misaligned lattice (orange, dashed) is taken into account, which effectively causes an imbalance between second-nearest-neighbors corresponding to Δ. The plot on Panel **(b)** is done just for clarification purposes, and the potential generated by the misaligned lattice, corresponding to $V_b = 0.3V_0$, is different than the one actually employed for calculations. See text for more details.

and probabilities. Besides the symmetric structure of the model's Hamiltonian, the general condition for integrability, as state on Eq. 5.3.2, relies on exactly matching the onsite (contact + dipole-dipole) interaction with the D.D.I. between diagonal sites. Supposing that this is not the case and that there's a small difference (called "error") ξ between the interaction energies, the integrability condition of Eq. 5.3.2 turns into a "mismatch condition"

$$U_0 - U_{13} = \xi, \tag{6.3.5}$$

and the system's Hamiltonian becomes:

$$H' = H + \xi(N_1 N_3 + N_2 N_4). \tag{6.3.6}$$

In the expression above, H is the integrable hamiltonian with parameters U', J', $\mu' = \nu'$ recalculated due to the mismatch ξ. Such an error is responsible for a fidelity drop on the quantum device's functionalities, as shown in Fig. 6.8. Following the exact same procedure as the one done for the integrability condition, we now calculate the set of parameters $\{\xi^{\pm}, U'(\xi^{\pm}), J'(\xi^{\pm}), \mu'(\xi^{\pm}) = \nu'(\xi^{\pm})\}$ for errors $\xi^{+}/\hbar = -\xi^{-}/\hbar$ ranging from 0 to 4 Hz (the equivalent of $\sim 4\%$ of U). For each value of ξ, one has to calculate the "mismatch condition" as in Eq. 6.3.5 to obtain the corresponding radial frequency ω_r' and then evaluate the set of parameters above. The results are shown in Fig. 6.7.

Robustness against errors

Now, a quantitative estimate is presented for the robustness of the quantum devices against undesired perturbations, which will be done in terms of calculated fidelities between analytical quantum states (obtained from the unperturbed H_{eff}) and the numerical ones obtained with different values of ξ. Let us start by defining

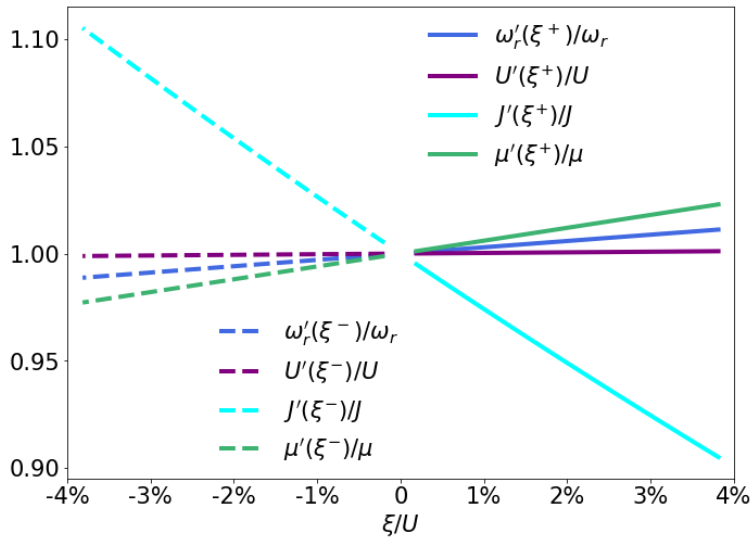

Figure 6.7: Hamiltonian parameters as a function of error $\xi^{\pm}$. The "mismatch condition" was employed for each value of ξ, and the resulting value for $\omega_r'(\xi)$ was subsequently used to calculate the numerical values of $U'(\xi)$, $J'(\xi)$ and $\mu'(\xi) = \nu'(\xi)$, which are plotted in this picture divided by their integrable counterparts.

$$\mathcal{U}'(t,\mu',\nu',\xi) \equiv \exp\Big(-\frac{it}{\hbar}\Big[H' + \mu'(\xi)(N_2 - N_4) + \nu'(\xi)(N_1 - N_3) + \xi(N_1N_3 + N_2N_4)\Big]\Big),$$

where H' is the integrable Hamiltonian with $U'(\xi)$ and $J'(\xi)$. Then, the error is taken into account in the following way:

(i) The precision on seting the trapping frequency is such that the values $\omega_r^{(-)}$ and $\omega_r^{(+)}$ are precisely achieved, but the intermediate value $\omega_r = 1/2(\omega_r^{(-)} + \omega_r^{(+)})$ is not;

(ii) The laser intensity oscillates between the two closest values to the one that generates ω_r, which induces an oscillation between $\omega_r^{(-)}$ and $\omega_r^{(+)}$, which is then translated into an oscillation between the respective errors generated ξ^- and ξ^+;

(iii) When evaluating the fidelity for a given error value ξ, the parameter is alternated between ξ^- and ξ^+ during the time-evolution, together with the corresponding Hamiltonian couplings, if $t \sim$ seconds (e.g. during the time-evolution with $\mu' = \nu' = 0$). During the phase-related evolutions ($\mu \neq 0$ or $\nu \neq 0$), we consider a usual time-evolution with $\xi = 0$ and the average of the parameters obtained with ξ^- and ξ^+: $\{\bar{U}', \bar{J}', \bar{\mu}' = \bar{\nu}'\}$.

(iv) The relevant times t_m, t_μ and t_ν are always calculated with the averaged parameters $\{\bar{U}', \bar{J}', \bar{\mu}' = \bar{\nu}'\}$.

For example, for a time-evolution from $t = 0$ to $t = t_m$ with s oscilations, with $\mu' = \nu' = 0$, and following the aforementioned procedure, one should consider an operator $\mathcal{U}_s$ given by:

$$\mathcal{U}_s = \prod_{i=1}^{s} \mathcal{U}\left(\frac{t_m}{2s}, 0, 0, \xi^-\right)\mathcal{U}\left(\frac{t_m}{2s}, 0, 0, \xi^+\right). \tag{6.3.7}$$

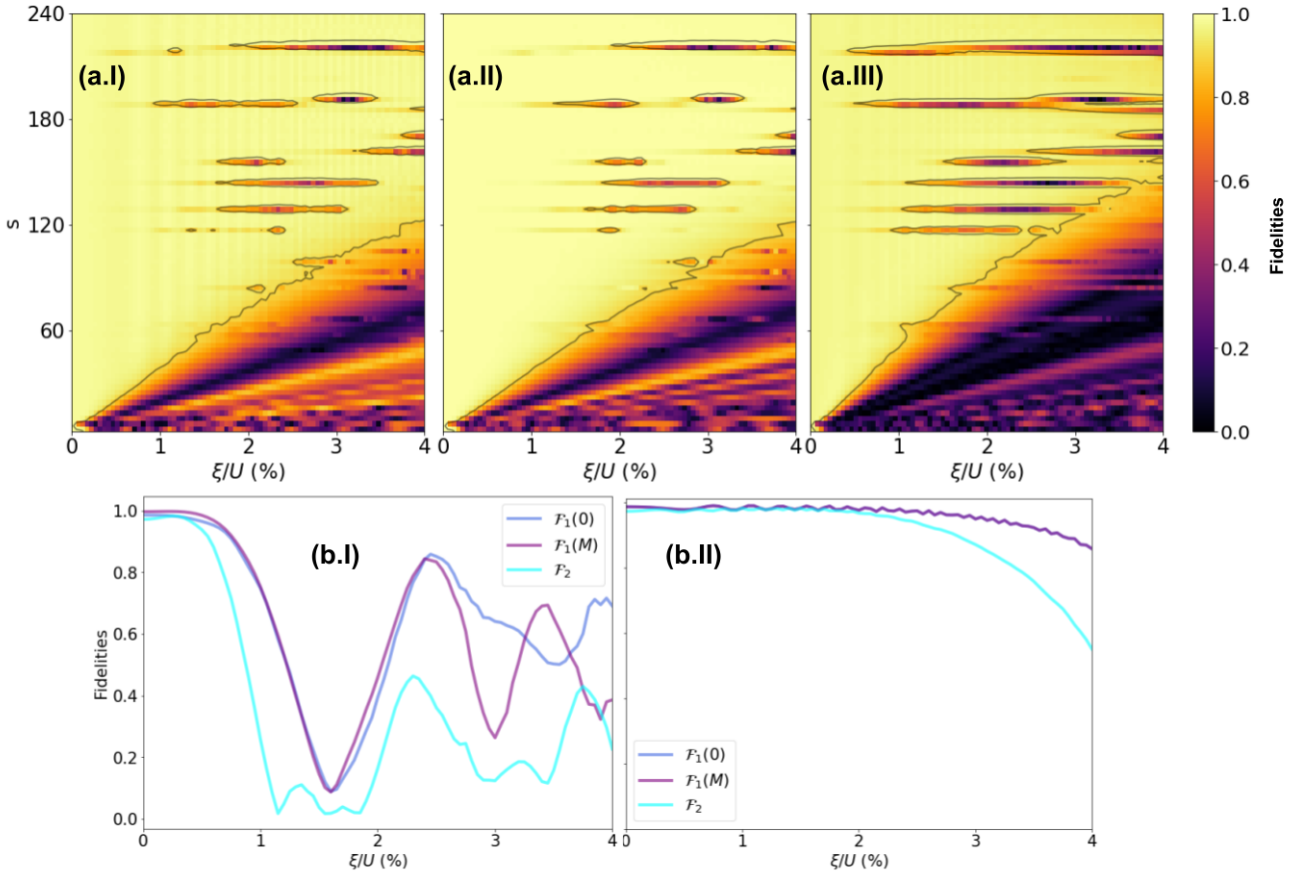

Figure 6.8: Robustness of the NOON state generator against errors. The initial state is given by $|\Psi_0\rangle = |M,P,0,0\rangle$, with $M = 4$, $P = 11$, and we consider a phase codification of $P\theta = \pi/2$. The relative error ξ/U is taken into account by calculating the quantum dynamics with the Hamiltonian H' of Eq. 6.3.6, following the assumptions that lead to the time-evolution operator $\mathcal{U}_s$ of Eq. 6.3.7. Panels **(a.I)** and **(a.II)** depict the fidelities of the NOON states obtained with Protocol I when measuring $r = 0$ and $r = M$ bosons at site "3", respectively. Panel **(a.III)** shows the fidelities of the NOON state obtained with Protocol II. On all three panels, the solid line demarcates the regions where the fidelity is higher than 0.9. The two lower panels illustrate the fidelities for both protocols with respect to ξ/U, for $s = 30$ **[(b.I)]** and $s = 120$ **[(b.II)]**.

On Fig. 6.8, the fidelities related to the NOON state generator device are plotted with respect to the number of oscillations s and the relative error ξ/U. We notice that the solid line (corresponding to fidelities higher than 0.9) separates the figure on two regions, characterizing the system as "robust" ("not robust") in the region of "high" ("low") fidelities.

Chapter 7

Digital Micromirror Device

The ability to manipulate and tailor laser light with control and precision is of great importance, with applications that range from biomedical imaging [92] to probing the roton mode and supersolid excitation spectrum on dipolar gases [93, 94]. In the reffered literature, the main component for light tailoring is an instrument called Digital Micromirror Device (DMD).

In this Chapter, we discuss the working principles of a DMD, along with a possible application to the theoretical proposals presented in previous chapters. The results presented here were obtained during the time I was working as a visiting Master's student in the Erbium Group of Prof. Francesca Ferlaino, in the University of Innsbruck, and are part of the output of my fellowship (which resulted in the Python package "pythonDMDapp"[1]).

7.1 Working principles

As the name suggests, the Digital Micromirror Device (DMD) is an equipment composed of an arrange of small mirrors. For example, the model V9501 from Vialux [2] is composed of 1920×1080 mirrors, each one of them being square and with an area of 10.8×10.8 $(\mu\text{m})^2$ (Panel **(b)** of Fig. 7.1 illustrates the device and the mirror area). Since this is the model I worked with, I will assume these physical characteristics henceforward.

The key aspect of the DMD is that each mirror can be individually controlled in two positions ("on" and "off"), which enables the loading of an incredible variety of patterns into the DMD's RAM memory, allowing for their subsequent use. By inputting a partern into it, the DMD reflects the incoming beam shaped by the on/off mirrors (which effectively "cut" the beam in the desired shape). This is illustrated in Panel **(a)** of Fig. 7.1. However, due to aberrations on the reflection area (mainly due to the DMD construction), such a beam is reflected with phase aberrations. For applications where the reflected beam is employed after being focused down by a lens (such as the Faraday measurement described in Chapter 6), such phase aberrations cause deformations on the beam when it arrives at the lens' focus [95]. In order to be able to correct these deformations (and, as will be shown later, to effectively displace the beam's position at focus), it is convenient to work with the so-called "Lee

[1] https://github.com/danielsgrun/pythonDMDapp
[2] https://vialux.de/en/superspeed-specification.html

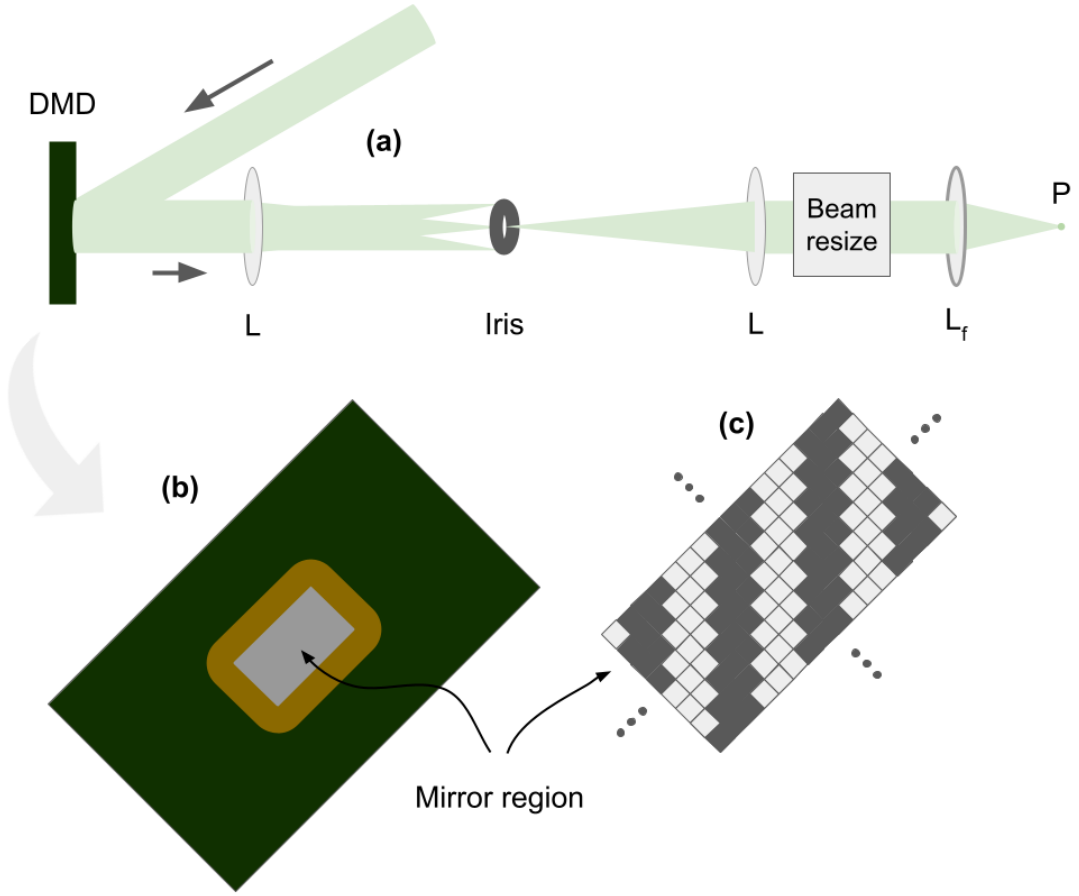

Figure 7.1: Working principles of the DMD. On panel **(a)**, the incoming beam is reflected by the DMD, "cut" by the pattern $g\{f(x,y)\}$. Then, it is focused down by the first lens L, and the 1^{st}-order of diffraction is chosen on the focal point of L through an iris, and the resulting beam is collimated back to its previous radius by the second lens L. Afterwards, the beam can be resized to an "arbitrary" radius before being finally focused down by the final lens L_f onto the atomic ensamble. Panel **(b)** shows an illustration of the DMD. On a very simplified view, it is composed by an electronic circuit (green) and a mirror region (gray). There is also the "motherboard", that provides energy and receives the array-inputs from the computer, which is not depicted here. Panel **(c)** depicts a zoom into the mirror region, showing the individual mirrors on "on" (white) and "off" (gray) states, following a simple "Lee hologram" as presented in Eq. 7.1.1, with $\sigma(x,y) = 0$.

Holograms" [96]. This consists in considering an amplitude pattern $f(x,y)$ across the mirror region, given by:

$$f(x,y) = \frac{1}{2}\left[1 + \cos(k(x-y) - \sigma(x,y))\right], \tag{7.1.1}$$

where k can be arbitrarily chosen and $\sigma(x,y)$ is related to the local phase at each mirror on the DMD. Since the state of each mirror is either "on" (255) or "off" (0), it is necessary to perform a binarization g on the pattern $f(x,y)$, which becomes $g\{f(x,y)\}$, defined as:

$$g\{f(x,y)\} = \begin{array}{l} 255, \text{ if } f(x,y)>1/2 \\ 0, \text{ otherwise} \end{array}. \tag{7.1.2}$$

The desired pattern should then be generated within the background of the grating structure of previous equation. Panel **(c)** of Fig. 7.1 depicts an example of $g\{f(x,y)\}$ on the mirror region of the DMD.

7.2 Zernike polynomials

Phase correction

As mentioned before, an incident beam at the DMD will be reflected with phase aberrations caused by a range of factors (such as the own process of producing the instrument). In this case, the phase correction of a DMD consists in using a phase-map $\sigma(x,y)$ such that the beam shape at the final-lens' focus is correct. Such a phase map can be extracted by different means. One of them consists on varying mirror patches along the DMD mirror area, calculating the phase-difference between each patch and a previously-chosen central patch (more details on this method can be found in [95]). The other method - which I decided to work with - consists on generating a circular phase mask from Zernike Polynomials $Z_j(\rho,\phi)$ [1] [97] and optimizing the signal on the CCD by varying the phase mask on a loop. The idea is as follows:

(i) a circular phase mask $\sigma(x,y)$ is generated as $\sigma(x,y) = \sum_j c_j Z_j(\rho,\phi)$;

(ii) the full pattern $g\{f(x,y)\}$ is uploaded into the DMD, and a CCD captures the light in spot P (as shown in Panel **(a)** of Fig. 7.1);

(iii) an algorithm looks for the brighest pixel count in the previously-captured image, and stores its value;

(iv) for a fixed j 2, c_j is varied until the brighest pixel is generated, and the whole process is repeated for a different j 2.

Panel **(a)** of Fig. 7.2 shows a real example of the pattern $g\{f(x,y)\}$ corrected by the phase-map $\sigma(x,y)$ obtained from the phase correction procedure. There, the whole (elliptical) beam is within a circular region of $r = 400$ px (mirrors) taken into account for the phase-correction. One may notice that the phase-map $\sigma(x,y)$ also acts on regions where no beam reaches - which therefore are not trustful for

[1] The single index "j" refers to the OSA/ANSI convention.

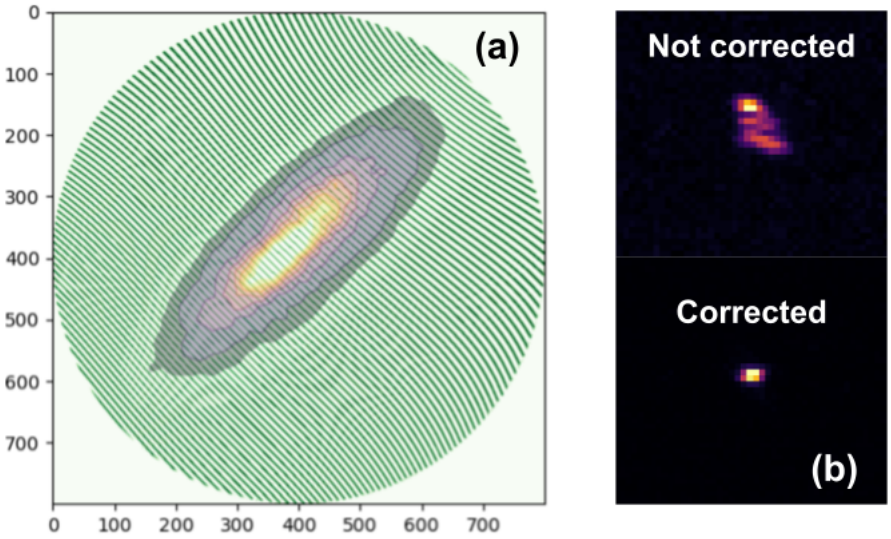

Figure 7.2: Phase-correction. Panel **(a)**: DMD hologram with the obtained $\sigma(x,y)$ for phase correction. The green slits represent the "on" mirrors on a binarized amplitude function $g\{f(x,y)\}$, while the pattern in the middle represents the beam position on the DMD, called "intensity map". This map can be obtaining by considering different patches of 20×20 mirrors and putting them in the "on" position on an alternating manner, measuring the pixel counts at the CCD on each step. The amplitude function $g\{f(x,y)\}$ is shown with the phase correction $\sigma(x,y)$, which causes a distortion in it that becomes more visible further from the beam, which implies a higher phase deformation on the edges of the DMD (since the beam is somewhat centralized). Panel **(b)** shows the beam detected by the CCD at the focus of a $f = 75$ mm lens, before (top) and after (bottom) the phase correction of Panel **(a)**.

further applications where such regions are used (and a new phase-map should be extracted taking them into account). Panel **(b)** of Fig. 7.2 shows the obtained pixel counts for the beam by the CCD, at the focus of a $f = 75$ mm lens, before and after the phase-correction shown in Panel **(a)**.

Beam displacement

As commented on Chapter 6, the Faraday Imaging may be employed for single site measurement with the use of a DMD, allowing for a controllable displacement and allignment of the focalized beam. This can be done by constructing a phase map with the 1st- and 2nd-order Zernike polynomials and using them in the amplitude function $g\{f(x,y)\}$.

The first polynomial is given by $Z_0(\rho,\phi) = 1$ and, therefore, corresponds to a constant phase, whereas $Z_1(\rho,\phi)$ and $Z_2(\rho,\phi)$, expressed as

$$Z_1(\rho,\phi) = 2\rho\ \sin\phi \qquad Z_2(\rho,\phi) = 2\rho\ \cos\phi, \tag{7.2.1}$$

are related to linear phase-gradients on two perpendicular directions. It is precisely these phase-gradients that cause the beam to suffer a displacement on the lens' focus. Since the coefficients $\{c_j\}$ may take any real value, such displacement can be performed in an almost continuous way. Therefore, combined with an off-resonant beam for Faraday imaging, this may also constitute a useful method for the technique. Fig. 7.3 shows the **x-y** displacement (at focus) of the beam reflected by the DMD with a circular pattern with $r = 1.62$ mm.

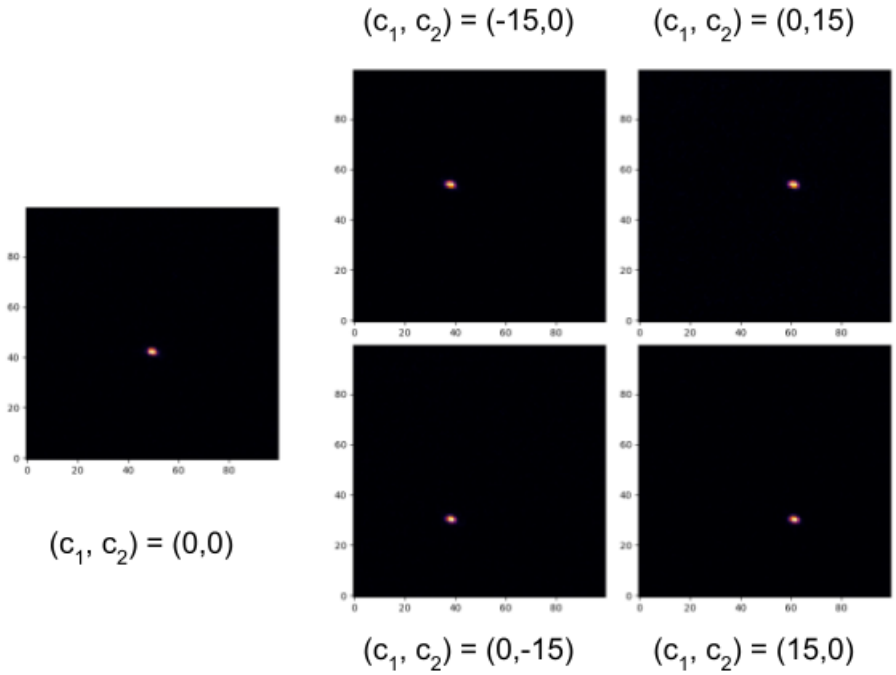

Figure 7.3: Beam displacement with Zernike Polynomials. The beam comes out of the DMD in a circular shape with $r = 1.62$ mm. The constants c_j refer to the coefficients of the respective Zernike Polynomial Z_j, which are employed as a circular phase-mask at the DMD, with $r = 1.62$ mm. The axes are in units of "pixel" (each pixel $= 5.3$ μm). The contributions of Z_1 and Z_2 can be independently varied, and the beam's displacement at focus can be arbitrarily chosen.

Chapter 8

Conclusion

In this work we have investigated the properties and possible applications of the four-well integrable model, which describes the quantum tunneling and the interaction of bosons in a square plaquette. More specifically, on Chapter 2 we have studied its integrability, which means that if the model is integrable, it possesses four conserved quantities - the total number of atoms N, the Hamiltonian H and the two "conserved charges" Q_1 and Q_2. In the so-called "resonant regime" - achieved with a special choice for the Hamiltonian's couplings and the initial state -, it is possible to employ the conserved charges as an effective hamiltonian, enabling the development of analytical formulae for the system's quantum dynamics. These expressions proved to be helpful on the characterization of possible applications of the system as a quantum device.

When a NOON state is employed as the initial state, we demonstrated that the system operates interferometric activity with a sensitivity given by the Heisenberg uncertainty principle. Then, on Chapter 3 we showed that, for an initial Fock state, the system generates a NOON state by itself after a time-evolution depending on the Hamiltonian's interaction and tunneling parameters. For the specific Hamiltonian parameters employed, the characteristic time-scales are typically a few seconds. When comparing the results from the effective and physical Hamiltonians, these device applications demonstrated to have high values of fidelities and probabilities that are similar to the ones predicted.

On Chapter 4, the Von-Neumann entanglement entropy is evaluated for the proposed quantum devices. There, a counter-intuitive result is shown: even though the devices only work for a total number of particles N odd, the entanglement entropy between sites "1,3" and "2,4", after the characteristic time-evolution, is expected to reach the same numerical value regardless the parity of N. Such a result is really impressive, as it demonstrates that, for a given reduction of the density operator, two quantum states that are completely different may be related to the same Von-Neumann entropy, which exemplifies that not all entangled states are useful for the same purposes.

The equivalence between the theoretical Hamiltonian parameters and a possible experimental realization was estabilished through the extended Bose-Hubbard model. As shown in Chapter 5, for a trapping scheme that realizes atoms with alligned dipoles on a square plaquette, the condition for integrability comes from matching the eBH and the integrable Hamiltonians, which is accomplished by making the onsite and diagonal interactions the same. A possible realization in terms of opti-

cal superlattices is provided in Chapter 6, and the respective expression for the trapping potential is employed in order to numerically-evaluate the Hamiltonian parameters. In order to probe the system's robustness against imperfections on the integrable coupling, we also undertake numerical analysis by taking into account an error parameter. Supposing that it encompasses the instabilities in the laser beam's intensities, we consider that this parameter oscillates around zero. On this approach, the system demonstrates to be highly robust for errors up to a few percent of the interaction parameter if the error oscillates at least around 150 times during the characteristic time-scales involved.

Therefore, we expect that the results demonstrated in this Dissertation help to boost advances on the field of atomtronics. By stablishing a link between integrability and neutral-atom quantum information processing, the output presented here increases the prospects of building quantum machines with scalable and controllable characteristics enabled by property of integrability.

Bibliography

[1] S.N. Bose. Plancks Gesetz und Lichtquantenhypothese. *Zeitschrift für Physik*, 26:178–181, 1924.

[2] A. Einstein. Quantentheorie des einatomigen idealen gases. *Preussischen Akademie der Wissenschaften*, pages 3–14, 1925.

[3] M. H. Anderson, J. R. Ensher, M. R. Matthews, C. E. Wieman, and E. A. Cornell. Observation of bose-einstein condensation in a dilute atomic vapor. *Science*, 269(5221):198–201, 1995.

[4] K.B. Davis, M.-O. Mewes, M. R. Andrews, N. J. van Druten, D. S. Durfee, D. M. Kurn, and W. Ketterle. Bose-einstein condensation in a gas of sodium atoms. *Physical Review Letters*, 75(22):3969–3973, 1995.

[5] M. Albiez, R. Gati, J. Fölling, S. Hunsmann, M. Cristiani, and M. K. Oberthaler. Direct observation of tunneling and nonlinear self-trapping in a single bosonic josephson junction. *Physical Review Letters*, 95(1):010402–1–010402–4, 2005.

[6] H.A. Gersh and G.C. Knollman. Quantum cell model for bosons. *Physical Review*, 129(2):959–967, 1963.

[7] M.P.A. Fisher, P.B. Weichman, G. Grinstein, and D.S. Fisher. Boson localization and the superfluid-insulator transition. *Physical Review B*, 40(1):546–570, 1989.

[8] A.P. Tonel, J. Links, and A. Foerster. Quantum dynamics of a model for two josephson-coupled bose–einstein condensates. *Journal of Physics A: Mathematical and General*, 38(6):1235–1245, 2005.

[9] M. Greiner, O. Mandel, T. Esslinger, T.W. Hänsch, and Immanuel Bloch. Quantum phase transition from a superfluid to a mott insulator in a gas of ultracold atoms. *Nature*, 415:39–44, 2002.

[10] M. Greiner, O. Mandel, T.W. Hänsch, and Immanuel Bloch. Collapse and revival of the matter wave field of a bose–einstein condensate. *Nature*, 419:51–54, 2002.

[11] E. Schrödinger. Quantisierung als eigenwertproblem. *Annalen der Physik*, 384(4):361–376, 1926.

[12] E. Schrödinger. Quantisierung als eigenwertproblem. *Annalen der Physik*, 384(6):489–527, 1926.

[13] F.J. Dyson, E.H. Lieb, and B. Simon. Phase transitions in the quantum heisenberg model. *Physical Review Letters*, 37(3):120–123, 1976.

[14] R.G. Bowers and M.E. Woolf. Some critical properties of the heisenberg model. *Physical Review*, 177(2):917–932, 1969.

[15] H. Bethe. Zur theorie der metalle. *Zeitschrift für Physik*, 71:205–226, 1931.

[16] J.B. McGuire. Study of exactly soluble one-dimensional n-body problems. *Journal of Mathematical Physics*, 5(5):622–636, 1964.

[17] E.H. Lieb. Exact solution of the problem of the entropy of two-dimensional ice. *Physical Review Letters*, 18(17), 1967.

[18] C.N. Yang. Some exact results for the many-body problem in one dimension with repulsive delta-function interaction. *Physical Review Letters*, 19(23), 1967.

[19] R.J. Baxter. *Exactly Solved Models in Statistical Mechanics*. Academic Press, 1989.

[20] L.D. Fadeev. Algebraic aspects of the Bethe ansatz. *International journal of modern physics A*, 10(13):1845–1878, 1995.

[21] H. Babujian, A. Foerster, and M. Karowski. Exact form factors of the su(n) gross-neveu model and 1/n expansion. *Nuclear Physics B*, 825(3):396–425, 2010.

[22] A. Foerster and M. Karowski. Algebraic properties of the bethe ansatz for an spl(2,1)-supersymmetric t-j model. *Nuclear Physics B*, 396(2):611–638, 1993.

[23] V.E. Korepin and F.H.L. Essler. *Exactly solvable models of strongly correlated electrons*. World Scientific, 1994.

[24] M.T. Batchelor and A. Foerster. Yang–baxter integrable models in experiments: from condensed matter to ultracold atoms. *Journal of Physics A: Mathematical and Theoretical*, 49(17):173001, 2016.

[25] A. Foerster and E. Ragoucy. Exactly solvable models in atomic and molecular physics. *Nuclear Physics B*, 777(3):373–403, 2007.

[26] J. Links, A. Foerster, A.P. Tonel, and G. Santos. The two-site bose-hubbard model. *Annales Henri Poincaré*, 7:1591–1600, 2006.

[27] D. Rubeni, A. Foerster, E. Mattei, and I. Roditti. Quantum phase transitions in bose–einstein condensates from a bethe ansatz perspective. *Nuclear Physics B*, 856(3):698–715, 2012.

[28] G. Santos, A.P. Tonel, A. Foerster, and J. Links. Classical and quantum dynamics of a model for atomic-molecular bose-einstein condensates. *Physical Review A*, 73(2):023609, 2006.

[29] G. Santos, A. Foerster, J. Links, E. Mattei, and S. R. Dahmen. Quantum phase transitions in an interacting atom-molecule boson model. *Physical Review A*, 81(6):063621, 2010.

[30] M. Duncan, A. Foerster, J. Links, E. Mattei, N. Oelkers, and A. Tonel. Emergent quantum phases in a heteronuclear molecular bose–einstein condensate model. *Nuclear Physics B*, 767(3):227–249, 2007.

[31] L.H. Ymai, A.P. Tonel, A. Foerster, and J. Links. Quantum integrable multi-well tunneling models. *Journal of Physics A: Mathematical and Theoretical*, 50(26):264001, 2017.

[32] K.Wittmann W. Quebra da integrabilidade para um modelo de tunelamento quântico de três poços. Master's thesis, UFRGS, 2017.

[33] K. Wittmann W., L.H. Ymai, A.P. Tonel, J. Links, and A. Foerster. Control of tunneling in an atomtronic switching device. *Communications Physics*, 1(91), 2018.

[34] J.E. Lilienfeld. Device for controlling electric current. US Patent number 1900018A, 3 1933.

[35] T.H. Maiman. Stimulated optical radiation in ruby. *Nature*, 187:493–494, 1960.

[36] C.E. Shannon. A mathematical theory of communication. *The Bell System Technical Journal*, 27(3):379–423, 1948.

[37] J.P. Dowling and G.J. Milburn. Quantum technology: the second quantum revolution. *Philosophical transactions of the royal society A*, 361(1809):1655–1674, 2003.

[38] P.W. Shor. Algorithms for quantum computation: discrete logarithms and factoring. In *Proceedings on 35th Annual Symposium on Foundations of Computer Science*, pages 124–134, 1994.

[39] R.P. Feynman. Simulating physics with computers. *International journal of theoretical physics*, 21:467–488, 1982.

[40] D. Jaksch, J.I. Cirac, P. Zoller, S.L. Rolston, R. Côté, and M.D. Lukin. Fast quantum gates for neutral atoms. *Physical Review Letters*, 85(10):2208–2211.

[41] I. Bloch, J. Dalibard, and W. Zwerger. Many-body physis with ultracold gases. *Reviews of Modern Physics*, 80(3):885–964.

[42] B.T. Seaman, M. Krämer, D.Z. Anderson, and M.J. Holland. Atomtronics: Ultracold-atom analogs of electronic devices. *Physical Review A*, 75(2), 2007.

[43] R.A. Pepino. Advances in atomtronics. *arXiv:2104.12239*.

[44] L. Amico et al. Roadmap on atomtronics: state of the art and perspective. *arXiv: 2008.04439*, 2020.

[45] L. Amico, G. Birkl, M. Boshier, and L.-C. Kwek. Focus on atomtronics-enabled quantum technologies. *New Journal of Physics*, 19, 2017.

[46] C. Ryu, P.W. Blackburn, A.A. Blinova, and M.G. Boshier. Experimental realization of Josephson Junctions for an atom SQUID. *Physical Review Letters*, 111(20), 2013.

[47] S. Pandey et al. Hypersonic bose–einstein condensates in accelerator rings. *Nature*, 570:205—-209, 2019.

[48] A.P. Tonel, L.H. Ymai, A. Foerster, and J. Links. Integrable model of bosons in a four-well ring with anisotropic tunneling. *Journal of Physics A: Mathematical and Theoretical*, 48(49):494001, 2015.

[49] D. Rubeni, J. Links, P. S. Isaac, and A. Foerster. Two-site bose-hubbard model with nonlinear tunneling: Classical and quantum analysis. *Phys. Rev. A*, 95:043607, 2017.

[50] E.R. Castro, J. Chavez-Carlos, I. Roditi, L.F. Santos, and J.G. Hirsch. Quantum-classical correspondence of a system of interacting bosons in a triple-well potential. *arXiv:2105.10515*, 2021.

[51] J.-S. Caux and J. Mossel. Remarks on the notion of quantum integrability. *Journal of Statistical Mechanics: Theory and Experiment*, 2011(02), 2011.

[52] G. Santos, A. Foerster, and I. Roditi. A bosonic multi-state two-well model. *Journal of Physics A: Mathematical and Theoretical*, 46(26):265206, 2013.

[53] A. P. Tonel, J. Links, and A. Foerster. Behaviour of the energy gap in a model of josephson coupled bose–einstein condensates. *Journal of Physics A: Mathematical and General*, 38(31):6879–6891, 2005.

[54] G. Santos, C. Ahn, A. Foerster, and I. Roditi. Bethe states for the two-site bose–hubbard model: A binomial approach. *Physics Letters B*, 746:186–189, 2015.

[55] D.S. Grün. Integrabilidade em modelos de tunelamento quântico. Bachelor's thesis, UFRGS, 2018.

[56] A.P. Tonel, L.H. Ymai, K. Wittmann.W., A. Foerster, and J. Links. Entangled states of dipolar bosons generated in a triple-well potential. *SciPost Physics Core*, 2(1), 2020.

[57] N.J. Lopes. Dinâmica em modelos de tunelamento quântico. Bachelor's thesis, UFRGS, 2020.

[58] A.A. Michelson and E.W. Morley. On the relative motion of the earth and the luminiferous ether. *American Journal of Science*, s3-34(203):333–345, 1887.

[59] G. Sagnac. L'ether lumineux demontre par l'effet du vent relatif d'ether dans un interferometre en rotation uniforme. *Comptes rendus de l'Académie des Sciences*, 157:708–710, 1913.

[60] B.C. Barish and R. Weiss. Ligo and the detection of gravitational waves. *Physics Today*, 52(10):44–50, 1999.

[61] R. Abbott et al. Observation of gravitational waves from two neutron star–black hole coalescences. *The Astrophysical Journal Letters*, 915(1):L5, 2021.

[62] M.O. Scully and M.S. Zubairy. *Quantum Optics*. Cambridge University Press, 1997.

[63] C.W. Helstrom. *Quantum detection and estimation theory*. Academic Press New York, 1976.

[64] H. Lee, P. Kok, and J.P. Dowling. A quantum Rosetta stone for interferometry. *Journal of Modern Optics*, 49(14–15):2325–2338, 2002.

[65] B.C. Sanders and G.J. Milburn. Optimal quantum measurements for phase estimation. *Physical Review Letters*, 75:2944–2947, 1995.

[66] Z.Y. Ou. Fundamental quantum limit in precision phase measurement. *Physical Review A*, 55:2598–2609, 1997.

[67] O. Carnal and J. Mlynek. Young's double-slit experiment with atoms: A simple atom interferometer. *Physical Review Letters*, 66:2689–2692, 1991.

[68] D.W. Keith, C.R. Ekstrom, Q.A. Turchette, and D.E. Pritchard. An interferometer for atoms. *Physical Review Letters*, 66:2693–2696, 1991.

[69] F. Riehle, Th. Kisters, A. Witte, J. Helmcke, and C.J. Bordé. Optical ramsey spectroscopy in a rotating frame: Sagnac effect in a matter-wave interferometer. *Physical Review Letters*, 67:177–180, 1991.

[70] M. Kasevich and S. Chu. Atomic interferometry using stimulated raman transitions. *Physical Review Letters*, 67:181–184, 1991.

[71] M. Meister, A. Roura, E.M. Rasel, and W.P. Schleich. The space atom laser: an isotropic source for ultra-cold atoms in microgravity. *New Journal of Physics*, 21(1), 2019.

[72] M.J. Mark, E. Haller, K. Lauber, J.G. Danzl, A.J. Daley, and H.-C. Nägerl. Precision measurements on a tunable mott insulator of ultracold atoms. *Physical Review Letters*, 107:175301, 2011.

[73] D.S. Grun, L.H. Ymai, K. Wittmann W., A.P. Tonel, A. Foerster, and J. Links. Integrable atomtronic interferometry. *arXiv:2004.11987*.

[74] B. Yang, H. Sun, and R. Ott et al. Observation of gauge invariance in a 71-site bose–hubbard quantum simulator. *Nature*, 587:392–396.

[75] B. Yang et al. Cooling and entangling ultracold atoms in optical lattices. *Science*, 369(6503):550–553, 2020.

[76] D.S. Grun, K. Wittmann W., L.H. Ymai, J. Links, and A. Foerster. Atomtronic protocol designs for noon states. *arXiv:2102.02944*.

[77] D. Okuno, Y. Amano, K. Enomoto, N. Takei, and Y. Takahashi. Schemes for nondestructive quantum gas microscopy of single atoms in an optical lattice. *New Journal of Physics*, 22(1):013041, 2020.

[78] L. Pezzè, A. Smerzi, M.K. Oberthaler, R. Schmied, and P. Treutlein. Quantum metrology with nonclassical states of atomic ensembles. *Review of Modern Physics*, 90:035005, Sep 2018.

[79] Cheng Chin, Rudolf Grimm, Paul Julienne, and Eite Tiesinga. Feshbach resonances in ultracold gases. *Reviews of Modern Physics*, 82:1225–1286, 2010.

[80] K. Góral, L. Santos, and M. Lewenstein. Quantum phases of dipolar bosons in optical lattices. *Physical Review Letters*, 88:170406, Apr 2002.

[81] T. Lahaye, C. Menotti, L. Santos, M. Lewenstein, and T. Pfau. The physics of dipolar bosonic quantum gases. *Reports on Progress in Physics*, 72(12):126401, nov 2009.

[82] P. Jung, R.W. Helmes, and A. Rosch. Transport in almost integrable models: Perturbed heisenberg chains. *Phys. Rev. Lett.*, 96:067202, 2006.

[83] B. Wilson, A. Foerster, C.C.N. Kuhn, I. Roditi, and D. Rubeni. A geometric wave function for a few interacting bosons in a harmonic trap. *Physics Letters A*, 378(16):1065–1070, 2014.

[84] I. Brouzos and A. Foerster. Trace of broken integrability in stationary correlation properties. *Phys. Rev. A*, 89:053623, 2014.

[85] J. Reichel and W. Hänsel T.W. Hänsch. Atomic micromanipulation with magnetic surface traps. *Physical Review Letters*, 83:3398–3401, Oct 1999.

[86] J. Fortágh and C. Zimmermann. Magnetic microtraps for ultracold atoms. *Reviews of Modern Physics*, 79:235–289, Feb 2007.

[87] J. Reichel and V. Vuletic. *Atom Chips*. Wiley, 2011.

[88] R. Grimm, M. Weidemüller, and Y.B. Ovchinnikov. Optical dipole traps for neutral atoms. volume 42 of *Advances In Atomic, Molecular, and Optical Physics*, pages 95–170. Academic Press, 2000.

[89] C. Cohen-Tannoudji, J. Dupont-Roc, and G. Grynberg. Atom–photon interactions: Basic processes and applications. *American Journal of Physics*, 61(6):572–572, 1993.

[90] C. Bouazza. *Ultracold dysprosium gas in optical dipole traps : control of interactions between highly magnetic atoms*. PhD thesis, Université Paris sciences et lettres, 2018.

[91] M. Wenzel. A dysprosium quantum gas in highly controllable optical traps. Master's thesis, Universität Stuttgart, 2015.

[92] Z. Zhuang and H.P. Ho. Application of digital micromirror devices (dmd) in biomedical instruments. *Journal of Innovative Optical Health Sciences*, 13(06):2030011, 2020.

[93] D. Petter, G. Natale, R.M.W. van Bijnen, A. Patscheider, M.J. Mark, L. Chomaz, and F. Ferlaino. Probing the roton excitation spectrum of a stable dipolar bose gas. *Physical Review Letters 122, 183401*, May 2019.

[94] D. Petter et al. Bragg scattering of an ultracold dipolar gas across the phase transition from bose-einstein condensate to supersolid in the free-particle regime. *Physical Review A*, 104:L011302, Jul 2021.

[95] D. Petter. Spatial modulation of light for ultracold gas experiments with erbium atoms. Master's thesis, Universität Innsbruck, 2015.

[96] W.-H. Lee. III computer-generated holograms: Techniques and applications. volume 16 of *Progress in Optics*, pages 119–232. Elsevier, 1978.

[97] Setting up a DMD/SLM: Aberration effects. https://www.wavefrontshaping.net/post/id/23. Accessed: 2021-08-01.

Appendix A

Analytical calculations

In this Appendix, we demonstrate the main anlytical formulae used in the text. The material presented here was based on private notes from Prof. Jon Links.

A.1 IMBALANCE QUANTUM DYNAMICS

A.1.1 Conserved charges and effective hamiltonian

The conserved charges of the Four-well Model, Q_1 and Q_2, are given by:

$$\begin{aligned} Q_1 &= \frac{1}{2}(N_1 + N_3) - \frac{1}{2}(a_1^\dagger a_3 + a_1 a_3^\dagger) \\ Q_1 &= \frac{1}{2}(N_2 + N_4) - \frac{1}{2}(a_2^\dagger a_4 + a_2 a_4^\dagger) \end{aligned} \tag{A.1.1}$$

It has been shown that, if the system is in the resonant regime (i.e. with a choice of parameters such that each different initial state corresponds to a different energy band), it's quantum dynamics may be completely described with an effective hamiltonian, H_{eff}. Considering an initial condition of the kind $|M,P,0,0\rangle$, with $M \equiv N - P$, the effective hamiltonian takes the form:

$$\begin{aligned} H_{eff} = &\frac{J^2}{16U}\left(\frac{P}{M-P+1} - \frac{P+2}{M-P-1}\right)(M - 2Q_1) \\ &+ \frac{J^2}{16U}\left(\frac{M+2}{M-P+1} - \frac{M}{M-P-1}\right)(M - 2Q_2) \\ &+ \frac{J^2}{16U}\left(\frac{M+2}{M-P+1} - \frac{M}{M-P-1}\right)[MP + 4Q_1Q_2 - 2PQ_1 - 2MQ_2] \end{aligned} \tag{A.1.2}$$

where U and J are, respectively, the interaction and hopping constants. The energy eigenvalues associated with (A.1.2), $\mathfrak{e}_{q_1,q_2}$, are given by:

$$\mathfrak{e}_{q_1,q_2} = \frac{J^2}{4U[(M-P)^2 - 1]}[(N+1)(q_1+q_2) - 2q_1q_2] \tag{A.1.3}$$

A.1.2 Autobasis construction

To make the calculations easier, we shall construct an eigenbasis of $\{Q_1, Q_2\}$, which we will denote as $\{|M,P,q_1,q_2\}\}$, defined as:

$$|M,P,q_1,q_2\} = \frac{C}{\sqrt{2^N}}(a_1^\dagger + a_3^\dagger)^{M-q_1}(a_1^\dagger - a_3^\dagger)^{q_1}(a_2^\dagger + a_4^\dagger)^{P-q_2}(a_2^\dagger - a_4)^{q_2}\,|0\rangle\,, \tag{A.1.4}$$

such that $H_{eff}|M,P,q_1,q_2\} = \mathfrak{e}_{q_1,q_2}|M,P,q_1,q_2\}$, and $C = \frac{1}{\sqrt{q_1!(M-q_1)!q_2!(P-q_2)!}}$. Since we intend to calculate the time evolution of the imbalance between wells 1-3 and 2-4, we ought to look at how the states defined in (A.1.4) transform under the operations of $N_1 - N_3$ and $N_2 - N_4$. First, we define:

$$\begin{aligned} b_1 &= \frac{1}{\sqrt{2}}(a_1 + a_3); \qquad & b_2 &= \frac{1}{\sqrt{2}}(a_1 - a_3); \\ b_3 &= \frac{1}{\sqrt{2}}(a_2 + a_4); \qquad & b_4 &= \frac{1}{\sqrt{2}}(a_2 - a_4), \end{aligned} \tag{A.1.5}$$

such that (A.1.4) may be rewritten as:

$$|M,P,q_1,q_2\} = C(b_1^\dagger)^{M-q_1}(b_2^\dagger)^{q_1}(b_3^\dagger)^{P-q_2}(b_4^\dagger)^{q_2}\,|0\rangle\,. \tag{A.1.6}$$

The expressions of $N_1 - N_3$ and $N_2 - N_4$ in terms of b_i, $b_i^\dagger$ become:

$$\begin{aligned} N_1 - N_3 &= b_1^\dagger b_2 + b_1 b_2^\dagger; \\ N_2 - N_4 &= b_3^\dagger b_4 + b_3 b_4^\dagger. \end{aligned} \tag{A.1.7}$$

Then, defining $M \equiv N - P$, the application of $N_1 - N_3$ on the state described by (A.1.6) will be:

$$\begin{aligned} &(N_1 - N_3)|M,P,q_1,q_2\} \\ &= C\left[(b_1^\dagger)^{M-q_1+1}b_2(b_2^\dagger)^{q_1} + b_1(b_1^\dagger)^{M-q_1}(b_2^\dagger)^{q_1+1}\right](b_3^\dagger)^{P-q_2}(b_4^\dagger)^{q_2}\,|0\rangle \\ &= C\left[(b_1^\dagger)^{M-(q_1-1)}q_1(b_2^\dagger)^{q_1-1} + (N-P-q_1)(b_1^\dagger)^{M-(q_1+1)}(b_2^\dagger)^{q_1+1}\right](b_3^\dagger)^{P-q_2}(b_4^\dagger)^{q_2}\,|0\rangle \\ &= \sqrt{q_1(M-q_1+1)}|N,P,q_1-1,q_2\} + \sqrt{(M-q_1)(q_1+1)}|N,P,q_1+1,q_2\}, \end{aligned} \tag{A.1.8}$$

where we used the following properties: $[b_i,(b_i^\dagger)^j] = j(b_i^\dagger)^{j-1}$, and $b_i\,|0\rangle = 0$. Similarly, by applying $(N_2 - N_4)$ into $|M,P,q_1,q_2\}$, we have:

$$(N_2 - N_4)|M,P,q_1,q_2\} = \sqrt{q_2(P-q_2+1)}|M,P,q_1,q_2-1\} + \sqrt{(P-q_2)(q_2+1)}|M,P,q_1,q_2+1\}, \tag{A.1.9}$$

which is a property we will use later. It is possible to rewrite the state of (A.1.4) as:

$$
\begin{aligned}
|M,P,q_1,q_2\} &= \frac{C(-1)^{q_1+q_2}}{\sqrt{2^N}} \sum_{i=0}^{M-q_1}\sum_{j=0}^{q_1} \binom{M-q_1}{i}\binom{q_1}{j}(-1)^j (a_1^\dagger)^i (a_3^\dagger)^{M-q_1-i}(a_1^\dagger)^j (a_3^\dagger)^{q_1-j} \\
&\qquad \sum_{k=0}^{P-q_2}\sum_{l=0}^{q_2} \binom{P-q_2}{k}\binom{q_2}{l}(-1)^l (a_2^\dagger)^k (a_4^\dagger)^{P-q_2-k}(a_2^\dagger)^l (a_4^\dagger)^{q_2-l}|0\rangle \\
&= \frac{C(-1)^{q_1+q_2}}{\sqrt{2^N}} \sum_{i=0}^{M-q_1}\sum_{j=0}^{q_1} \binom{M-q_1}{i}\binom{q_1}{j}(-1)^{j+l} (a_1^\dagger)^{i+j} (a_3^\dagger)^{M-i-j} \\
&\qquad \sum_{k=0}^{P-q_2}\sum_{l=0}^{q_2} \binom{P-q_2}{k}\binom{q_2}{l}(a_2^\dagger)^{k+l} (a_4^\dagger)^{P-k-l}|0\rangle
\end{aligned}
\tag{A.1.10}
$$

where we considered Newton's Binomial expansion: $(x+y)^n = \sum_{i=0}^{n}\binom{n}{i}x^{n-i}y^i$. Therefore, using $(a^\dagger)^r|0\rangle = \sqrt{r!}\,|r\rangle$, we can calculate the useful relations:

$$
\begin{aligned}
\langle M,P,0,0|M,P,q_1,q_2\} = \frac{C(-1)^{q_1+q_2}}{\sqrt{2^N}} &\sum_{i=0}^{M-q_1}\sum_{j=0}^{q_1}(-1)^j \binom{M-q_1}{i}\binom{q_1}{j}\sqrt{(M-i-j)!(i+j)!}\,\delta_{i+j,M} \\
&\sum_{k=0}^{P-q_2}\sum_{l=0}^{q_2}(-1)^l \binom{P-q_2}{k}\binom{q_2}{l}\sqrt{(P-k-l)!(k+l)!}\,\delta_{k+l,P}
\end{aligned}
$$

Now we replace C by its expression and simplify the summations with the Kronecker delta, obtaining:

$$
\begin{aligned}
\langle M,P,0,0|M,P,q_1,q_2\} &= \sqrt{\frac{M!P!}{2^N q_1!(M-q_1)!q_2!(P-q_2)!}} \\
&\qquad \sum_{j=0}^{q_1}(-1)^j \binom{M-q_1}{M-j}\binom{q_1}{j}\sum_{l=0}^{q_2}(-1)^l \binom{P-q_2}{P-l}\binom{q_2}{l} \\
&= \sqrt{\frac{M!P!}{2^N q_1!(M-q_1)!q_2!(P-q_2)!}},
\end{aligned}
\tag{A.1.11}
$$

where we used the Vandermonde Convolution: $\sum_{j=0}^{n}\binom{n}{j}\binom{m}{k-j} = \binom{n+m}{k}$.

By considering a similar procedure, we can calculate $\langle M,0,0,P|N,P,q_1,q_2\}$; using the results from (A.1.10), we get:

$$
\begin{aligned}
\langle M,0,0,P|N,P,q_1,q_2\} = \frac{C(-1)^{q_1+q_2}}{\sqrt{2^N}} &\sum_{i=0}^{M-q_1}\sum_{j=0}^{q_1}(-1)^{j+l} \binom{M-q_1}{i}\binom{q_1}{j}\sqrt{(M-i-j)!(i+j)!}\,\delta_{i+j,0} \\
&\sum_{k=0}^{P-q_2}\sum_{l=0}^{q_2} \binom{P-q_2}{k}\binom{q_2}{l}\sqrt{(P-k-l)!(k+l)!}\,\delta_{k+l,P}.
\end{aligned}
$$

Using the definition of C and simplifying the summations with the Kroenecker Deltas, we obtain the same result as (A.1.11), but with an extra $(-1)^{q_2}$ factor. Therefore:

$$\langle M,0,0,P|N,P,q_1,q_2\} = (-1)^{q_2}\sqrt{\frac{M!P!}{2^N q_1!(M-q_1)!q_2!(P-q_2)!}}. \tag{A.1.12}$$

A.1.3 Imbalance quantum dynamics

Using the effective hamiltonian H_{eff} described in (A.1.2), we calculate the time evolution of the operator $(N_1 - N_3)$ as:

$$
\begin{aligned}
(N_1 - N_3)(t) &= e^{iH_{eff}t}(N_1 - N_3)e^{-iH_{eff}t} \\
&= \sum_{p_1=0}^{M}\sum_{p_2=0}^{P}\sum_{q_1=0}^{M}\sum_{q_2=0}^{P} e^{i(\epsilon_{p_1,p_2}-\epsilon_{q_1,q_2})t} \\
&\qquad |N,P,p_1,p_2\}\{N,P,p_1,p_2|(N_1 - N_3)|M,P,q_1,q_2\}\{N,P,q_1,q_2| \\
&= \sum_{p_1=0}^{M}\sum_{p_2=0}^{P}\sum_{q_1=0}^{M}\sum_{q_2=0}^{P} e^{i(\epsilon_{p_1,p_2}-\epsilon_{q_1,q_2})t}|N,P,p_1,p_2\}\{N,P,p_1,p_2| \\
&\quad (\sqrt{q_1(M-q_1+1)}|N,P,q_1-1,q_2\} + \sqrt{(M-q_1)(q_1+1)}|N,P,q_1+1,q_2\})\{N,P,q_1,q_2| \\
&= \sum_{q_1=0}^{M}\sum_{q_2=0}^{P}\Bigg(e^{-i(\epsilon_{q_1,q_2}-\epsilon_{q_1-1,q_2})t}\sqrt{q_1(M-q_1+1)}|N,P,q_1-1,q_2\} \\
&\qquad + e^{-i(\epsilon_{q_1,q_2}-\epsilon_{q_1+1,q_2})t}\sqrt{(M-q_1)(q_1+1)}|N,p,q_1+1,q_2\}\Bigg)\{N,P,q_1,q_2|.
\end{aligned}
\tag{A.1.13}
$$

A.1.3.1 Simple initial state

The imbalance dynamics can be obtained by choosing an initial state $|\Psi_0\rangle$, such that $\langle N_1 - N_3\rangle(t) = \langle\Psi_0|(N_1 - N_3)(t)|\Psi_0\rangle$. Here, we consider $|\Psi_0\rangle = |M,P,0,0\rangle$. Defining $\Delta\epsilon_1^+ \equiv \epsilon_{q_1,q_2} - \epsilon_{q_1+1,q_2}$ and $\Delta\epsilon_1^- \equiv \epsilon_{q_1,q_2} - \epsilon_{q_1-1,q_2}$, we obtain:

$$
\begin{aligned}
\langle N_1 - N_3\rangle(t) &= \sum_{q_2=0}^{P}\left(\sum_{q_1=1}^{M} e^{-i\Delta\mathfrak{e}_1^- t}\sqrt{q_1(M-q_1+1)}\langle M,P,0,0|N,P,q_1-1,q_2\}\right.\\
&\left.+\sum_{q_1=0}^{M-1} e^{-i\Delta\mathfrak{e}_1^+ t}\sqrt{(M-q_1)(q_1+1)}\langle M,P,0,0|N,P,q_1+1,q_2\}\right)\{N,P,q_1,q_2|M,P,0,0\rangle.\\
&= \frac{M!P!}{2^N}\sum_{q_2=0}^{P}\frac{1}{q_2!(P-q_2)!\sqrt{q_1!(M-q_1)!}}\left(\sum_{q_1=1}^{M} e^{-i\Delta\mathfrak{e}_1^- t}\sqrt{\frac{q_1(M-q_1+1)}{(q_1-1)!(M-q_1+1)!}}\right.\\
&\qquad\left.+\sum_{q_1=0}^{M-1} e^{-i\Delta\mathfrak{e}_1^+ t}\sqrt{\frac{(M-q_1)(q_1+1)}{(q_1+1)!(M-q_1-1)!}}\right)\\
&= \frac{M!P!}{2^N}\sum_{q_2=0}^{P}\frac{1}{q_2!(P-q_2)!\sqrt{q_1!(M-q_1)!}}\left(\sum_{q_1=1}^{M} e^{-i\Delta\mathfrak{e}_1^- t}\sqrt{\frac{q_1}{(q_1-1)!(M-q_1)!}}\right.\\
&\qquad\left.+\sum_{q_1=0}^{M-1} e^{-i\Delta\mathfrak{e}_1^+ t}\sqrt{\frac{M-q_1}{q_1!(M-q_1-1)!}}\right)\\
&= \frac{M!P!}{2^N}\sum_{q_2=0}^{P}\frac{1}{q_2!(P-q_2)!}\left(\sum_{q_1=1}^{M}\frac{e^{-i\Delta\mathfrak{e}_1^- t}}{(q-1)!(M-q_1)!}+\sum_{q_1=0}^{M-1}\frac{e^{-i\Delta\mathfrak{e}_1^+ t}}{q_1!(M-q_1-1)!}\right)\\
&= \frac{M!P!}{2^N}\sum_{q_2=0}^{P}\frac{1}{q_2!(P-q_2)!}\sum_{q_1=1}^{M}\frac{1}{(q_1-1)!(M-q_1)!}\left(e^{-i\Delta\mathfrak{e}_1^- t}+e^{i\Delta\mathfrak{e}_1^- t}\right)\\
&= \frac{M!P!}{2^{N-1}}\sum_{q_2=0}^{P}\frac{1}{q_2!(P-q_2)!}\sum_{q_1=1}^{M}\frac{1}{(q_1-1)!(M-q_1)!}\cos(\Delta\mathfrak{e}_1^- t)
\end{aligned}
\tag{A.1.14}
$$

To continue the calculation, we must explicitly calculate $\Delta\mathfrak{e}_1^-$. By using the expression derived in (A.1.3), we get:

$$
\begin{aligned}
\Delta\mathfrak{e}_1^- &= \mathfrak{e}_{q_1,q_2}-\mathfrak{e}_{q_1-1,q_2}\\
&= \frac{J^2}{4U[(M-P)^2-1]}\left[(N+1)(q_1+q_2)-2q_1q_2-(N+1)(q_1+q_2-1)+2(q_1-1)q_2\right]\\
&= \frac{J^2}{4U[(M-P)^2-1]}\left[(N+1)-2q_2\right]=\Omega\left[(N+1)-2q_2\right],
\end{aligned}
\tag{A.1.15}
$$

where we defined $\Omega\equiv J^2/[4U(M-P)^2-1]$. Now, using it in (A.1.14), we arrive with:

$$
\begin{aligned}
\langle N_1 - N_3 \rangle (t) &= \frac{M!P!}{2^{N-1}} \sum_{q_2=0}^{P} \frac{\cos\left([N+1-2q_2]\,\Omega t\right)}{q_2!(P-q_2)!} \sum_{q_1=1}^{M} \frac{1}{(q_1-1)!(M-q_1)!} \\
&= \frac{P!}{2^{N-1}} \sum_{q_2=0}^{P} \frac{\cos\left([N+1-2q_2]\,\Omega t\right)}{q_2!(P-q_2)!} \sum_{q_1=0}^{M-1} \frac{M(M-1)!}{q_1![(M-1)-q_1]!} \\
&= M\frac{P!}{2^{P}} \sum_{q_2=0}^{P} \frac{\cos\left([N+1-2q_2]\,\Omega t\right)}{q_2!(P-q_2)!} \\
&= M\frac{P!}{2^{P+1}} \sum_{q_2=0}^{P} \frac{e^{i(N+1-2q_2)\Omega t} + e^{-i(N+1-2q_2)\Omega t}}{q_2!(P-q_2)!} \\
&= M\frac{1}{2^{P+1}} \left(e^{i(N+1)\Omega t} \sum_{q_2=0}^{P} \frac{P!}{q_2!(P-q_2)!} e^{-2i\Omega t q_2} + e^{-i(N+1)\Omega t} \sum_{q_2=0}^{P} \frac{P!}{q_2!(P-q_2)!} e^{2i\Omega t q_2} \right) \\
&= M\frac{1}{2^{P+1}} \left(e^{i(N+1)\Omega t} \left[1 + e^{-2i\Omega t}\right]^P + e^{-i(N+1)\Omega t} \left[1 + e^{2i\Omega t}\right]^P \right) \\
&= M\frac{1}{2^{P+1}} \left(e^{i(N+1)\Omega t} e^{-iP\Omega t} + e^{-i(N+1)\Omega t} e^{iP\Omega t} \right) 2^P (\cos\Omega t)^P \\
&= \frac{M}{2} (\cos\Omega t)^P \left(e^{i(M+1)\Omega t} + e^{-i(M+1)\Omega t} \right).
\end{aligned}
$$

Above, we used the relation $\sum_{j=0}^{m} \frac{m!}{j!(m-j)!} x^j = (1+x)^m$. Finally, by simplifying the last expression:

$$
\langle N_1 - N_3 \rangle (t) = M \cos[(M+1)\Omega t][\cos(\Omega t)]^P. \tag{A.1.16}
$$

Now, we can use the symmetry between $M \leftrightarrow P$ to find the analytical expressions of the quantum dynamics for the imbalance between 2-4, such that:

$$
\langle N_2 - N_4 \rangle (t) = P \cos[(P+1)\Omega t][\cos(\Omega t)]^M. \tag{A.1.17}
$$

It is possible to show that the same result is obtained if an initial state $|\Psi_0\rangle = |M,0,0,P\rangle$ is considered.

A.1.3.2 Initial NOON state

Now, let us suppose an initial NOON state $|\Psi_0\rangle = \overbrace{\frac{1}{\sqrt{2}}|M,P,0,0\rangle}^{|A\rangle} + \overbrace{\frac{e^{i\phi}}{\sqrt{2}}|M,0,0,P\rangle}^{|B\rangle}$. Defining $N_{ij}(t) \equiv (N_i - N_j)(t)$, we calculate $\langle N_1 - N_3 \rangle (t)$ as:

$$
\begin{aligned}
\langle N_1 - N_3 \rangle (t) &= (\langle A| + \langle B|) N_{13}(t) (|A\rangle + |B\rangle) \\
&= \langle A|N_{13}(t)|A\rangle + \langle A|N_{13}(t)|B\rangle + \langle B|N_{13}(t)|A\rangle + \langle B|N_{13}(t)|B\rangle,
\end{aligned}
$$

where we recognize

$$\langle A|N_{13}(t)|A\rangle + \langle B|N_{13}(t)|B\rangle = M\cos[(M+1)\Omega t][\cos(\Omega t)]^P.$$

Hence, we must calculate $\langle A|N_{13}(t)|B\rangle$ as follows:

$$\begin{aligned}\langle A|N_{13}(t)|B\rangle = \frac{e^{i\phi}}{2}\sum_{q_2=0}^{P}(-1)^{q_2}\Bigg(&\sum_{q_1=1}^{M} e^{-i\Delta\mathfrak{e}_1^- t}\sqrt{q_1(M-q_1+1)}\langle M,P,0,0|N,P,q_1-1,q_2\} \\ &+\sum_{q_1=0}^{M-1} e^{-i\Delta\mathfrak{e}_1^+ t}\sqrt{(M-q_1)(q_1+1)}\langle M,P,0,0|N,P,q_1+1,q_2\}\Bigg)\{N,P,q_1,q_2|M,0,0,P\rangle.\end{aligned}$$

Considering the relation $\{N,P,q_1,q_2|M,0,0,P\rangle = (-1)^{q_2}\{N,P,q_1,q_2|M,P,0,0\rangle$ and using some previous results, we can rewrite last expression as:

$$\begin{aligned}\langle A|N_{13}(t)|B\rangle &= \frac{M}{2^{P+1}}\frac{e^{i\phi}}{2}\left(e^{i(N+1)\Omega t}\sum_{q_2=0}^{P}\frac{(-1)^{q_2}P!}{q_2!(P-q_2)!}e^{-2i\Omega t q_2} + e^{-i(N+1)\Omega t}\sum_{q_2=0}^{P}\frac{(-1)^{q_2}P!}{q_2!(P-q_2)!}e^{2i\Omega t q_2}\right) \\ &= \frac{M}{2^{P+1}}\frac{e^{i\phi}}{2}\left(e^{i(N+1)\Omega t}\left[1-e^{-2i\Omega t}\right]^P + e^{-i(N+1)\Omega t}\left[1-e^{2i\Omega t}\right]^P\right) \\ &= \frac{M}{2^{P+1}}\frac{e^{i\phi}}{2}\left(e^{i(N+1)\Omega t}e^{-iP\Omega t}\left[i^P\right] + e^{-i(N+1)\Omega t}e^{iP\Omega t}\left[i^{-P}\right]\right)2^P(\sin\Omega t)^P \\ &= \frac{M}{2}\frac{e^{i\phi}}{2}[\sin(\Omega t)]^P\left(e^{i[(M+1)\Omega t+P\pi/2]} + e^{-i[(M+1)\Omega t+P\pi/2]}\right). \\ &= M\frac{e^{i\phi}}{2}[\sin(\Omega t)]^P\cos\left[(M+1)\Omega t+\frac{P\pi}{2}\right],\end{aligned}$$

where we used the property: $i^x = e^{i\pi x/2}$. Now, since $\langle B|N_{13}(t)|A\rangle = \langle A|N_{13}(t)|B\rangle^*$, we obtain:

$$\langle A|N_{13}(t)|B\rangle + \langle B|N_{13}(t)|A\rangle = M\cos(\phi)[\sin(\Omega t)]^P\cos\left[(M+1)\Omega t+\frac{P\pi}{2}\right].$$

Therefore, the expression for $\langle N_1 - N_3\rangle(t)$ becomes:

$$\begin{aligned}\langle N_1 - N_3\rangle(t) = &M\cos[(M+1)\Omega t][\cos(\Omega t)]^P \\ &+ M\cos(\phi)[\sin(\Omega t)]^P\cos\left[(M+1)\Omega t+\frac{P\pi}{2}\right].\end{aligned} \tag{A.1.18}$$

A similar development done for sites "2-4" results in $\langle N_2 - N_4\rangle(t) = 0$.

A.1.4 Variance

In order to calculate dynamical fluctuations, it is necessary to first evaluate $(N_1 - N_3)^2(t)$. Starting with the expression on (A.1.7) and expanding it:

$$(N_1 - N_3)^2 = N_{b_1} + N_{b_2} + 2N_{b_1}N_{b_2} + (b_1^\dagger)^2(b_2)^2 + (b_1)^2(b_2^\dagger)^2 \equiv N_{13}^2. \tag{A.1.19}$$

By acting this operator into $|M,P,q_1,q_2\}$, we obtain:

$$\begin{aligned} N_{13}^2|M,P,q_1,q_2\} = {} & [M + 2q_1(M-q_1)]|M,P,q_1,q_2\} \\ & + \sqrt{(q_1+1)(q_1+2)(M-q_1)(M-q_1-1)}|N,P,q_1+2,q_2\} \\ & + \sqrt{q_1(q_1-1)(M-q_1+1)(M-q_1+2)}|N,P,q_1-2,q_2\}. \end{aligned}$$

Therefore, we may evaluate $N_{13}^2(t)$ as:

$$\begin{aligned} N_{13}^2(t) = \sum_{q_1=0}^{M}\sum_{q_2=0}^{P}\Big(& e^{-i(\mathfrak{e}_{q_1,q_2}-\mathfrak{e}_{q_1-2,q_2})t}\sqrt{q_1(q_1-1)(M-q_1+1)(M-q_1+2)}|N,P,q_1-2,q_2\} \\ & + e^{-i(\mathfrak{e}_{q_1,q_2}-\mathfrak{e}_{q_1+2,q_2})t}\sqrt{(q_1+1)(q_1+2)(M-q_1)(M-q_1-1)}|N,P,q_1+2,q_2\} \\ & + [M + 2q_1(M-q_1)]|M,P,q_1,q_2\}\Big)\{N,P,q_1,q_2|. \end{aligned} \tag{A.1.20}$$

Considering an initial NOON state: $|\Psi_0\rangle = \overbrace{\frac{1}{\sqrt{2}}|M,P,0,0\rangle}^{|A\rangle} + \overbrace{\frac{e^{i\phi}}{\sqrt{2}}|M,0,0,P\rangle}^{|B\rangle}$, we can calculate $\langle(N_1 - N_3)^2(t)\rangle$, where:

$$\langle N_{13}^2(t)\rangle = \langle A|N_{13}^2(t)|A\rangle + \langle B|N_{13}^2(t)|B\rangle + 2\,\mathrm{Re}\left(\langle A|N_{13}^2(t)|B\rangle\right).$$

It is enough to calculate $\langle A|N_{13}^2(t)|A\rangle$ and $\langle A|N_{13}^2(t)|B\rangle$, since $\langle A|N_{13}^2(t)|A\rangle = \langle B|N_{13}^2(t)|B\rangle$. Explicitly, we get:

$$\begin{aligned} 2\langle A|N_{13}^2(t)|A\rangle = \sum_{q_2=0}^{P}\frac{M!P!}{2^N q_2!(P-q_2)!}\Bigg(& \sum_{q_1=2}^{M} e^{-i\Delta\mathfrak{e}_2^- t}\frac{1}{(q_1-2)!(M-q_1)!} \\ & + \sum_{q_1=0}^{M-2} e^{-i\Delta\mathfrak{e}_2^+ t}\frac{1}{q_1!(M-q_1-2)!} + \sum_{q_1=0}^{M}\frac{M}{q_1!(M-q_1)!} \\ & + 2\sum_{q_1=0}^{M}\frac{1}{(q_1-1)!(M-q_1-1)!}\Bigg). \end{aligned} \tag{A.1.21}$$

Expanding $\Delta\mathfrak{e}_2^- = 2\Omega[(N+1) - 2q_2] = -\Delta\mathfrak{e}_2^+$, substituting into equation (A.1.21) and simplifying it, we arrive with:

$$2\langle A|N_{13}^2(t)|A\rangle = \frac{M(M+1)}{2} + \frac{M(M-1)}{2}\left[\cos(2\Omega t)\right]^P \cos\left[2\Omega(M+1)t\right]. \tag{A.1.22}$$

The evaluation of $\langle A|N_{13}^2(t)|B\rangle$ yields the same expression as Eq. A.1.21, with the correction $e^{i\phi}(-1)^{q_2}$. Explicitely:

$$\begin{aligned} 2\langle A|N_{13}^2(t)|B\rangle = \sum_{q_2=0}^{P} \frac{M!P!(-1)^{q_2}e^{i\phi}}{2^N q_2!(P-q_2)!}\Bigg(\sum_{q_1=2}^{M} e^{-i\Delta\epsilon_2^- t}\frac{1}{(q_1-2)!(M-q_1)!} \\ + \sum_{q_1=0}^{M-2} e^{-i\Delta\epsilon_2^+ t}\frac{1}{q_1!(M-q_1-2)!} + \sum_{q_1=0}^{M}\frac{M}{q_1!(M-q_1)!} \\ + 2\sum_{q_1=0}^{M}\frac{1}{(q_1-1)!(M-q_1-1)!}\Bigg). \\ = \frac{M(M-1)}{2}e^{i\phi}\cos\left[2\Omega(M+1)t + \frac{P\pi}{2}\right]\left[\sin(2\Omega t)\right]^P. \end{aligned} \tag{A.1.23}$$

Therefore, the quadratic-imbalance quantum dynamics will be given by:

$$\begin{aligned} \langle N_{13}^2(t)\rangle = \frac{M(M+1)}{2} + \frac{M(M-1)}{2}\left[\cos(2\Omega t)\right]^P\cos\left[2\Omega(M+1)t\right] \\ + \frac{M(M-1)}{2}\cos\left[2\Omega(M+1)t + \frac{P\pi}{2}\right]\left[\sin(2\Omega t)\right]^P\cos\phi. \end{aligned} \tag{A.1.24}$$

A.2 INTERFEROMETRIC STATES

Here, the generation of interferometric states by the model - at the resonant regime, with N odd - will be analytically demonstrated.

A.2.1 Pure initial state

Considering $|\Psi_0\rangle = |M,P,0,0\rangle$, $M+P=N$ odd, we calculate the projection of $|\Psi(t)\rangle = e^{-iH_{eff}t}|\Psi_0\rangle$ on the four simplest states that satisfy the resonant tunneling regime: $|\Psi_a\rangle \equiv |M,P,0,0\rangle\,(=|\Psi_0\rangle)$, $|\Psi_b\rangle \equiv |M,0,0,P\rangle$, $|\Psi_c\rangle \equiv |0,P,M,0\rangle$ and $|\Psi_d\rangle \equiv |0,0,M,P\rangle$. The full evaluation will be shown for $\langle\Psi_b|\Psi(t)\rangle$ as follows.

$$\begin{aligned}
\langle\Psi_b|\Psi(t)\rangle &= \sum_{q_1,p_1=0}^{M}\sum_{q_2,p_2=0}^{P}\langle M,0,0,P|M,P,q_1,q_2\}\{M,P,q_1,q_2|e^{-iH_{eff}t}|M,P,p_1,p_2\}, \\
&\qquad\qquad \times\{M,P,p_1,p_2|M,P,0,0\rangle. \\
&= \frac{1}{2^N}\sum_{q_1=0}^{M}\sum_{q_2=0}^{P}(-1)^{q_2}e^{-i\mathfrak{e}_{q_1,q_2}t}\frac{M!P!}{q_1!(M-q_1)!q_2!(P-q_2)!} \\
&= \frac{1}{2^N}\sum_{q_1=0}^{M}\frac{M!}{q_1!(M-q_1)!}e^{-i\Omega(N+1)q_1t}\sum_{q_2=0}^{P}\frac{P!}{q_2!(P-q_2)!}\left[e^{-it[\Omega(N+1)-2\Omega q_1]}\right]^{q_2}(-1)^{q_2} \\
&= \frac{1}{2^M}e^{-i\frac{P}{2}[\Omega(N+1)t+\pi]}\sum_{q_1=0}^{M}\frac{M!}{q_1!(M-q_1)!}\{e^{-i\Omega(M+1)t}\}^{q_1}\left[\sin\left[\frac{\Omega t}{2}(2q_1-N-1)\right]\right]^{P}.
\end{aligned} \tag{A.2.1}$$

where the closure condition $\mathbb{1} = \sum_{q_1=0}^{M}\sum_{q_2=0}^{P}|M,P,q_1,q_2\}\{M,P,q_1,q_2|$ was employed. At time $t=t_m=\pi/(2\Omega)$, the projection becomes:

$$\langle\Psi_b|\Psi(t_m)\rangle = \frac{1}{2^M}e^{-i\frac{P\pi}{2}\left[\frac{N+1}{2}+1\right]}\sum_{q_1=0}^{M}\frac{M!}{q_1!(M-q_1)!}\{e^{-i(M+1)\pi/2}\}^{q_1}\left[\sin\left(\frac{\pi}{2}\left(q_1-\frac{N+1}{2}\right)\right)\right]^{P} \tag{A.2.2}$$

Remarkably, it is possible to demonstrate that the expression above does not depend on M, P or N (although it must be odd). Rather, by considering different values for M and N and numerically evaluating it, one arrives always at:

$$\langle\Psi_b|\Psi(t_m)\rangle = \frac{1}{2}. \tag{A.2.3}$$

Following a similar procedure for the other three projections, it is possible to show that:

$$\langle\Psi_a|\Psi(t_m)\rangle = \frac{\beta}{2} \qquad \langle\Psi_c|\Psi(t_m)\rangle = \frac{1}{2} \qquad \langle\Psi_d|\Psi(t_m)\rangle = -\frac{\beta}{2}. \tag{A.2.4}$$

From Eqs. A.2.3 and A.2.4, one infers that the state at $t=t_m$, for $|\Psi_0\rangle = |M,P,0,0\rangle$ and $N=M+P$ odd, is given by:

$$|\Psi(t_m)\rangle = \frac{1}{2}\left[\beta|M,P,0,0\rangle + |M,0,0,P\rangle + |0,P,M,0\rangle - \beta|0,0,M,P\rangle\right]. \tag{A.2.5}$$

A.2.2 Initial NOON state

We now repeat the same analysis as before, but with an initial state $|\Psi_0\rangle = \frac{1}{\sqrt{2}}|M,P,0,0\rangle + \frac{e^{i\phi}}{\sqrt{2}}|M,0,0,P\rangle$. A simplification can be made by recognizing that

$$|\Psi(t)\rangle = e^{-iH_{eff}t}|\Psi_0\rangle = \frac{1}{\sqrt{2}}\underbrace{e^{-iH_{eff}t}|M,P,0,0\rangle}_{|A(t)\rangle} + \frac{e^{i\phi}}{\sqrt{2}}\underbrace{e^{-iH_{eff}t}|M,0,0,P\rangle}_{|B\rangle(t)},$$

where $|A(t_m)\rangle$ is the same state of Eq. A.2.5. Now, the idea is to do the equivalent of what was done to calculate $|A\rangle$. Explicitly expanding $\langle\Psi_b|B(t)\rangle$ in terms of the eigenbasis of H_{eff}:

$$\begin{aligned}
\langle\Psi_b|B(t)\rangle &= \frac{1}{\sqrt{2}}\sum_{q_1,p_1=0}^{M}\sum_{q_2,p_2=0}^{P}\langle M,P,0,0|\,M,P,q_1,q_2\}\{M,P,q_1,q_2|e^{-iH_{eff}t}|M,P,p_1,p_2\} \\
&\qquad\qquad \times\{M,P,p_1,p_2|M,0,0,P\rangle. \\
&= \frac{1}{2^N\sqrt{2}}\sum_{q_1=0}^{M}\sum_{q_2=0}^{P}e^{-\mathfrak{e}_{q_1,q_2}t}\frac{M!P!}{q_1!(M-q_1)!q_2!(P-q_2)!} \\
&= \frac{1}{2^N\sqrt{2}}\sum_{q_1=0}^{M}\frac{M!}{q_1!(M-q_1)!}e^{-\Omega(N+1)q_1t}\sum_{q_2=0}^{P}\frac{P!}{q_2!(P-q_2)!}\left[e^{-it[\Omega(N+1)-2\Omega q_1]}\right]^{q_2} \\
&= \frac{1}{2^M\sqrt{2}}e^{-i\Omega\left(\frac{N+1}{2}\right)Pt}\sum_{q_1=0}^{M}\frac{M!}{q_1!(M-q_1)!}\left[e^{-i\Omega(M+1)t}\right]^{q_1}\left[\cos\left[\Omega\left(q_1-\frac{N+1}{2}\right)t\right]\right]^{P}.
\end{aligned} \tag{A.2.6}$$

Once again, we are interested in the expression above for $t = t_m$, which results in:

$$\langle\Psi_b|B(t_m)\rangle = \frac{1}{2^M\sqrt{2}}e^{-i\left(\frac{N+1}{4}\right)P\pi}\sum_{q_1=0}^{M}\frac{M!}{q_1!(M-q_1)!}\left[e^{-i\left(\frac{M+1}{2}\right)\pi}\right]^{q_1}\left[\cos\left(\frac{\pi}{2}\left(q_1-\frac{N+1}{2}\right)\right)\right]^{P}. \tag{A.2.7}$$

By considering different values for M and N and evaluating it, one obtains:

$$\langle\Psi_b|B(t_m)\rangle = \frac{\beta e^{i\phi}}{2}.$$

Repeating the procedure for the other projections, we get:

$$\langle\Psi_a|B(t_m)\rangle = \frac{e^{i\phi}}{2} \qquad \langle\Psi_c|B(t_m)\rangle = -\frac{\beta e^{i\phi}}{2} \qquad \langle\Psi_d|B(t_m)\rangle = \frac{e^{i\phi}}{2},$$

which yields

$$|\Psi(t_m)\rangle = \frac{1+\beta e^{i\phi}}{2\sqrt{2}}\left[\beta|M,P,0,0\rangle + |M,0,0,P\rangle\right] + \frac{1-\beta e^{i\phi}}{2\sqrt{2}}\left[|0,P,M,0\rangle - \beta|0,0,M,P\rangle\right]. \tag{A.2.8}$$

A.2.3 Phase-encoding

Here, a very simple proof of the phase-encoding operator $e^{-i\mu(N_2-N_4)t_\mu}$ introduced in the main text is presented. Considering the action of the above operator on the u-NOON state:

$$
\begin{aligned}
& e^{-i\mu(N_2-N_4)t_\mu}\ \frac{1}{2}\left[\beta\,|M,P,0,0\rangle + |M,0,0,P\rangle + |0,P,M,0\rangle - \beta\,|0,0,M,P\rangle\right] \\
&= \frac{1}{2}\left[\beta e^{-iP\mu t_\mu}\,|M,P,0,0\rangle + e^{iP\mu t_\mu}\,|M,0,0,P\rangle + e^{-iP\mu t_\mu}\,|0,P,M,0\rangle - \beta e^{iP\mu t_\mu}\,|0,0,M,P\rangle\right] \\
&= \frac{e^{-iP\mu t_\mu}}{2}\left[\beta\,|M,P,0,0\rangle + e^{2iP\mu t_\mu}\,|M,0,0,P\rangle + |0,P,M,0\rangle - \beta e^{2iP\mu t_\mu}\,|0,0,M,P\rangle\right] \\
&= \frac{e^{-iP\theta/2}}{2}\left[\beta\,|M,P,0,0\rangle + e^{iP\theta}\,|M,0,0,P\rangle + |0,P,M,0\rangle - \beta e^{iP\theta}\,|0,0,M,P\rangle\right],
\end{aligned}
\tag{A.2.9}
$$

where we defined $\theta \equiv 2\mu t_\mu$. The same simple procedure can be employed in any other quantum state discussed in the main text.

A.3 Von-Neumann Entropy

Here, we demonstrate the main results regarding the Von-Neumann entropy used in Chapter 4. In doing so, we will always consider the effective Hamiltonian H_{eff}.

Starting from an initial state $|\Psi_0\rangle = \frac{1}{\sqrt{2}}\left(|M,P,0,0\rangle + e^{i\phi}|M,0,0,P\rangle\right)$, we calculate its time evolution as:

$$\begin{aligned}
|\Psi(t)\rangle &= e^{-iH_{eff}t}|\Psi_0\rangle \\
&= \frac{e^{-iH_{eff}t}}{\sqrt{2}}\left(|M,P,0,0\rangle + e^{i\phi}|M,0,0,P\rangle\right) \\
&= \frac{1}{\sqrt{2}}\Bigg(\underbrace{\sum_{q_1,q_2} e^{-i\epsilon_{q_1,q_2}t}\sqrt{\frac{C^M_{q_1}C^P_{q_2}}{2^N}}|M,P,q_1,q_2\}}_{|A(t)\rangle} + e^{i\phi}\underbrace{\sum_{q_1,q_2} e^{-i\epsilon_{q_1,q_2}t}(-1)^{q_2}\sqrt{\frac{C^M_{q_1}C^P_{q_2}}{2^N}}|M,P,q_1,q_2\}}_{|B(t)\rangle}\Bigg),
\end{aligned}$$

where we employed the results from Eqs. A.1.11 and A.1.12. Then, the density operator $\rho(t)$ will read:

$$\begin{aligned}
\rho(t) &= |\Psi(t)\rangle\langle\Psi(t)| \\
&= \frac{1}{2}\left(|A(t)\rangle\langle A(t)| + |B(t)\rangle\langle B(t)| + e^{-i\phi}|A(t)\rangle\langle B(t)| + e^{i\phi}|B(t)\rangle\langle A(t)|\right).
\end{aligned} \tag{A.3.1}$$

A.3.1 Entanglement between classes

In order to calculate $S(\rho_A(t))$, we first need to obtain the reduced operator $\rho_A(t) = \mathrm{tr}_B\ \rho(t)$. Explicitly for $|A(t)\rangle\langle A(t)|$:

$$\mathrm{tr}_B\ |A(t)\rangle\langle A(t)| = \sum_{m,n=0}^{N}\langle m,n|A(t)\rangle\langle A(t)|m,n\rangle, \tag{A.3.2}$$

where $|m,n\rangle$ act on wells "2" and "4". The inner product on the previous equation is not trivially calculated, since it must result on a "ket-bra" with half the degrees of freedom. To carefully evaluate it, it is convenient to first write $|M,P,q_1,q_2\} = |\chi(q_1)\rangle \otimes |\zeta(q_2)\rangle$, where:

$$
\begin{aligned}
|\chi(q_1)\rangle &\equiv \frac{C_{q_1}^M}{\sqrt{M!}}\left(\frac{a_1^\dagger + a_3^\dagger}{\sqrt{2}}\right)^{M-q_1}\left(\frac{a_1^\dagger - a_3^\dagger}{\sqrt{2}}\right)^{q_1}|0\rangle_A \\
|\zeta(q_2)\rangle &\equiv \frac{C_{q_2}^P}{\sqrt{P!}}\left(\frac{a_2^\dagger + a_4^\dagger}{\sqrt{2}}\right)^{P-q_2}\left(\frac{a_2^\dagger - a_4^\dagger}{\sqrt{2}}\right)^{q_2}|0\rangle_B \\
&= \sum_{k=0}^{P-q_2}\sum_{l=0}^{q_2} C_k^{P-q_2} C_l^{q_2}\sqrt{\frac{(P-k-l)!(k+l)!}{2^P(P-q_2)!q_2!}}(-1)^l\,|P-k-l,k+l\rangle \\
&= \sum_{r=0}^{P}\sum_{k=0}^{r} C_k^{P-q_2} C_{r-k}^{q_2}\sqrt{\frac{(P-r)!r!}{2^P(P-q_2)!q_2!}}(-1)^{r-k}\,|P-r,r\rangle \\
&= \sum_{r=0}^{P} a_r(q_2,P)\,|P-r,r\rangle\,.
\end{aligned}
\tag{A.3.3}
$$

In the equation above, we used $\sum_{k=0}^{P-q_2}\sum_{l=0}^{q_2} \to \sum_{r=0}^{P}\sum_{k=0}^{r}$. The term $a_r(q,P)$ employed is defined as:

$$
a_r(q,P) \equiv \frac{1}{\sqrt{2^P}}\sum_{k=0}^{r}\sqrt{\frac{C_q^P}{C_r^P}}C_k^{P-q}C_{r-k}^{q}(-1)^{r-k}.
$$

Now, we continue the evaluation of Eq. A.3.2:

$$
\begin{aligned}
\mathrm{tr}_B\ |A(t)\rangle\langle A(t)| &= \sum_{m,n=0}^{N}\langle m,n|A(t)\rangle\langle A(t)|m,n\rangle \\
&= \frac{1}{2^N}\sum_{m,n}\sum_{q_1,q_2}\sum_{p_1,p_2} e^{-i(\mathfrak{e}_{q_1,q_2}-\mathfrak{e}_{p_1,p_2})t}\sqrt{C_{q_1}^M C_{q_2}^P C_{p_1}^M C_{p_2}^P}\langle m,n|M,P,q_1,q_2\}\{M,P,p_1,p_2|m,n\rangle \\
&= \frac{1}{2^N}\sum_{m,n}\sum_{q_1,q_2}\sum_{p_1,p_2}\sum_{r_1,r_2} e^{-i(\mathfrak{e}_{q_1,q_2}-\mathfrak{e}_{p_1,p_2})t}a_{r_1}(q_2,P)a_{r_2}(p_2,P)\sqrt{C_{q_1}^M C_{p_1}^M C_{q_2}^P C_{p_2}^P} \\
&\qquad\qquad \langle m,n|P-r_1,r_1\rangle\langle P-r_2,r_2|m,n\rangle\,|\chi(q_1)\rangle\langle\chi(p_1)| \\
&= \frac{1}{2^N}\sum_{q_1,q_2}\sum_{p_1,p_2}\sum_{r_1,r_2} e^{-i(\mathfrak{e}_{q_1,q_2}-\mathfrak{e}_{p_1,p_2})t}a_{r_1}(q_2,P)a_{r_2}(p_2,P)\sqrt{C_{q_1}^M C_{p_1}^M C_{q_2}^P C_{p_2}^P} \\
&\qquad\qquad \langle P-r_2,r_2|\underbrace{\sum_{m,n}|m,n\rangle\langle m,n|}_{\mathbb{1}_B}|P-r_1,r_1\rangle\,|\chi(q_1)\rangle\langle\chi(p_1)| \\
&= \frac{1}{2^N}\sum_{q_1,q_2}\sum_{p_1,p_2} e^{-i(\mathfrak{e}_{q_1,q_2}-\mathfrak{e}_{p_1,p_2})t}\sqrt{C_{q_1}^M C_{p_1}^M C_{q_2}^P C_{p_2}^P}\,|\chi(q_1)\rangle\langle\chi(p_1)|\sum_{r=0}^{P}a_r(q_2,P)a_r(p_2,P).
\end{aligned}
\tag{A.3.4}
$$

Since $\langle\zeta(q_2)|\zeta(p_2)\rangle = \delta_{q_2,p_2}$, it implies that $\sum_{r=0}^{P}a_r(q_2,P)a_r(p_2,P) = \delta_{q_2,p_2}$. By expanding $\mathfrak{e}_{q_1,q_2} - \mathfrak{e}_{p_1,q_2} = \Omega\,[(N+1)(q_1-p_1) - 2q_2(q_1-p_1)]$, we can rewrite the expression above as:

$$\begin{aligned}\mathrm{tr}_B\ |A(t)\rangle\langle A(t)| &= \frac{1}{2^N}\sum_{q_2}\sum_{q_1,p_1} e^{-2i\Omega t([N]_+(q_1-p_1)-q_2(q_1-p_1))} C_{q_2}^P \sqrt{C_{q_1}^M C_{p_1}^M}\,|\chi(q_1)\rangle\langle\chi(p_1)| \\ &= \frac{1}{2^N}\sum_{q_1,p_1} e^{-2i\Omega t[N]_+(q_1-p_1)}\sqrt{C_{q_1}^M C_{p_1}^M}\,|\chi(q_1)\rangle\langle\chi(p_1)|\sum_{q_2} C_{q_2}^P\left(e^{2i\Omega(q_1-p_1)t}\right)^{q_2} \\ &= \frac{1}{2^N}\sum_{q_1,p_1} e^{-2i\Omega t[N]_+(q_1-p_1)}\sqrt{C_{q_1}^M C_{p_1}^M}\left[1+e^{2i\Omega t(q_1-p_1)}\right]^P |\chi(q_1)\rangle\langle\chi(p_1)|\end{aligned} \tag{A.3.5}$$

At $t = t_m = \pi/(2\Omega)$, the above expression becomes:

$$\begin{aligned}\mathrm{tr}_B\ |A(t_m)\rangle\langle A(t_m)| &= \frac{1}{2^N}\sum_{q_1,p_1} e^{-i\pi[N]_+(q_1-p_1)}\sqrt{C_{q_1}^M C_{p_1}^M}\left[1+(-1)^{q_1-p_1}\right]^P |\chi(q_1)\rangle\langle\chi(p_1)|. \\ &= \frac{1}{2^M}\sum_{q_1,p_1} e^{-i\pi[N]_+(q_1-p_1)}\sqrt{C_{q_1}^M C_{p_1}^M}\,|\chi(q_1)\rangle\langle\chi(p_1)|, \text{ if } q_1-p_1 \text{ is even} \\ &\qquad 0, \text{ if } q_1-p_1 \text{ is odd.}\end{aligned} \tag{A.3.6}$$

Therefore, we can define the orthogonal states:

$$|\Psi_\pm\rangle = \frac{1}{\sqrt{2^M}}\sum_{q=0}^{M} e^{-iq\pi[N]_\pm}\sqrt{C_q^M}\,|\chi(q)\rangle, \tag{A.3.7}$$

such that we may rewrite Eq. A.3.6 as:

$$\mathrm{tr}_B\ |A(t_m)\rangle\langle A(t_m)| = \frac{1}{2}|\Psi_+\rangle\langle\Psi_+| + \frac{1}{2}|\Psi_-\rangle\langle\Psi_-|. \tag{A.3.8}$$

It is worth noticing here that, had we considered a simple initial state given by $|M,P,0,0\rangle$, then its time evolution would be $|A(t)\rangle$ and the expression above would be already $\rho_A(t_m)$. The calculation of $\mathrm{tr}_B\ |B(t)\rangle\langle B(t)|$ can be performed in a similar way. Its equivalent of Eq. A.3.5 will be the exact same expression with a term $(-1)^{q_2+p_2}$. Then, since $\sum_{r=0}^{P} a_r(q_2,P)a_r(p_2,P) = \delta_{q_2,p_2}$, $(-1)^{q_2+p_2} = 1$, and the final result of $\mathrm{tr}_B\ |B(t_m)\rangle\langle B(t_m)|$ will be exactly the same as the one for $\mathrm{tr}_B\ |A(t_m)\rangle\langle A(t_m)|$. Therefore, the partial trace for the first two terms of Eq. A.3.1 can be written as:

$$\begin{aligned}\mathrm{tr}_B\,\frac{1}{2}\left(|A(t_m)\rangle\langle A(t_m)| + |B(t_m)\rangle\langle B(t_m)|\right) &= \frac{1}{2}\mathrm{tr}_B\ |A(t_m)\rangle\langle A(t_m)| + \frac{1}{2}\mathrm{tr}_B\ |B(t_m)\rangle\langle B(t_m)| \\ &= \frac{1}{2}|\Psi_+\rangle\langle\Psi_+| + \frac{1}{2}|\Psi_-\rangle\langle\Psi_-|.\end{aligned} \tag{A.3.9}$$

When analyzing the individual expressions for $|A(t)\rangle$ and $|B(t)\rangle$, one notices that the only difference relies on the term $(-1)^{q_2}$, which is present only on $|B(t)\rangle$. Therefore, we realize that $|A(t)\rangle\langle B(t)| = |B(t)\rangle\langle A(t)|$, and $\mathrm{tr}_B\ |A(t)\rangle\langle B(t)|$ can be written as an adaptation of Eq. A.3.5:

$$\begin{aligned}\mathrm{tr}_B\ |A(t)\rangle\langle B(t)| &= \frac{1}{2^N}\sum_{q_2}\sum_{q_1,p_1} e^{-2i\Omega t([N]_+(q_1-p_1)-q_2(q_1-p_1))} C_{q_2}^P \sqrt{C_{q_1}^M C_{p_1}^M}(-1)^{q_2}\,|\chi(q_1)\rangle\langle\chi(p_1)| \\ &= \frac{1}{2^N}\sum_{q_1,p_1} e^{-2i\Omega t[N]_+(q_1-p_1)}\sqrt{C_{q_1}^M C_{p_1}^M}\,|\chi(q_1)\rangle\langle\chi(p_1)|\sum_{q_2}\left(-e^{2i\Omega(q_1-p_1)t}\right)^{q_2} \\ &= \frac{1}{2^N}\sum_{q_1,p_1} e^{-2i\Omega t[N]_+(q_1-p_1)}\sqrt{C_{q_1}^M C_{p_1}^M}\left[1-e^{2i\Omega t(q_1-p_1)}\right]^P |\chi(q_1)\rangle\langle\chi(p_1)|\,.\end{aligned} \tag{A.3.10}$$

Once again, we are interested in the reduced density operator at $t = t_m = \pi/(2\Omega)$, which then becomes:

$$\begin{aligned}\mathrm{tr}_B\ |A(t_m)\rangle\langle B(t_m)| &= \frac{1}{2^N}\sum_{q_1,p_1} e^{-i\pi[N]_+(q_1-p_1)}\sqrt{C_{q_1}^M C_{p_1}^M}\left[1-(-1)^{q_1-p_1}\right]^P |\chi(q_1)\rangle\langle\chi(p_1)|\,. \\ &= \frac{1}{2^M}\sum_{q_1,p_1} e^{-i\pi[N]_+(q_1-p_1)}\sqrt{C_{q_1}^M C_{p_1}^M}\,|\chi(q_1)\rangle\langle\chi(p_1)|\,,\ \text{if } q_1-p_1 \text{ is odd} \\ &\qquad\qquad 0,\ \text{if } q_1-p_1 \text{ is even.}\end{aligned} \tag{A.3.11}$$

It is possible to rewrite the previous equation in terms of the basis $|\Psi_\pm\rangle$ such that it vanishes when $(q-p)$ is even. This is somehow the opposite behavior when comparing to $\mathrm{tr}_B\ |A(t)\rangle\langle A(t)|$, and leads to:

$$\mathrm{tr}_B\ |A(t)\rangle\langle B(t)| = \frac{1}{2}|\Psi_+\rangle\langle\Psi_+| - \frac{1}{2}|\Psi_-\rangle\langle\Psi_-|\,. \tag{A.3.12}$$

Finally, we can rewrite Eq. A.3.1 for $t = t_m$ as:

$$\rho_A(t_m) = \mathrm{tr}_B\,\rho(t_m) = \cos^2\frac{\phi}{2}|\Psi_+\rangle\langle\Psi_+| + \sin^2\frac{\phi}{2}|\Psi_-\rangle\langle\Psi_-|\,, \tag{A.3.13}$$

and, therefore, the Von-Neumann Entropy $S(\rho_B(t_m))$ will be given by:

$$S(\rho_B(t_m)) = -\cos^2\frac{\phi}{2}\log_2\left(\cos^2\frac{\phi}{2}\right) - \sin^2\frac{\phi}{2}\log_2\left(\sin^2\frac{\phi}{2}\right). \tag{A.3.14}$$

A.3.2 Entanglement between one site and the others

Here, we will demonstrate how to calculate $S(\rho_3(t_m))$. A similar procedure can be employed for evaluating the entanglement entropies for the other sites. Since the reduced density operator $\rho_3(t)$ corresponds to only one the model's degrees of freedom, it can be written as the mixed state:

$$\rho_3(t) = \sum_i \mathcal{P}_t(N_3 = i)\,|i\rangle\langle i|\,, \tag{A.3.15}$$

where $\mathcal{P}_t(N_3 = i)$ stands for the probability of measuring "i" particles at site 3, on a given time t. With this, the Von-Neumann entropy is simply given by:

$$S(\rho_3(t)) = -\sum_i \mathcal{P}_t(N_3 = i)\log_2\left[\mathcal{P}_t(N_3 = i)\right]. \tag{A.3.16}$$

We may now employ the previous results for $\rho_A(t)$ in order to evaluate the measurement probabilities as $\mathcal{P}_t(N_3 = i) = \langle M-i,i|\rho_A(t)|M-i,i\rangle$. Explicitly for $t = t_m$:

$$\mathcal{P}_{t_m}(N_3 = i) = \cos^2\frac{\phi}{2}|\langle M-i,i|\Psi_+\rangle|^2 + \sin^2\frac{\phi}{2}|\langle M-i,i|\Psi_-\rangle|^2. \tag{A.3.17}$$

We can calculate the inner products as:

$$\begin{aligned}
\langle M-i,i|\Psi_\pm\rangle &= \frac{1}{\sqrt{2^M}}\sum_{q=0}^{M} e^{-iq\pi[N]_\pm}\sqrt{C_q^M}\langle M-i,i|\chi(q)\rangle \\
&= \frac{1}{\sqrt{2^M}}\sum_{q=0}^{M}\sqrt{C_q^M}e^{-iq\pi[N]_\pm}\left(\sum_{r=0}^{M} a_r(q,M)\delta_{i,r}\right) \\
&= \frac{1}{\sqrt{2^M}}\sum_{q=0}^{M}\sqrt{C_q^M}a_q(i,M)e^{-iq\pi[N]_\pm} \\
&= \sum_{q=0}^{M}\sum_{k=0}^{q}\frac{\sqrt{C_i^M}}{2^M}C_k^{M-i}C_{q-k}^{M}(-1)^{q-k}e^{-iq\pi[N]_\pm} \\
&= \frac{\sqrt{C_i^M}}{2^M}\sum_{k=0}^{M-i}\sum_{r=0}^{i} C_k^{M-i}C_r^M(-1)^r e^{-ir\pi[N]_\pm}e^{-is\pi[N]_\pm} \\
&= \frac{\sqrt{C_i^M}}{2^M}\left(\sum_{k=0}^{M-i} C_k^{M-i}e^{-ik\pi[N]_\pm}\right)\left(\sum_{r=0}^{i} C_r^M(-1)^r e^{-ir\pi[N]_\pm}\right) \\
&= \frac{\sqrt{C_i^M}}{2^M}\left(1+e^{-i\pi[N]_\pm}\right)^{M-i}\left(1-e^{-i\pi[N]_\pm}\right)^{i}.
\end{aligned}$$

Therefore, we have:

$$\begin{aligned}
|\langle M-i|\Psi_\pm\rangle|^2 &= \frac{C_i^M}{2^{2M}}2^M(1+\cos(\pi[N]_\pm))^{M-i}(1-\cos(\pi[N]_\pm))^i \\
&= C_i^M\left(\cos^2\frac{\pi[N]_\pm}{2}\right)^{M-i}\left(\sin^2\frac{\pi[N]_\pm}{2}\right)^{i} \\
&= b_{M,i}\left(\sin^2\frac{\pi[N]_\pm}{2}\right),
\end{aligned} \tag{A.3.18}$$

where we introduced the Bernstein polynomials $b_{\nu,j}(z) = C_\nu^j\, z^\nu(1-z)^{j-\nu}$. With this, we may write the probability $\mathcal{P}_{t_m}(N_3 = i)$ as:

$$\begin{aligned}
\mathcal{P}_{t_m}(N_3 = i) &= \frac{1}{2}b_{M,i}\left(\sin^2\frac{\pi(N+1)}{4}\right) + \frac{1}{2}b_{M,i}\left(\sin^2\frac{\pi(N-1)}{4}\right) \\
&= \frac{1}{2}\delta_{i,0} + \frac{1}{2}\delta_{i,M}, \text{ if } N \text{ is odd;} \\
&= \qquad \frac{1}{2^M}C_i^M, \text{ if } N \text{ is even.}
\end{aligned} \tag{A.3.19}$$

By looking at Eqs. A.3.16 and A.3.19, it is clear that, differently than what happened for $S(\rho_A(t_m))$, the behavior of the Von-Neumann entropy for $\rho_3(t_m)$ is different in the scenarios of N odd and even. These are given by:

$$\begin{aligned} S(\rho_3(t_m)) &= 1, && \text{for } N \text{ odd;} \\ &= M - \sum_i C_i^M \log_2(C_i^M), && \text{for } N \text{ even.} \end{aligned} \tag{A.3.20}$$

Appendix B

Submitted papers

B.0.1 Integrable atomtronic interferometry

Daniel S. Grün, Leandro H. Ymai, Karin Wittmann W., Arlei P. Tonel, Angela Foerster & Jon Links

arXiv:2004.11987

Integrable atomtronic interferometry

D.S. Grun[1], L.H. Ymai[2], K Wittmann W.[1], A.P. Tonel[2], A. Foerster[1], J. Links[3]
[1] *Instituto de Fsica da UFRGS, Avenida Bento Gonalves 9500, Porto Alegre, Rio Grande do Sul, Brazil,*
[2] *Universidade Federal do Pampa, Av. Maria Anunciao Gomes de Godoy 1650, Bag, Rio Grande do Sul, Brazil, and*
[3] *School of Mathematics and Physics, The University of Queensland, Brisbane, Queensland, Australia.*
(Dated: February 16, 2021)

High sensitivity quantum interferometry requires more than just access to entangled states. It is achieved through deep understanding of quantum correlations in a system. Integrable models offer the framework to develop this understanding. We communicate the design of interferometric protocols for an integrable model that describes the interaction of bosons in a four-site configuration. Analytic formulae for the quantum dynamics of certain observables are computed. These expose the system's functionality as both an interferometric identifier, and producer, of NOON states. Being equivalent to a controlled-phase gate acting on two hybrid qudits, this system also highlights an equivalence between Heisenberg-limited interferometry and quantum information. These results are expected to open new avenues for integrability-enhanced atomtronic technologies.

Introduction.– Recent developments in the manipulation of wave-like properties in matter are driving a raft of atom-interferometric applications, in the vicinity of the Heisenberg limit, within the field of quantum metrology [1, 2]. It has long been recognized that the ability to effectively and efficiently harness quantum interference is equivalent to implementing certain tasks in quantum computation [3]. Nowadays, ultracold quantum gases are proving to be successful in enabling quantum simulations, for phenomena such as quantum magnetism and topological states of matter, beyond the capabilities of classical supercomputers [4]. Through a confluence of these types of investigations, there are several efforts to push research towards designs for atomtronic devices [5–7], based on circuits with atomic currents. These devices promise high levels of control in the manipulation of many-body systems, leading to advanced sensitivity in metrology [8] and other quantum technologies [9–13].

Around a decade ago [14] a class of models was identified for physical realization of an interferometer, using dipolar atoms. The Hamiltonian governing the time evolution of the system is a generalized Bose-Hubbard model on four sites, with closed boundary conditions and long-ranged interactions. We begin by pinpointing a set of *integrable* couplings for the Hamiltonian. That is, choices of parameters for which there are four conserved operators, equal to the number of degrees of freedom. The property of integrability has two significant impacts: (i) integrable systems have unique properties, such as Poisson distribution in energy level statistics [15], absence of chaotic behaviors [16], and non-standard thermal equilibration [17]. The quantum Newton cradle [18] provided experimental verification of the latter; (ii) mathematically, integrability facilitates tractable, closed-form formulae to describe the physics.

In our study we utilize the conserved operators of the integrable system to guide the design of measurement protocols for interferometric tasks (see Fig. 1). Our results are applicable in a particular regime, designated as *resonant tunneling*, whereby the energy levels separate into distinct bands. Through an effective Hamiltonian approach, the entire energy spectrum and structure of eigenstates becomes explicit for resonant tunneling. Moreover, the behavior system is clear in quantum information theoretic terms. The interferometer is equivalent to a system of two *hybrid qudits* [19], and the time-evolution of states is equivalent to the operation of a *controlled-phase* gate [20, 21]. We describe proof of principle examples of high-fidelity measurement protocols to identify and produce certain NOON states [1, 3, 22–24].

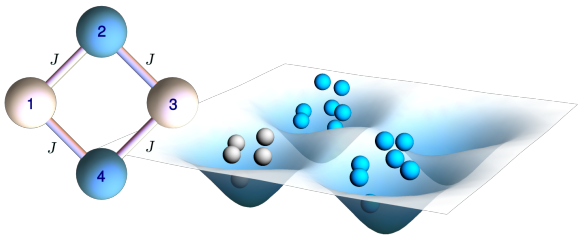

FIG. 1. Schematic representation of the interferometric circuit with tunneling between nearest neighbors. An initial state is prepared with M particles in site 1, and P particles in a (generally entangled) state across sites 2 and 4. After Hamiltonian time-evolution, measurement of particle number at site 3 is used to deduce information about the initial, or post-measurement, state across sites 2 and 4.

The model.– An extended Bose-Hubbard Hamiltonian on a square plaquette has the form [25, 26]

$$H = \frac{U_0}{2}\sum_{i=1}^{4} N_i(N_i-1) + \sum_{i=1}^{4}\sum_{j=1,j\neq i}^{4}\frac{U_{ij}}{2}N_iN_j - \frac{J}{2}[(a_1^\dagger + a_3^\dagger)(a_2+a_4) + (a_2^\dagger + a_4^\dagger)(a_1+a_3)]. \quad (1)$$

where $\{a_j, a_j^\dagger : j = 1,2,3,4\}$ are canonical boson annihilation and creation operators, U_0 characterizes the short-range interactions between bosons at the same site, $U_{ij} = U_{ji}$ accounts for long-range (e.g. dipole-dipole) interactions between sites, and J represents the tun-

neling strength between neighboring sites. The Hamiltonian commutes with the total particle number $N = N_1 + N_2 + N_3 + N_4$ where $N_j = a_j^\dagger a_j$. Moreover, the Hamiltonian is integrable when $U_{13} = U_{24} = U_0$ and $U_{12} = U_{14} = U_{23} = U_{34}$. It acquires two additional conserved operators

$$Q_1 = \frac{1}{2}(N_1 + N_3 - a_1^\dagger a_3 - a_3^\dagger a_1),$$
$$Q_2 = \frac{1}{2}(N_2 + N_4 - a_2^\dagger a_4 - a_4^\dagger a_2),$$

such that $[Q_1, Q_2] = [Q_j, H] = [Q_j, N] = 0$, $j = 1, 2$. Integrability results from derivation of the model through the Quantum Inverse Scattering Method. It is intimately related to exact solvability, due to the algebraic Bethe Ansatz [27]. Hereafter we only consider the integrable case.

Resonant tunneling regime.– It is straightforward to check that there are large energy degeneracies when $J = 0$. From numerical diagonalization of (1), with N particles and sufficiently small value of J, it is seen that the low-energy levels coalesce into well-defined bands, similar to that observed in an analogous integrable three-site model [10, 28]. In this regime, an effective Hamiltonian H_{eff} is obtained through consideration of second-order tunneling processes. For an initial Fock state $|M-l, P-k, l, k\rangle$, with total boson number $N = M+P$, the effective Hamiltonian is a simple function of the conserved operators

$$H_{\text{eff}} = (N+1)\Omega(Q_1 + Q_2) - 2\Omega Q_1 Q_2, \qquad (2)$$

where $\Omega = J^2/(4U((M-P)^2-1))$ with $U = (U_{12}-U_0)/4$. This result is valid for $J \ll U(M-P)$, which characterizes the resonant tunneling regime. For time evolution under H_{eff}, both $N_1 + N_3 = M$ and $N_2 + N_4 = P$ are constant. The respective $(M+1)$-dimensional subspace associated with sites 1 and 3 and $(P+1)$-dimensional subspace associated with sites 2 and 4 serve as two, coupled, hybrid qudits [19], and provide the state space for the relevant energy band (see Appendix A). This yields a robust approximation for the dynamics under (1), which we benchmark below. For later use we will designate the qudit associated with sites 1 and 3 as *qudit A*, and that associated with sites 2 and 4 as *qudit B*.

It is easily found, through Bogoliubov transformations, that the spectrum of H_{eff} is simply

$$E_{\text{eff}} = (N+1)\Omega(q_1 + q_2) - 2\Omega q_1 q_2$$

with $q_1 = 0, ..., M$ and $q_2 = 0, ..., P$. Thus the time evolution under H_{eff} is recognized as a controlled-phase gate [20, 21]. From here, several analytic results are accessible. For initial Fock state $|M, P, 0, 0\rangle$ it is found that the expectation value of the number imbalance between sites 1 and 3 is (in units where $\hbar = 1$)

$$\langle N_1 - N_3\rangle = M\cos((M+1)\Omega t)[\cos(\Omega t)]^P \qquad (3)$$

When $P = 0$, there are harmonic oscillations in the imbalance. For non-zero P, interference leads to a collapse and revival of oscillations. For comparison, results from numerical diagonalization of (1) are shown in the upper panels of Fig. 2

Other initial states can be studied, such as

$$|\Phi(\phi)\rangle = \frac{1}{\sqrt{2}}|M, P, 0, 0\rangle + \frac{\exp(i\phi)}{\sqrt{2}}|M, 0, 0, P\rangle, \qquad (4)$$

which is a product of a number state for site 1, vacuum for site 3 (qudit A), and a phase-dependent NOON state [1, 3] across sites 2 and 4 (qudit B). We find the following result for the imbalance between sites 1 and 3:

$$\langle N_1 - N_3\rangle = M\cos((M+1)\Omega t)[\cos(\Omega t)]^P \qquad (5)$$
$$+M\cos(\phi)\cos((M+1)\Omega t + \pi P/2)[\sin(\Omega t)]^P.$$

This formula provides excellent agreement with numerical calculations using (1). Illustrative examples are provided, for choices $\phi = 0$ and $\phi = \pi$, in the lower panels of Fig. 2.

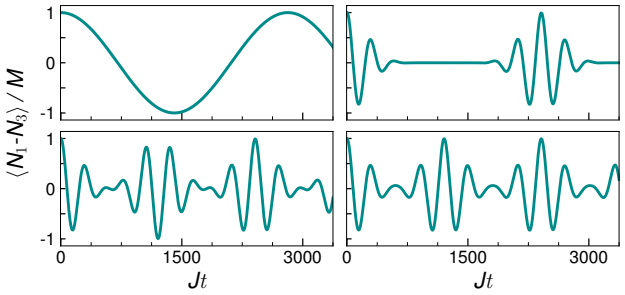

FIG. 2. Time evolution of expected fractional imbalance $\langle N_1 - N_3\rangle/M$ for the Hamiltonian (1) as a function of dimensionless time Jt, with $U/J = 8$ and different initial states. Upper panels: Left: $|15, 0, 0, 0\rangle$. Right: $|15, 10, 0, 0\rangle$. Bottom panels: $(|15, 10, 0, 0\rangle + \exp(i\phi)|15, 0, 0, 10\rangle)/\sqrt{2}$ with $\phi = 0$ on the left and $\phi = \pi$ on the right. The top panels display agreement with the formula (3), while the bottom panels are in agreement with (5).

NOON state identification and production.– The above results are sufficient to demonstrate the efficacy of the system to perform certain interferometric tasks. First consider a black box processor $\mathbb{P}$ that outputs one of two possible NOON states, either symmetric or antisymmetric. The output state, with particle number P, is loaded into qudit B. With M particles in site 1 and zero in site 3 of qudit A, this composite initial state is given by (4) with either $\phi = 0$ (symmetric) or $\phi = \pi$ (antisymmetric). Choose M such that $N = M + P$ is odd, let the system evolve for time $t_m = \pi/(2\Omega)$, and then measure the particle number at site 3. According to (5), there are only two possible measurement outcomes. One is to obtain the outcome zero, which occurs with probability 1 when $\phi = \pi$. The other is to obtain the outcome M, which occurs with probability 1 when $\phi = 0$ (cf. the

lower panels of Fig. 2, where the time of measurement is $t_m \approx 1206.37/J$). Moreover, this measurement is non-destructive and the NOON state in qudit B is preserved. See Appendix B for details.

This analytic result is an excellent approximation for the behavior governed by (1). From numerical results using the parameters of Fig. 2, we find that the success probability when $\phi = 0$ is 0.98699, and it is 0.98708 when $\phi = \pi$. This delivers a proof of principle example to show that the model (1) has capacity to perform interferometry with high accuracy.

One of the counter-intuitive features of this theoretical framework is the acute dependence on whether the total particle number $N = M + P$ is even or odd. To provide an understanding of this phenomenon, we take the initial state $|M, P, 0, 0\rangle$ and consider the time evolution of the *reduced density matrix* $\rho_{1,3}(t)$ for qudit A

$$\rho_{1,3}(t) = \mathrm{tr}_{2,4}\left(|\Psi(t)\rangle\langle\Psi(t)|\right)$$

where $\mathrm{tr}_{2,4}$ is the partial trace taken over the state space for qudit B, and $|\Psi(t)\rangle = \exp(-itH_{\mathrm{eff}})\,|M, P, 0, 0\rangle$. We then obtain

$$\rho_{1,3}\left(t_m\right) = \frac{1}{2}|\Psi_+\rangle\langle\Psi_+| + \frac{1}{2}|\Psi_-\rangle\langle\Psi_-| \tag{6}$$

where

$$|\Psi_\pm\rangle = \frac{1}{\sqrt{2^M}}\sum_{r=0}^{M}\sqrt{\binom{M}{r}}\exp\left(-i\frac{(N\pm 1)r\pi}{2}\right)|\chi(r)\rangle\,,$$
$$|\chi(r)\rangle = \frac{1}{\sqrt{2^M(M-r)!r!}}(a_1^\dagger + a_3^\dagger)^{M-r}(a_1^\dagger - a_3^\dagger)^r\,|0\rangle\,.$$

The above results then allow for a calculation of the probability $\mathcal{P}(r)$ that, measurement of the number of particles at site 3, when $t = t_m$, yields the outcome r. The result is

$$\mathcal{P}(r) = \frac{1}{2}b_{M,r}(\sin^2((N-1)\pi/4)) + \frac{1}{2}b_{M,r}(\sin^2((N+1)\pi/4))$$

where $b_{M,r}(x) = \binom{M}{r}x^r(1-x)^{M-r}$, $r = 1, ..., M$, are the *Bernstein polynomials*. When N is even,

$$\mathcal{P}(r) = \frac{1}{2^M}\binom{M}{r}.$$

When N is odd,

$$\mathcal{P}(r) = \frac{1}{2}\delta_{r,0} + \frac{1}{2}\delta_{r,M}. \tag{7}$$

The binomial distribution of the even case has maximal support, in stark contrast to the double delta function distribution of the odd case.

Remarkably, the earlier analysis on NOON state identification can now be inverted to show that the interferometer itself provides a high-fidelity simulation of the black box processor $\mathbb{P}$. For odd N it can be shown that

$$|\Psi\left(t_m\right)\rangle = \frac{(-1)^{(N+1)/2}}{2}\,|M, P, 0, 0\rangle + \frac{1}{2}\,|M, 0, 0, P\rangle + \frac{1}{2}\,|0, P, M, 0\rangle + \frac{(-1)^{(N-1)/2}}{2}\,|0, 0, M, P\rangle\,. \tag{8}$$

In accordance with the previous discussion, measurement at site 3 produces one of only two possible outcomes. A measurement outcome of M causes wavefunction collapse such that the state of qudit B is the symmetric (anti-symmetric) NOON state if $(N+1)/2$ is odd (even). Conversely, a measurement outcome of zero causes wavefunction collapse with an anti-symmetric (symmetric) NOON state in qudit B if $(N+1)/2$ is odd (even).

As before, it is useful to compare this result obtained from (2) against the analogous predictions of (1). Numerically, using the parameters of Fig. 2, we find that the outcome fidelity of this processor simulation for (1) is 0.99605 for outcome zero, and 0.99959 for outcome M, with respective probabilities of 0.497463 and 0.493898, close to the predictions of Eq. (7). Probabilities and fidelities for intermediate outcomes are provided in Appendix C.

Entanglement.– The ability to produce NOON states as described above is clearly dependent on the ability to create entanglement. More important is the ability to create "useful" entanglement since, as emphasized in the review article [1]: "Not all entangled states are useful for quantum metrology". See also [29]. Below we demonstrate how this notion applies in the present context.

It is convenient for our study to use the entanglement measure of *linear entropy* defined in terms of a density matrix ρ as [30, 31]

$$\mathcal{E}(\rho) = 1 - \mathrm{tr}(\rho^2).$$

The linear entropy is bounded between 0 and $1 - 1/d$, where d is the dimension of the space on which the density matrix acts. It follows from (6) that $\mathcal{E}(\rho_{1,3}(t_m)) = 1/2$. This result is independent of P. It asserts that immediately prior to making measurement at site 3, at time $t = t_m$, the entanglement between qudits A and B is *independent* of whether $N = M + P$ is even or odd.

Further, let $\rho_3(t_m) = \mathrm{tr}_1(\rho_{1,3}(t_m))$, which can be expressed compactly as

$$\rho_3(t_m) = \sum_{q=0}^{M}\mathcal{P}(q)\,|q\rangle\,\langle q|\,.$$

The linear entropy of ρ_3 quantifies the entanglement between the subsystems, sites 1 and 3, within qudit A. Now we encounter a difference between the even and odd

cases. When N is odd, $\mathcal{E}(\rho_3(t_m)) = 1/2$. For even N

$$\mathcal{E}(\rho_3(t_m)) = 1 - \frac{1}{2^{2M}}\binom{2M}{M} \sim 1 - \frac{1}{\sqrt{M\pi}}$$

where the second step invokes Stirling's approximation. By symmetry, the same conclusion can be drawn for qudit B (with M replaced by P). The curious observation to make here is that in the odd case, which enables a protocol for NOON state production, the pre-measurement entanglement within the qudits is *less* than that for the even case. While number-parity effects are ubiquitous in fermionic systems [32–36], they are less frequently encountered in bosonic models. The situation reported here displays some features in common with the work of [37].

Heisenberg-limited interferometry.– Finally, we establish that the system is capable of interferometry with sensitivity at the Heisenberg limit, through the archetypal example of parameter estimation through the phase of a NOON state [1, 3]. Consider initial state (4) with $N = M + P$ odd, and $\phi = 0$. A new phase φ is encoded into the bosons at site 4 through a transformation, $a_4^\dagger \mapsto \exp(i\varphi)a_4^\dagger$ (cf. [14]). This still corresponds to (4), but now with $\phi = P\varphi$, a phenomenon known as *phase super-resolution* [23, 24].

Again for time interval $t = t_m$, the imbalance between sites 1 and 3 is obtained from (5) as

$$\langle N_1 - N_3\rangle = (-1)^{(N+1)/2} M\cos(P\varphi).$$

Fig. 3 shows the dependence of the fractional population $\langle N_1 - N_3\rangle/M$ on parameters φ and the dimensionless time Jt.

Next, it can be confirmed that $\langle (N_1 - N_3)^2\rangle = M^2$, so

$$\Delta\langle N_1 - N_3\rangle = \sqrt{\langle (N_1 - N_3)^2\rangle - \langle N_1 - N_3\rangle^2} = M|\sin(P\varphi)|.$$

Using the standard estimation theory approach [1, 3], it is found that the system achieves Heisenberg-limited phase sensitivity since

$$\Delta\varphi = \frac{\Delta\langle N_1 - N_3\rangle}{|\mathrm{d}\langle N_1 - N_3\rangle/\mathrm{d}\varphi|} = \frac{1}{P}.$$

This is an improvement on the classical shot-noise case where $\Delta\varphi \sim 1/\sqrt{P}$ [1, 3].

Conclusion.– We have provided an example of integrable atomtronic interferometry, through an extended Bose-Hubbard model, with four sites arranged in a closed square. The integrable properties of the model furnished the necessary tools to understand the dynamics of the system in the resonant tunneling regime. It allowed for the analytic calculation of dynamical expectation values. This, in turn, informed the relevant time interval required to implement certain measurement protocols. The probabilities for measurement outcomes were computed through the density matrix. We demonstrated proof of principle examples that the integrable system functions as an identifier of NOON states produced by a black box processor, and as a simulator of such a processor.

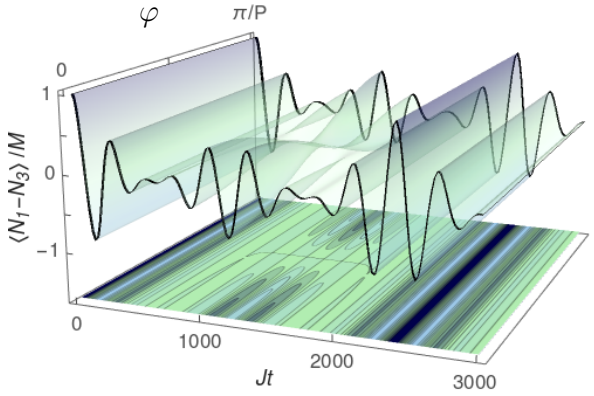

FIG. 3. Dependence of $\langle N_1 - N_3\rangle/M$ as a function of dimensionless Jt and phase φ, for initial state (4) with $M = 15$, $P = 10$, $\phi = P\varphi$, and $U/J = 8$. Upper surface: The colors range from light to dark blue, indicating lower and higher values for the imbalance population. The green color represents the region where $\langle N_1\rangle \approx \langle N_3\rangle$. Lower plane: The effect on the system's dynamics is highlighted, specifically for the limiting cases $\varphi = 0$ and $\varphi = \pi/P$, where it is seen that there is a minimum-maximum inversion at $t_m \approx 1206.373/J$.

Our study highlights the quantum information connections of the model by detailing its function as a hybrid qudit system subjected to a controlled-phase gate operation. This description complements other qudit studies in photonic [38–40] and NMR [41] settings, which are attracting attention due to the promise of increasing quantum computational capacity. It is anticipated that our results, in an atomtronic framework, may be transferable to these and other contexts.

In future research, we will undertake studies involving other states which may be useful for metrological applications, such as coherent states and Dicke states. We will examine the evolution of these input states, and investigate the resulting generation of entanglement. Particular emphasis will be given to the understanding of multipartite entanglement generation, beyond the bipartite investigations reported here.

D.S.G. and K.W.W. were supported by CNPq (Conselho Nacional de Desenvolvimento Científico e Tecnológico), Brazil. A.F. acknowledges support from CNPq - Edital Universal 430827/2016-4. A.F. and J.L. received funding from the Australian Research Council through Discovery Project DP200101339. J.L. acknowledges the traditional owners of the land on which The University of Queensland is situated, the Turrbal and Jagera people.

[1] L. Pezzé et al., Rev. Mod. Phys. **80**, 035005 (2018).
[2] K. Bongs, et al., Nature Reviews Physics **1**, 731 (2019).
[3] H. Lee, et al., J. Mod. Opt. **49**, 2325 (2002).
[4] C. Gross and I. Bloch, Science **357**, 995 (2017).
[5] R.A. Pepino et al., Phys. Rev. Lett. **103**, 140405 (2009).
[6] R. Dumke, et al., J. Opt. **18**, 093001 (2016).
[7] L. Amico, et al., New J. Phys. **19**, 020201 (2017).
[8] S Pandey, et al., Nature **570**, 205 (2019).
[9] M.K. Olsen and A.S. Bradley, Phys. Rev. A **91**, 043635 (2015).
[10] K. Wittmann Wilsmann, et al., Commun. Phys. **1**, 91 (2018).
[11] T. Haug, et al., Phys. Rev. A **97**, 013633 (2018).
[12] J. Polo, et al., Phys. Rev. Lett. **123**, 195301 (2019).
[13] E. Compagno, et al., arXiv:191201092.
[14] T. Lahaye, et al., Phys. Rev. Lett. **104**, 170404 (2010).
[15] D. Poilblanc, et al., Europhys. Lett. **22**, 537 (1993).
[16] L.F. Santos and M. Rigol, Phys. Rev. E **81**, 036206 (2010).
[17] P. Calabrese, et al., J. Stat. Mech. 064001 (2016).
[18] T. Kinoshita, et al., Nature **440**, 900 (2006).
[19] J. Daboul, et al., J. Phys. A: Math. Gen. **36**, 2525 (2003).
[20] A. Muthukrishnan and C.R. Stroud Jr., Phys. Rev. A **62**, 052309 (2000).
[21] G.K. Brennen, et al., Phys. Rev. A **71**, 052318 (2005).
[22] G.J. Pryde and A.G. White, Phys. Rev. A **68**, 052315 (2003).
[23] M.W. Mitchell et al., Nature **429**, 161 (2004).
[24] K.J. Resch, et al., Phys. Rev. Lett. **98**, 223601 (2007).
[25] M.A. Baranov, Phys. Rep. **464**, 71 (2008).
[26] T. Lahaye et al., Rep. Prog. Phys. **72**, 126401 (2009).
[27] A.P. Tonel, et al., J. Phys. A: Math. Theor. **48**, 494001 (2015).
[28] A.P. Tonel, et al., SciPost Phys. Core **2**, 003 (2020).
[29] T.R. Bromley, et al., Phys. Rev. A **95**, 052313 (2017).
[30] W.H. Zurek, et al., Phys. Rev. Lett. **70**, 1187 (1993).
[31] F. Buscemi, et al., Phys. Rev. A **75**, 032301 (2007).
[32] K.A. Matveev and A.I. Larkin, Phys. Rev. Lett. **78**, 3749 (1997).
[33] G, Zürn, et al., Phys. Rev. Lett. **111**, 175302 (2013).
[34] S. Matsuo, et al., Sci. Rep. **5**, 11723 (2015).
[35] C. Schilling and R. Schilling, Phys. Rev. A **93**, 021601 (2016).
[36] E.T. Mannila, et al., Phys. Rev. B **100**, 020502(R) (2019).
[37] D. Agboola, et al., J. Phys. B: At. Mol. Opt. Phys. **51**, 14530 (2018).
[38] R.-B. Jin, et al., Quantum Sci. Technol. **1**, 015004 (2016).
[39] M. Kues, et al., Nature **546**, 622 (2017).
[40] P. Imany, et al., npj Quantum Inf. **5**, 59 (2019).
[41] A. Z. Khoury et al., Phys. Rev. A **97**, 042343 (2018).

APPENDIX

A. Energy bands and effective Hamiltonian

Here we give an overview of the origin for the effective Hamiltonian (2). Recall that the integrability condition is $U_{13} = U_{24} = U_0$ and $U_{12} = U_{23} = U_{34} = U_{14}$. When

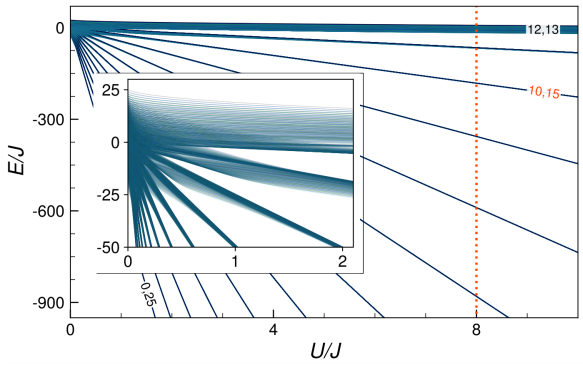

FIG. 4. Dimensionless energy eigenvalues E/J as a function of dimensionless coupling U/J, where $U = (U_{12} - U_0)/4$ and $C = 0$. Results are shown for $N = 25$, with M and P indicating the dependence of (9) in the $J \to 0$ limit. The orange vertical line is $U/J = 8$, for which quantum dynamics is described in Fig. 2, (except for the top left panel). The inset shows the large J limit, in which the bands begin to merge.

$J = 0$, the Fock state $|M - l, P - k, l, k\rangle$ is eigenstate of the Hamiltonian (1) with energy

$$E = C + \frac{U_0 - U_{12}}{4}(M - P)^2 \tag{9}$$

with $C = (U_0 + U_{12})N^2/4 - U_0/2$, independent of l and k, indicating degeneracies. For small values of J, the degeneracies are broken and lead to energy levels in well-defined bands, each with $2(M + 1)(P + 1)$ energy levels, except for N even, where the band with the highest energy, $M = P$, will have $(M + 1)(P + 1)$ levels. The level energy structure of the case we are analyzing, with N = 25, is shown in Fig. 4. In it, we highlight in red the band with $M = 15$ and $P = 10$ (and vice versa).

An effective Hamiltonian for each band is obtained by consideration of second-order processes. Associated to labels M and P, such that $N = M + P$, we obtain

$$\begin{aligned}
H_{\text{eff}} = &\frac{J^2}{16U(M-P+1)}\left(a_1a_3^\dagger + a_3a_1^\dagger\right)\left(a_2^\dagger a_2 + a_4^\dagger a_4\right) \\
&+ \frac{J^2}{16U(M-P+1)}\left(a_1a_1^\dagger + a_3a_3^\dagger\right)\left(a_2^\dagger a_4 + a_4^\dagger a_2\right) \\
&- \frac{J^2}{16U(M-P-1)}\left(a_2a_2^\dagger + a_4a_4^\dagger\right)\left(a_1^\dagger a_3 + a_3^\dagger a_1\right) \\
&- \frac{J^2}{16U(M-P-1)}\left(a_2a_4^\dagger + a_4a_2^\dagger\right)\left(a_1^\dagger a_1 + a_3^\dagger a_3\right) \\
&+ \frac{J^2}{16U}\left(\frac{1}{M-P+1} - \frac{1}{M-P-1}\right) \\
&\times \left(a_1^\dagger a_2 a_3 a_4^\dagger + a_1^\dagger a_2^\dagger a_3 a_4 + a_1 a_2^\dagger a_3^\dagger a_4 + a_1 a_2 a_3^\dagger a_4^\dagger\right).
\end{aligned}$$

This expression is equivalent to (2), up to a constant.

B. Non-destructive measurement

Here we show that the measurement protocol for NOON state identification using the effective Hamiltonian (2) is non-destructive with respect to qudit B. To establish this, it suffices to show that at measurement time t_m there is no entanglement between the qudits, such that a measurement performed on qudit A does not cause wavefunction collapse for qudit B.

From (4) define $|\Lambda(t,\phi)\rangle = \exp(-itH_{\text{eff}})\,|\Phi(\phi)\rangle$. Generalizing Eq. (8) it is found that (recall N is chosen to be odd)

$$\begin{aligned}|\Lambda(t_m,0)\rangle &= \frac{K(N+1,0)}{2\sqrt{2}}(|M,P,0,0\rangle + |M,0,0,P\rangle)\\ &\quad + \frac{K(N-1,0)}{2\sqrt{2}}(|0,0,M,P\rangle + |0,P,M,0\rangle),\\ |\Lambda(t_m,\pi)\rangle &= \frac{K(N+1,\pi)}{2\sqrt{2}}(|M,P,0,0\rangle - |M,0,0,P\rangle)\\ &\quad + \frac{K(N-1,\pi)}{2\sqrt{2}}(|0,0,M,P\rangle - |0,P,M,0\rangle)\end{aligned}$$

where $K(m,\phi) = (-1)^{m/2} + \exp(i\phi)$. Note that one of $K(N+1,\phi)$ and $K(N-1,\phi)$ is necessarily zero for N odd and $\phi = 0,\pi$.

It is recognized from the above equations that the possible measurements of the number of particles at site 3 are either 0 or M, and always occur with probability 1. Moreover, the post-measurement state of qudit B is a NOON state with the same symmetry or antisymmetric as the input NOON state for qudit B. That is, the identification of the NOON state loaded into qudit B is achieved without destruction of the NOON state.

C. Probabilities and fidelities

Here we provide benchmarks establishing the effectiveness of Hamiltonian (1) in the simulation of the black box processor $\mathcal{P}$, through numerical calculation of probabilities and outcome fidelities. A general N-particle state can be expressed as

$$|\Theta\rangle = \sum_{j,k,l=0}^{N} c_{j,k,l}|j,k,l,N-j-k-l\rangle$$

such that $c_{j,k,l} = 0$ if $j+k+l > N$, and $\sum_{j,k,l=0}^{N} |c_{j,k,l}|^2 = 1$. When a measurement is made at site 3, the probability $\mathcal{P}(r)$ to obtain the measurement outcome r is

$$\mathcal{P}(r) = \sum_{j,k=0}^{N} |c_{j,k,r}|^2 \tag{10}$$

satisfying $\sum_{r=0}^{N}\mathcal{P}(r) = 1$. After the measurement, the wavefunction collapses to

$$|\Theta(r)\rangle = \frac{1}{\sqrt{\mathcal{P}(r)}}\sum_{j,k=0}^{N} c_{j,k,r}|j,k,r,N-j-k-r\rangle$$

such that $\langle\Theta(r)|\Theta(r)\rangle = 1$. Set

$$|\Phi(r,\phi)\rangle = \frac{1}{\sqrt{2}}\,|M-r,P,r,0\rangle + \frac{\exp(i\phi)}{\sqrt{2}}\,|M-r,0,r,P\rangle$$

and define the outcome fidelity $\mathcal{F}(r,\phi)$ to be

$$\mathcal{F}(r,\phi) = |\langle\Phi(r,\phi)|\Theta(r)\rangle|. \tag{11}$$

We take $|\Theta\rangle = \exp(-it_mH)\,|15,10,0,0\rangle$ and use (1) with $U/J = 8$ to numerically calculate the measurement probabilities and outcome fidelities through (10,11). The results are given below in Table 1.

Measurement r	Probability $\mathcal{P}(r)$	Phase ϕ	Fidelity $\mathcal{F}(r,\phi)$
15	0.493898	0	0.999593
14	0.002814	0	0.600630
13	0.000237	0	0.515582
12	0.000149	0	0.070958
11	0.000311	0	0.023097
10	0.001182	0	0.002501
9	0.000252	0	0.007847
8	0.000235	0	0.011905
7	0.000231	π	0.014797
6	0.000254	π	0.010138
5	0.000168	π	0.022435
4	0.000176	π	0.026081
3	0.000144	π	0.057712
2	0.000291	π	0.449405
1	0.001398	π	0.839876
0	0.497463	π	0.996048

TABLE I. Measurement probabilities and fidelities after evolution under (1) until time t_m. The initial state is $|15,10,0,0\rangle$, and $U/J = 8$ as used in Figs. 2, 3, 4. The calculations show that the highest fidelity outcomes, close to 1, occur with the highest probabilities, close to 1/2. This is in agreement with the results predicted by the effective Hamiltonian (2).

B.0.2 Atomtronic protocol designs for NOON states

Daniel S. Grün, Karin Wittmann W., Leandro H. Ymai, Jon Links & Angela Foerster
arXiv:2102.02944

Atomtronic protocol designs for NOON states

Daniel S. Grün[1], Karin Wittmann W.[1], Leandro H. Ymai[2], *Jon Links[3] & Angela Foerster[1]

[1] Instituto de Física da UFRGS, Av. Bento Gonçalves 9500, Agronomia, Porto Alegre, 91501-970, RS, Brazil

[2] Universidade Federal do Pampa, Av. Maria Anunciação Gomes de Godoy 1650, Malafaia, Bagé, 96413-170, RS, Brazil

[3] School of Mathematics and Physics, The University of Queensland, Brisbane, QLD, 4072, Australia

*Corresponding author

Abstract

The ability to reliably prepare non-classical states will play a major role in the realization of quantum technology. NOON states, belonging to the class of Schrödinger cat states, have emerged as a leading candidate for several applications. Starting from a model of dipolar bosons confined to a closed circuit of four sites, we show how to generate NOON states. This is achieved by designing protocols to transform initial Fock states to NOON states through use of time evolution, application of an external field, and local projective measurements. By variation of the external field strength, we demonstrate how the system can be controlled to encode a phase into a NOON state. We also discuss the physical feasibility, via an optical lattice setup. Our proposal illuminates the benefits of quantum integrable systems in the design of atomtronic protocols.

Quantum systems are widely considered to be the most promising foundation for the next generation of platforms in computing, communication, measurement and simulation. This is primarily due to the properties of state superposition and entanglement. To realize the potential for progress, it is necessary to establish protocols that are capable of generating important quantum states.

The NOON state is a fundamental example. It is an "all and nothing" superposition of two different modes[1,2]. For N particles, it has the form

$$|\text{NOON}\rangle = \frac{1}{\sqrt{2}}\left(|N,0\rangle + e^{i\varphi}|0,N\rangle\right) \tag{1}$$

where the phase φ typically records information in applications. These include: in the fields of quantum metrology and sensing, performing precision phase-interferometry at the Heisenberg limit[3] and overcoming diffraction limits in quantum lithography[4]; in tests of fundamental physics, NOON states are used to study Bell-type inequalities violation[5]; they offer promising applications in Quantum Communication and Quantum Computing[6], and their utilization is expected to extend to areas such as chemistry and biology[7]. After an early success, using photon pairs and Hong-Ou-Mandel (HOM) interferometry[8], several schemes have followed for the production and detection of photonic NOON states[2,9–12]. There are also proposals using other architectures, such as circuit QED[13], trapped ions[14], and Bose-Einstein condenstates[15].

The atomtronic creation of Bose-atom NOON states would enable new tests, using massive states, of the foundations for quantum mechanics. One step in this direction is a proposal to demonstrate the matter-wave equivalent of the HOM effect[16]. Prospects for creating Bose-atom NOON states using a double-well potential were first floated some time ago[17]. This early work considered an attractive system, which is prone to instability. In principle a more robust repulsive system can be prepared to evolve to a high-fidelity approximation of a NOON state. However, the drawback there is that the process is associated with an extremely large time scale. Recently, new studies of the double-well system have been undertaken to reduce the time scale. One example proposes to adiabatically vary the system parameters through an excited-state phase transition during the process[18]. Another study employs periodic driving to lower the NOON-state evolution time[19]. Nonetheless, the time to generate a NOON state in these examples still, increasingly, scales with the total number of particles.

Here we present an alternative to circumvent these issues. Our approach adopts a closed-circuit of four sites, with a Fock-state input of M particles in site 1, P particles in site 2, and no particles in sites 3 and 4, denoted as $|\Psi_0\rangle = |M,P,0,0\rangle$. The initial step is to create an uber-NOON state, with the general form

$$|\text{u-NOON}\rangle = \frac{1}{2}\left(|M,P,0,0\rangle + e^{i\varphi_1}|M,0,0,P\rangle + e^{i\varphi_2}|0,P,M,0\rangle + e^{i\varphi_3}|0,0,M,P\rangle\right)$$

for a set of phases $\{\varphi_1, \varphi_2, \varphi_3\}$. This state may be viewed as an embedding of NOON states (1) within two-site subsystems. We then describe two protocols to extract a NOON state from an uber-NOON state, one through dy-

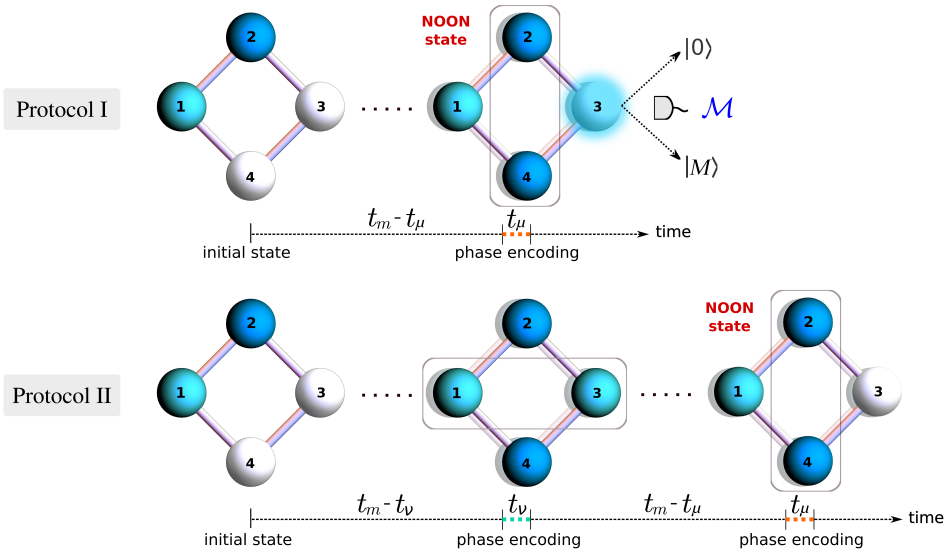

Figure 1. NOON state generation scheme. The four circles on the left represent the initial state, with white indicating an empty site, cyan and blue corresponding to M and P particles respectively. The solid lines connecting the circles denote tunneling between nearest neighbor sites. Rectangles represent applied external fields to sites 1-3 and 2-4. In Protocol I, the system initially evolves during a time of $t_{\rm m} - t_\mu$. Then, an applied field across sites 2-4 is switched on, and a phase is encoded during the time t_μ. Finally, the light blue halo portrays a projective measurement process at site 3, denoted by $\mathcal{M}$, resulting in two possible NOON states across sites 2-4. In Protocol II, the system first evolves during a time of $t_{\rm m} - t_\nu$. Then, an applied field to sites 1-3 is switched on for time t_ν. Next, the system evolves for $t_{\rm m} - t_\mu$, after which the applied field to sites $2-4$ is switched on. This results in a NOON state across sites 2-4 without performing a measurement procedure.

namical evolution followed by local projective measurement and post-selection, the other from dynamical evolution alone. The protocols are schematically presented in Fig. 1.

The approach taken has the following properties: (i) The system has long-ranged interactions, described by the Extended Bose-Hubbard Model (EBHM)[20]. There exists a choice of the coupling parameters for which this model is integrable[21]. As in other physically realized integrable systems[22–29], this property facilitates several analytic calculations for physical quantities. Here, integrability exposes the protocols available for NOON state generation. The execution time is found to be dependent on the difference between the two initially populated sites within the four-site system. It is independent of total particle number, offering an encouraging prospect for scalability. (ii) The system can be controlled by breaking the integrability over small time scales. Encoding of the phase into a NOON state only requires breaking of integrability over an interval that is several orders of magnitude smaller than the entire execution time. This causes minimal loss in fidelity. (iii) With currently available technology, the system may be realized and controlled using dipolar atoms (e.g. dysprosium or erbium) trapped in an optical lattice[30,31]. In this setup, the evolution times that we compute for NOON-state generation are of the order of seconds.

For the four-site configuration, the EBHM Hamiltonian is

$$H = \frac{U_0}{2}\sum_{i=1}^{4} N_i(N_i-1) + \sum_{i=1}^{4}\sum_{j=1,j\neq i}^{4}\frac{U_{ij}}{2}N_iN_j - \frac{J}{2}\left[(a_1^\dagger + a_3^\dagger)(a_2+a_4) + (a_1+a_3)(a_2^\dagger + a_4^\dagger)\right], \tag{2}$$

where $a_j^\dagger$, a_j are the creation and annihilation operators for site j, and $N_j = a_j^\dagger a_j$ are the number operators. The total number operator $N = N_1 + N_2 + N_3 + N_4$ is conserved. Above, U_0 characterizes the interaction between bosons at the same site, $U_{ij} = U_{ji}$ is related to the long-range (e.g. dipole-dipole) interaction between bosons at sites i and j, and J accounts for the tunneling strength between different sites.

Below, we describe two protocols that enable the generation of NOON states, with fidelities greater than 0.9. A physical setup to implement them, drawn on currently available technology, is discussed.

Results

Insights into the physical behaviour of Eq. (2) become accessible at integrable coupling. Setting $U_{13} = U_{24} = U_0$, the system acquires two additional conserved quantities, Q_1 and Q_2, such that $2Q_1 = N_1 + N_3 - a_1^\dagger a_3 - a_1 a_3^\dagger$ and $2Q_2 = N_2 + N_4 - a_2^\dagger a_4 - a_2 a_4^\dagger$. Together with the total number of particles N and the Hamiltonian H, the system possesses four independent, conserved quantities. This is equal to the number of degrees of freedom, satisfying the criterion for integrability. Suppose that, initially, there are M atoms in site 1 and P atoms in site 2. We identify the resonant tunneling regime as being achieved when $U|M-P| \gg J$ (see Methods for details), where $U = (U_{12} - U_0)/4$. This regime is characterized by sets of bands in the energy spectrum (see Supplementary Note 1). In this region, an effective Hamiltonian H_{eff} enables the derivation of analytic expressions for several physical quantities.

In the settings discussed above, the system described by Eq. (2) provides the framework to generate uber-NOON states when $N = M + P$ is odd[32]. To encode phases, however, it is necessary to break the integrability in a controllable fashion. Here, we introduce two idealized protocols to produce NOON states with general phases by breaking the system's integrability with externally applied fields. We call the subsystem containing sites $1, 3$ as A, and the one containing sites $2, 4$ as B. We denote three time intervals: t_{m}, t_μ and t_ν. The first, corresponding to integrable time evolution, is associated with evolution to a particular uber-NOON state. The others, associated with smaller scale non-integrable evolution, produce phase encoding. Both protocols are built around a general time-evolution operator

$$\mathcal{U}(t,\mu,\nu) = \exp\left(-\frac{it}{\hbar}[H + \mu(N_2 - N_4) + \nu(N_1 - N_3)]\right),$$

where the applied field strengths μ, ν implement the breaking of integrability. It is convenient to introduce the phase variable $\theta = 2\mu t_\mu/\hbar$, and to fix $t_\nu = \hbar\pi/(4M\nu)$, with $\hbar$ the reduced Planck constant.

Protocol I

In this protocol we employ breaking of integrability through an applied field to subsystem B and a measurement process. The protocol consists of three sequential steps, schematically depicted in Fig. 1:

(i) $|\Psi_1^{\text{I}}\rangle = \mathcal{U}(t_{\text{m}} - t_\mu, 0, 0)\,|\Psi_0\rangle$;

(ii) $|\Psi_2^{\text{I}}\rangle = \mathcal{U}(t_\mu, \mu, 0)\,|\Psi_1^{\text{I}}\rangle$;

(iii) $|\Psi_3^{\text{I}}\rangle = \mathcal{M}\,|\Psi_2^{\text{I}}\rangle$,

where $t_{\text{m}} = \hbar\pi/(2\Omega)$ (see Methods) and $\mathcal{M}$ represents a projective measurement of the number of bosons at site 3 (which could be implemented, in principle, through Faraday rotation detection[33,34]). A measurement outcome of 0 or M heralds a high-fidelity NOON state in subsystem B. For other measurement outcomes, the output is discarded and the process repeated (post-selection).

Idealized limit

There is an idealized limit for which the above protocol has perfect success probability and output fidelity. Taking $t_\mu \to 0$, $\mu \to \infty$ such that θ remains finite, and using the effective Hamiltonian, provides explicit expressions for the uber-NOON states that result at steps (i) and (ii)

$$\begin{aligned}
|\Psi_1^{\text{I}}\rangle &= \frac{1}{2}\Big(\beta\,|M,P,0,0\rangle + |M,0,0,P\rangle \\
&\qquad + |0,P,M,0\rangle - \beta\,|0,0,M,P\rangle\Big) \\
|\Psi_2^{\text{I}}\rangle &= \frac{1}{2}\Big(\beta\,|M,P,0,0\rangle + e^{iP\theta}\,|M,0,0,P\rangle \\
&\qquad + |0,P,M,0\rangle - \beta e^{iP\theta}\,|0,0,M,P\rangle\Big)
\end{aligned} \tag{3}$$

Note that due to the conservation of $N_1 + N_3$ and $N_2 + N_4$ under the effective Hamiltonian, Fock states such as $|M,0,P,0\rangle$ and $|0,M,0,P\rangle$ do not appear in the above expression. Next, the two possible states at step (iii) depend on the measurement outcome r at site 3:

$$|\Psi_3^{\text{I}}\rangle = \begin{cases} \frac{1}{\sqrt{2}}\left(\beta\,|M,P,0,0\rangle + e^{iP\theta}\,|M,0,0,P\rangle\right), & r = 0, \\ \frac{1}{\sqrt{2}}\left(|0,P,M,0\rangle - \beta e^{iP\theta}\,|0,0,M,P\rangle\right), & r = M, \end{cases} \tag{4}$$

with $\beta = (-1)^{(N+1)/2}$. These states are recognized as products of a NOON state for subsystem B with Fock basis states for subsystem A.

In the non-ideal case with non-zero t_μ and finite μ, there is a small probability that the measurement outcome r is neither 0 or M. Numerical benchmarks for the measurement probabilities and NOON state output fidelities are provided in a later section. Next, we describe a second protocol.

Protocol II

Now we specify an alternative protocol that does not involve measurements, so post-selection is not required. Employing the same initial state $|\Psi_0\rangle$, the following sequence of steps are implemented to arrive at a NOON state in subsystem B (illustrated in Fig. 1):

(i) $|\Psi_1^{\text{II}}\rangle = \mathcal{U}(t_{\text{m}} - t_\nu, 0, 0)\,|\Psi_0\rangle$;

(ii) $|\Psi_2^{\text{II}}\rangle = \mathcal{U}(t_\nu, 0, \nu)\,|\Psi_1^{\text{II}}\rangle$;

(iii) $|\Psi_3^{\rm II}\rangle = \mathcal{U}(t_{\rm m}-t_\mu,0,0)\,|\Psi_2^{\rm II}\rangle$;

(iv) $|\Psi_4^{\rm II}\rangle = \mathcal{U}(t_\mu,\mu,0)\,|\Psi_3^{\rm II}\rangle$.

Idealized limit

Similar to Protocol I, in the limit $\mu,\nu\to\infty$, $t_\mu, t_\nu \to 0$, and implementing $\mathcal{U}(t,\mu,\nu)$ with the effective Hamiltonian produces

$$
\begin{aligned}
|\Psi_1^{\rm II}\rangle &= \frac{1}{2}\Big(\beta\,|M,P,0,0\rangle + |M,0,0,P\rangle \\
&\quad + |0,P,M,0\rangle - \beta\,|0,0,M,P\rangle\Big);\\
|\Psi_2^{\rm II}\rangle &= \frac{1}{2}\Big(\beta\,|M,P,0,0\rangle + |M,0,0,P\rangle \\
&\quad + i\,|0,P,M,0\rangle - i\beta\,|0,0,M,P\rangle\Big);\\
|\Psi_3^{\rm II}\rangle &= \frac{1}{\sqrt{2}}\Big(|M,P,0,0\rangle + \beta e^{-i\pi/2}\,|M,0,0,P\rangle\Big);\\
|\Psi_4^{\rm II}\rangle &= \frac{1}{\sqrt{2}}\Big(|M,P,0,0\rangle + \Upsilon\,|M,0,0,P\rangle\Big)
\end{aligned}
\tag{5}
$$

where $\Upsilon = \beta\exp(i(P\theta-\pi/2))$.

Protocol fidelities

The analytic results provided above are obtained by employing the effective Hamiltonian in an extreme limit, with divergent applied fields acting for infinitesimally small times. Below we give numerical simulations of the protocols to show that, for physically realistic settings where the fields are applied for finite times, high-fidelity outcomes for NOON state production persist.

Throughout this section, we use $|\Psi\rangle$ to denote an analytic state, obtained in an idealized limit. We adopt $|\Phi\rangle$ to denote a numerically calculated state, obtained by time evolution with the EBHM Hamiltonian (2). Two sets of parameters are chosen to illustrate the results (expressed in Hz):

Set 1: $\{U/\hbar = 75.876,\ J/\hbar = 24.886,\ \mu/\hbar = 20.870\}$;
Set 2: $\{U/\hbar = 76.519,\ J/\hbar = 73.219,\ \mu/\hbar = 15.168\}$.

For all numerical simulation results presented below, the initial state is chosen as $|\Psi_0\rangle = |4,11,0,0\rangle$, i.e. $M=4$ and $P=11$.

The fidelities of Protocols I and II are defined as[35] $F_{\rm I} = |\langle\Psi_3^{\rm I}|\Phi_3^{\rm I}\rangle|$ and $F_{\rm II} = |\langle\Psi_4^{\rm II}|\Phi_4^{\rm II}\rangle|$, respectively. This is computed for $P\theta$ ranging from 0 to π, achieved by varying t_μ. In the case of Protocol II, we use $\nu=\mu$ for both sets of parameters. The systems considered here can, in principle, be implemented using existing hardware – see Physical proposal.

The results are presented in Fig. 2, where it is seen that $F_{\rm II}$ is lower than $F_{\rm I}$. This can be attributed to two primary causes. The first is that, while Protocol I takes $\tau_I \sim t_{\rm m}$ to produce the final state, Protocol II requires double the evolution time $\tau_{II}\sim 2t_{\rm m}$. The longer evolution time contributes to a loss in fidelity. The second reason is that, the measurement occurring in the final step of Protocol I has the effect of renormalizing the quantum state after collapse, which increases the fidelity of the resulting NOON state when a measurement of $r=0$ or $r=M$ is obtained. However, there is a finite probability that the measurement outcome is neither $r=0$ nor $r=M$ (see Supplementary Note 2).

In summary, both protocols display high fidelity results greater than 0.9. For Protocol I the outcomes are probabilistic (See Supplementary Note 2 for data). By contrast, the slightly lower fidelity results of Protocol II are deterministic.

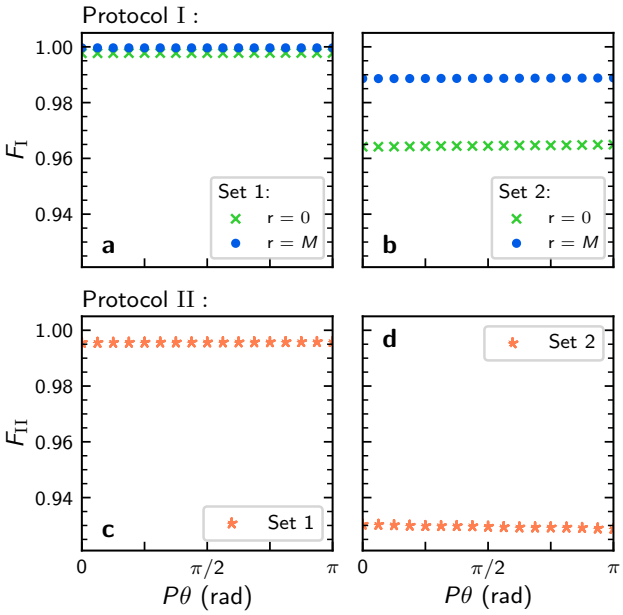

Figure 2. Fidelities for Protocols I and II. Numerical calculations of the fidelities $F_{\rm I}$ (**a** and **b**) and $F_{\rm II}$ (**c** and **d**). To vary $P\theta$, μ is fixed and t_μ is varied. **a**, **c** Set 1: $U/\hbar = 75.876$ Hz, $J/\hbar = 24.886$ Hz, $\mu/\hbar = 20.870$ Hz, $t_{\rm m}\sim 36.950$s, $t_\nu\sim 0.009$s and t_μ varies from $t=0$ to $t\simeq 0.007$s, such that $P\theta\in[0,\pi]$. **b**, **d** Set 2: $U/\hbar = 76.519$ Hz, $J/\hbar = 73.219$ Hz, $\mu/\hbar = 15.168$ Hz, $t_{\rm m}\sim 4.248$s, $t_\nu\sim 0.013$s, and t_μ varies from $t=0$ to $t\simeq 0.009$s, such that $P\theta\in[0,\pi]$. The required times $t_{\rm m}$, $2t_{\rm m}$ to produce the NOON states are comparable with typical lifetimes of optical lattice traps, which can be as large as a few minutes[36].

Readout statistics

A means to test the reliability of the system, through a statistical analysis of local measurement outcomes, is directly built into the design. This results from the system's

capacity to function as an interferometer[32]. For both protocols, once the output state has been attained we can continue to let the system evolve under $\mathcal{U}(t_{\rm m},0,0)$. This yields the readout states, denoted as $|\Psi^{\rm I}_{\rm RO}\rangle$, $|\Psi^{\rm II}_{\rm RO}\rangle$ respectively for protocols I and II. In the idealized limits these are

$$|\Psi^{\rm I}_{\rm RO}\rangle = \begin{cases} \frac{c(\theta)}{\sqrt{2}}(|M,P,0,0\rangle + \beta\,|M,0,0,P\rangle) \\ + \frac{is(\theta)}{\sqrt{2}}(\beta\,|0,P,M,0\rangle - |0,0,M,P\rangle), \;\; r=0, \\ \\ \frac{c(\theta)}{\sqrt{2}}(|M,P,0,0\rangle - \beta\,|M,0,0,P\rangle) \\ - \frac{is(\theta)}{\sqrt{2}}(\beta\,|0,P,M,0\rangle - |0,0,M,P\rangle), \;\; r=M, \end{cases}$$

$$|\Psi^{\rm II}_{\rm RO}\rangle = \frac{1}{\sqrt{2}}s\left(\theta-\frac{\pi}{2P}\right)(|M,P,0,0\rangle + \beta\,|M,0,0,P\rangle) - \frac{i}{\sqrt{2}}c\left(\theta-\frac{\pi}{2P}\right)(\beta\,|0,P,M,0\rangle - |0,0,M,P\rangle),$$

where $c(\theta) \equiv \cos(P\theta/2)$ and $s(\theta) \equiv \sin(P\theta/2)$. For $|\Psi^{I}_{\rm RO}\rangle$, the measurement probabilities at site 3 are $\mathcal{P}(0) = \cos^2(P\theta/2)$ and $\mathcal{P}(M) = \sin^2(P\theta/2)$. Combined with the probability of measuring $r=0,M$ in step (iii), we obtain four possibilities for the total probabilities as $\mathcal{P}_{\rm I}(0,0) = \mathcal{P}_{\rm I}(M,0) = 0.5\cos^2(P\theta/2)$ and $\mathcal{P}_{\rm I}(0,M) = \mathcal{P}_{\rm I}(M,M) = 0.5\sin^2(P\theta/2)$. Meanwhile, for $|\Psi^{II}_{\rm RO}\rangle$, the measurement probabilities at site 3 are $\mathcal{P}_{\rm II}(0) = \sin^2(P\theta/2-\pi/4)$ and $\mathcal{P}_{\rm II}(M) = \cos^2(P\theta/2-\pi/4)$. As a numerical check, we consider the same sets of parameters from previous section. Then, we numerically calculate the above probabilities using the Hamiltonian (2), comparing the predicted analytic results with the numerical ones, as shown in Fig. 3. See Supplementary Note 2 for numerical probabilities of Protocol I, and related fidelity data. For results with Set 2, see Supplementary Note 3.

Methods

Resonant tunneling regime

The Hamiltonian (2) has large energy degeneracies when $J=0$. Through numerical diagonalization of the intergable Hamiltonian for sufficiently small values of J, it is seen that the levels coalesce into well-defined bands, similar to that observed in an analogous integrable three-site model[37,39]. By examination of second-order tunneling processes (see Supplementary Note 1) In this regime, an effective Hamiltonian $H_{\rm eff}$ is obtained for this regime.

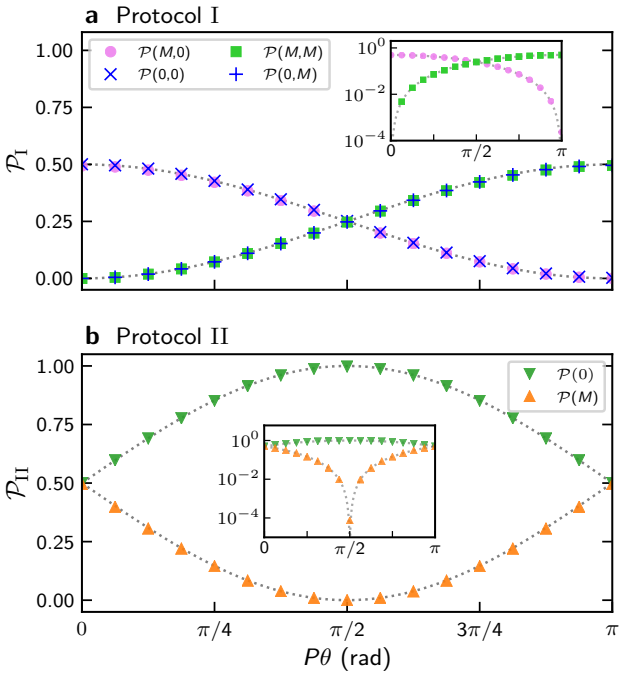

Figure 3. Readout probabilities for Protocols I and II. Comparison between analytic and numerically-calculated probabilities for parameters of Set 1 (as in Figure 2) for different values of $P\theta$. **a** Results for Protocol I. The pink dot and the blue "x" (green square and the blue "+") depict the probabilities of measuring $r=0$ ($r=M$) during the readout, having measured $r=M$ or $r=0$ in step (iii) respectively. **b** Results for Protocol II. The probabilities of measuring $N_3=0$ ($N_3=M$) in the readout are shown as green (orange) triangles. The dotted line depicts the analytic predictions of the probabilities with respect to $P\theta$. The insets show the accordance between predicted and calculated probabilities in semilogarithmic scale.

For an initial Fock state $|M-l,P-k,l,k\rangle$, with total boson number $N=M+P$, the effective Hamiltonian is a simple function of the conserved operators with the form

$$H_{\rm eff} = (N+1)\Omega(Q_1+Q_2) - 2\Omega Q_1 Q_2, \qquad (6)$$

where $\Omega = J^2/(4U((M-P)^2-1))$ and $U=(U_{12}-U_0)/4$. This result is valid for $J \ll U|M-P|$, and it is this inequality that we use to define the resonant tunneling regime.

A very significant feature is that, for time evolution under $H_{\rm eff}$, both $N_1+N_3=M$ and $N_2+N_4=P$ are constant. The respective $(M+1)$-dimensional subspace associated with sites 1 and 3 and $(P+1)$-dimensional subspace associated with sites 2 and 4 provide the state space for the relevant energy band (see Supplementary Note 1). Restricting to these subspaces and using the effective Hamiltonian (6) yields a robust approximation for (2).

Physical proposal

We propose a physical construction, consisting of dysprosium ^{164}Dy atoms trapped in an optical lattice, to test the theoretical results. The trapping is accomplished by employing two sets of counterpropagating laser beams with wavelength $\lambda = 0.532$ μm and waist w_0, with $w_0 \gg \lambda$. We consider each set of beams to cross with the other at an angle of 90° (cyan beams in Fig. 5) , generating a square, two-dimensional optical lattice, in which the distance between nearest wells is $l = \lambda/2 = 266$ nm. We also consider a Gaussian beam propagating towards the **z**-direction (blue beam in Fig. 5), with $\lambda = 0.532$ μm and waist $w_1 = 1.0$ μm, aligned to the center of a four-site square plaquette, to isolate it from the rest of the lattice. Then, to achieve a pancake-shaped trap, it is necessary to include a set of two beams with $\lambda = 0.532$ μm and waist $w_2 \sim w_0$, whose orientations are disposed at an angle of $\alpha = 60°$ from each other (orange beams in Fig. 5), inducing a trapping aspect ratio of $\kappa^2 \equiv \omega_z/\omega_\mathrm{r} = 1.464$. Together, they generate the potential $V(\mathbf{r})$:

$$V(\mathbf{r}) = \frac{1}{2}m\omega^2(x^2+y^2) + \frac{1}{2}m\omega_z^2 z^2 + V_0 \sin^2\left[k\left(x-\frac{l}{2}\right)\right] + V_0\sin^2\left[k\left(y-\frac{l}{2}\right)\right], \tag{7}$$

where m is the atom's mass, $\omega_\mathrm{r} = \sqrt{\frac{2}{m}\left(V_0k^2 + \frac{2V_1}{w_1^2}\right)}$ and

$$\omega_z = \sqrt{\frac{2}{m}\left(\frac{\pi^2 V_2}{d_{sw}^2} + \frac{V_1}{R_1^2}\right)}, \qquad R_k = \frac{\pi w_k^2}{\lambda}$$

are, respectively, the radial and transverse trapping frequencies. Above, $\omega = \sqrt{4V_1/(mw_1^2)}$ arises due to the isolation of the four-well system from the optical lattice. The values $V_1 = V_0$ and $V_2 = 9V_0$ are, respectively, the central beam's and the **x-z** crossing beam's potential depths, V_0 is the 2D lattice potential depth, l is the distance between nearest sites, $k = 2\pi/\lambda$ is the wave number, and $d_\mathrm{sw} = \lambda/(2\sin(\alpha/2))$ is the distance between nearest wells along the **z**-axis. Since we are considering $\alpha = 60°$, the minimum distance between the system's horizontal layer and the next upper (or lower) layer is $d_\mathrm{sw} = 2l = \lambda$, which makes irrelevant the tunneling contributions between different horizontal layers.

To establish equivalency between $V(\mathbf{r})$ and the Hamiltonian of Eq. (2), we employ the standard second-quantization procedure. From this, we calculate the on-site interaction parameter U_0 as:

$$U_0 = U_\mathrm{contact} + U_\mathrm{dip} = \frac{\kappa\eta^3}{\pi^3}\left(g - \frac{C_\mathrm{dd}}{3}f(\kappa)\right), \tag{8}$$

where κ is related to the trapping (pancake) shape aspect, $\eta \equiv m\omega_\mathrm{r}/(2\hbar)$, $g \equiv 4\pi\hbar^2 a/m$, with a being the s-wave scattering length (tunable via Feshbach Resonance), $C_\mathrm{dd} \equiv \mu_0\mu_1^2$ is the coupling constant, where μ_0 is the vacuum magnetic permeability, μ_1 is the atomic magnetic moment, and $f(\kappa)$ is a function that describes how the dipolar interaction behaves for different geometries (encoded in κ)[38]. Taking site 1 as the "starting point', the parameter $U_{1\mathrm{j}}$, which accounts for the dipole-dipole interaction between atoms at sites 1 and j, is expressed as:

$$U_{1\mathrm{j}} = \frac{C_\mathrm{dd}}{4\pi}\int_0^\infty \mathrm{d}r\; r\exp\left(-\frac{r^2}{4\eta}\right)J_0(rd_{1\mathrm{j}})Z(r), \tag{9}$$

$$Z(r) = \left(\frac{4}{3}\sqrt{\frac{\kappa^2\eta}{\pi}} - r\exp\left(\frac{r^2}{4\kappa^2\eta}\right)\mathrm{erfc}\left(\frac{r}{2\sqrt{\kappa^2\eta}}\right)\right),$$

where J_0 is the Bessel function of first kind, $d_{1\mathrm{j}} = l/\delta$, if $j = 2, 4$, and $d_{1\mathrm{j}} = l\sqrt{2}/\delta$, if $j = 3$. Here, the on-site dipolar interaction is given by $U_\mathrm{dip} = \lim_{d_{ij}\to 0} U_{1\mathrm{j}} \propto f(\kappa)$. The term $\delta = 1 + 2V_1/(V_0k^2w_1^2)$ arises when isolating the four-site region from the rest of the lattice, which causes the wells to slightly approach each other.

Integrability condition

The physical setup above is able to simulate the EBHM. To achieve NOON-state generation, however, relies on the particular case for which the EBHM is integrable; as explained previously, this can be accomplished by making $U_0 = U_{13}$, which we call the "integrability condition". The approach is to first choose a value for the s-wave scattering length via Feshbach Resonance. Then, from the condition just stated, one has to adjust ω_r by varying the laser beams intensities[40] such that, at some point, U_0 becomes the same as U_{13}. From this point every Hamiltonian parameter is evaluated only after the integrability condition is satisfied, which sets the intensity of the trapping scheme.

By considering $a = -21$ (-20.85) a_0, the system becomes integrable at $\omega_\mathrm{r} \approx 2\pi \times 37.078$ $(2\pi \times 31.610)$ kHz, as is depicted in Fig. 4. This frequency implies on a 2D-lattice depth of $V_0 \approx 18.495E_\mathrm{R}$ $(13.443E_\mathrm{R})$, where $E_\mathrm{R}/\hbar = \hbar(k\pi)^2/(2ml^2) = 26.894$ kHz is the recoil energy, which characterizes a deep lattice. This allows for a higher stabilization of the system with a negative value for the s-wave scattering length[41]. Then, by using this trapping frequency to calculate the Hamiltonian parameters, one finds $U/\hbar \approx 75.876$ (76.519) Hz and $J/\hbar \approx 24.886$ (73.219) Hz. It is also important to highlight that the tunneling parameter J_{13} between diagonal sites (1-3 and 2-4), which is not included in the Hamiltonian (2), is very small if compared to J. From this, one infers that the tunneling between different horizontal layers of the optical lattice is even smaller, since the distance between these

layers is bigger than the distance between diagonal sites by a factor of $\sqrt{2}$.

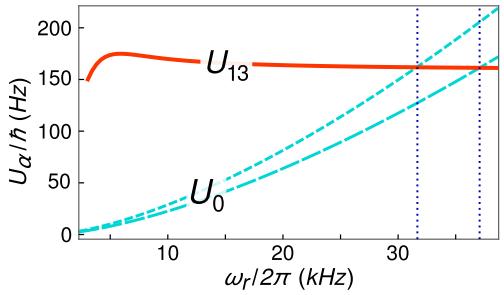

Figure 4. Fulfillment of integrability condition. The s-wave scattering length value is set, following by a variation of the radial trapping frequency ω_r up to the point at which $U_0 = U_{13}$, corresponding to the frequency required for the system to be integrable. The long dashed, short dashed and solid lines depict U_0 for $a = -21\ a_0$ and $a = -20.85\ a_0$ and U_{13}, respectively, for different values of ω_r. By setting $a = -21\ a_0$ ($-20.85\ a_0$), we find $\omega_r \approx 2\pi \times 37.078$ kHz (31.610 kHz) as the frequency for integrability, which results in $U_0/\hbar = U_{13}/\hbar \approx 161.282$ Hz (161.797 Hz). The points where $U_0 = U_{13}$ and the corresponding frequencies ω_r are highlighted by the dotted lines. The system is robust for small deviations from the integrable point (see Supplementary Note 4 for more details).

Breaking of integrability

To produce a controllable breaking of integrability, it is sufficient to consider a second **z**-oriented Gaussian beam (green beam in Fig. 5), weaker than the one used for the region isolation, with waist $w_b \sim 5\ \mu$m and wavelength $\lambda = 0.532\ \mu$m. This beam is displaced by Δx and Δy (with $|\Delta x|=|\Delta y|$) from the center of the four-well system. When the laser is turned on, it implements the terms

$$\nu = \frac{2V_b l}{w_b^2 \delta}(\Delta x + \Delta y), \qquad \mu = \frac{2V_b l}{w_b^2 \delta}(\Delta x - \Delta y), \qquad (10)$$

where $V_b = 5 \times 10^{-3} V_0$ is the potential depth generated by the second beam. For $|\Delta x| = |\Delta y| = 0.2\ \mu$m and the previously obtained radial trapping frequency, the parameters μ and ν can (non-simultaneously) assume the value of 20.870 (15.168) Hz. Therefore, considering $M = 4$ and $P = 11$, one should vary t_μ from 0 to ~ 0.007 (0.009) s to encode $P\theta$ from 0 to π. Also, from the condition $2\nu t_\nu/\hbar = \pi/(2M)$, $t_\nu \sim 0.009$ (0.013)s.

An alternative physical setup is one designed to generate many copies of disconnected four-site plaquettes. This can be realized by overlapping two square optical lattices, each one with lattice spacing determined through different wavelengths (λ and 2λ)[42]. By changing the relative phase, the breaking of integrability can be simultaneously controlled in all copies of the four-site plaquettes.

Discussion

We have offered new techniques to address the highly challenging problem of designing a framework to facilitates NOON state creation. Our approach employs dipolar atoms confined to four sites of an optical lattice. The setup allows for the interactions to be tuned, and to fix the couplings in such a way that the system is integrable. At these couplings, and for controlled perturbative breaking of the integrability, the theoretical properties of the system become very transparent.

The insights gained from integrability allowed us to develop two protocols. Protocol I employs a local measurement procedure to produce NOON states with slightly higher fidelities, over a shorter time, than Protocol II. However Protocol I is probabilistic, requiring post-selection on the measurement outcome. This is in contrast to the deterministic approach of Protocol II. For both protocols, phase-encoding is performed by breaking the system's integrability, in a controllable fashion, at specific moments during the time evolution. And in both protocols the output states were shown to have high-fidelity in numerical simulations. We also identifed a readout scheme, by converting encoded phases into a population imbalance, that allows verification of NOON state production through measurement statistics.

The approaches we have described, that are based on the formation of an uber-NOON state en route to the final state, have two significant advantages. One is that the evolution time does not scale with the total number of particles. Instead, it is only dependent on the difference in particle number of subsystem A and B in the Fock-state input. The other advantage is that all measurements are made in the local Fock-state basis.

We conducted an analysis of the feasibility of a physical proposal. It was demonstrated that the long-range interaction between dipolar atoms allows for an integrable coupling to be achieved, depending on the interplay between contact and dipolar interactions. Through the second-quantization procedure the values for the Hamiltonian parameters were provided, derived by numerical calculations. These are seen to be realistic both in the context of optical-lattice setups and in comparison to literature. We also outlined a procedure to improve the system's robustness with respect to error perturbation (see Supplementary Note 4 for a broader description).

Besides demonstrating the feasibility of NOON state generation, the physical setup we provide can also be employed in the study of thermalization processes and other many-body features of the EBHM. By establishing a link between integrability and quantum technologies, this work promotes advances in the field of neutral-atom quantum information processing.

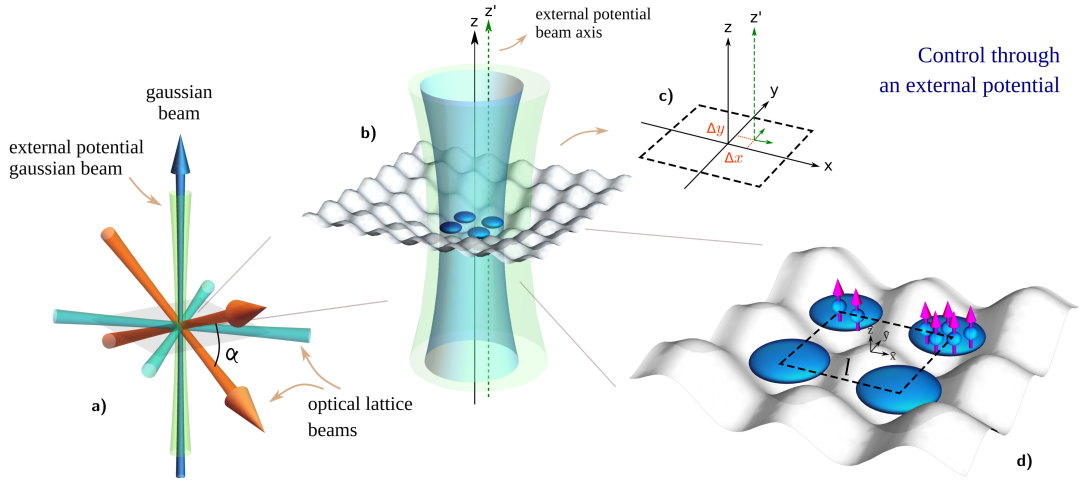

Figure 5. Representation of the trapping scheme. **a** Trapping scheme of the four-well model. In cyan, the two sets of counterpropagating beams are represented, with each set crossing at 90° with the other, providing the two-dimensional lattice trap. In orange, the two beams crossing at an angle of $\alpha = 60°$ are depicted, whose propagation occur in opposite orientations as seen with respect to **z**-axis, resulting in the pancake-shaped potential. In blue, the single laser beam is illustrated, whose waist value is at the typical size of the four-site system, isolating it from the rest of the 2D lattice. The external beam, used for breaking the system's integrability, is depicted in green. **b** Zoom into the region of the lattice which contains the four-well system. The blue beam represents the single laser beam isolating the region of interest from the rest of the lattice. The green beam depicts the external beam, used to controllably break the system's integrability, and the four pancakes illustrate the four wells of the system. **c** The dashed square in the **x-y** plane illustrates the square plaquette formed by the four-well system. The displacement of the central position of the green beam with respect to the center of the four-well system is represented by Δx and Δy, which implement the breaking of the system's integrability. **d** The light grey background represents the trapping potential in the vicinities of the four-well system. The four pancake-shaped wells, at a distance of l between nearest neighbors, are depicted in blue, the cyan spheres illustrate the trapped atoms and the purple arrows represent the aligned dipoles, which induce the dipole-dipole interaction.

Data availability

All relevant data are available on reasonable request from the authors.

References

[1] Lee, H., Kok, P. & Dowling, J.P. A quantum Rosetta Stone for interferometry. *J. Mod. Opt.* **49**, 2325 (2002).

[2] Afek, I., Ambar, Oron & Silberberg, Y. High-NOON states by mixing quantum and classical light. *Science* **328**, 879 (2010).

[3] Bollinger, J.J., Itano, W. M., Wineland, D. J. & Heinzen, D. J. Optimal frequency measurements with maximally correlated states. *Phys. Rev. A* **54**, R4649(R) (1996).

[4] Boto, A. N. et al. Quantum interferometric optical lithography: exploiting entanglement to beat the diffraction limit. *Phys. Rev. Lett.* **85**, 2733 (2000).

[5] Wildfeuer, C. F., Lund, A. P. & Dowling, J. P. Strong violations of Bell-type inequalities for path-entangled number states. *Phys. Rev. A* **76**, 052101 (2007).

[6] Pan, J.-W. et al. Multiphoton entanglement and interferometry. *Rev. Mod. Phys.* **84**, 777 (2012).

[7] Haas, J. et al. Chem/bio sensing with non-classical light and integrated photonics. *Analyst* **143**, 593-605 (2018).

[8] Rarity, J. G. et al. Two-photon interference in a Mach-Zehnder interferometer. *Phys. Rev. Lett.* **65**, 1348 (1990).

[9] Pryde, G. J. & White, A. G. Creation of maximally entangled photon-number states using optical fiber multiports. *Phys. Rev. A.* **68**, 052315 (2003).

[10] Resch, K. J. et al. Time-Reversal and Super-

Resolving Phase Measurements. *Phys. Rev. Lett.* **98**, 223601 (2007).

[11] Kamide, K., Ota, Y., Iwamoto, S. & Arakawa, Y. Method for generating a photonic NOON state with quantum dots in coupled nanocavities. *Phys. Rev. A* **96**, 013853 (2017).

[12] Soto-Eguibar, F. & Moya-Cessa, H.M. Generation of NOON states in waveguide arrays. *Ann. Phys.* **531**, 1900250 (2019).

[13] Merkel, S. T. & Wilhelm, F. K. Generation and detection of NOON states in superconducting circuits. *New J. Phys.* **12**, 093036 (2010).

[14] Hu, Y.M., Feng, M. & Lee, C. Adiabatic Mach-Zehnder interferometer via an array of trapped ions. *Phys. Rev. A* **85**, 043604 (2012).

[15] Cable, H., Laloë, F. & Mullin, W. J. Formation of NOON states from Fock-state Bose-Einstein condensates. *Phys. Rev. A* **83**, 053626 (2011).

[16] Lewis-Swan, R. J. & Kheruntsyan K. V. Proposal for demonstrating the Hong–Ou–Mandel effect with matter waves. *Nat. Commun.* **5**, 3752 (2014).

[17] Cirac, J. I., Lewenstein, M., Mölmer, K. & Zoller, P. Quantum superposition states of Bose-Einstein condensates. *Phys. Rev. A* **57**, 1208 (1998).

[18] Bychek, A. A., Maksimov, D. N. & Kolovsky, A. R. NOON state of Bose atoms in the double-well potential via an excited-state quantum phase transition. *Phys. Rev. A* **97**, 063624 (2018).

[19] Vanhaele, G. & Schlagheck, P. NOON states with ultracold bosonic atoms via resonance- and chaos-assisted tunneling. arXiv:2008.12156.

[20] Góral, K., Santos, L. & Lewenstein, M. Quantum phases of dipolar bosons in optical lattices. *Phys. Rev. Lett.* **88**, 170406 (2002).

[21] Tonel, A. P., Ymai, L. H., Foerster, A. & Links, J. Integrable model of bosons in a four-well ring with anisotropic tunneling. *J. Phys. A: Math. Theor.* **48**, 494001 (2015).

[22] Kinoshita, T., Wenger, T. & Weiss, D. S. A quantum Newton's cradle. *Nature* **440**, 900-903 (2006).

[23] Liao, Y. et al. Spin-imbalance in a one-dimensional Fermi gas. *Nature* **467**, 567-569 (2010).

[24] Pagano, G. et al. A one-dimensional liquid of fermions with tunable spin. *Nat. Phys.* **10**, 198-201 (2014).

[25] Batchelor, M. T. & Foerster, A. Yang–Baxter integrable models in experiments: from condensed matter to ultracold atoms. *J. Phys. A: Math. Theor.* **49**, 17 (2016).

[26] Yang, B. et al. Quantum criticality and the Tomonaga-Luttinger liquid in one-dimensional Bose gases. *Phys. Rev. Lett.* **119**, 165701 (2017).

[27] Breunig, O. et al. Quantum criticality in the spin-1/2 Heisenberg chain system copper pyrazine dinitrate. *Science Adv.* **3**, 12 (2017).

[28] Wang, Z. et al. Experimental observation of Bethe strings. *Nature* **554**, 219-223 (2018).

[29] Pilatowsky-Cameo, S. et al. Positive quantum Lyapunov exponents in experimental systems with a regular classical limit. *Phys. Rev. E* **101** 010202(R) (2020).

[30] Yao, N.Y. et al. Bilayer fractional quantum Hall states with ultracold dysprosium. *Phys. Rev. A* **92**, 033609 (2015).

[31] Baier, S. et al. Extended Bose-Hubbard models with ultracold magnetic atoms. *Science* **352**, 6282 (2016).

[32] Grün, D. S., Wittmann W. K., Ymai, L. H., Tonel, A. P., Foerster, A. & Links, J. Integrable atomtronic interferometry. arXiv:2004.11987.

[33] Yamamoto, R. et al. Site-resolved imaging of single atoms with a Faraday quantum gas microscope. *Phys. Rev. A* **96**, 033610 (2017).

[34] Schäfer, F., Fukuhara, T., Sugawa, S., Takasu, Y. & Takahashi, Y. Tools for quantum simulation with ultracold atoms in optical lattices. *Nat. Rev. Phys.* **2**, 411-425 (2020).

[35] Nielsen, M. A. & Chuang, I. L. *Quantum Computation and Quantum Information.* (Cambridge Univ. Press, 2010).

[36] Gibbons, M. J., Kim, S. Y., Fortier, K. M., Ahmadi, P., & Chapman, M. S. Achieving very long lifetimes in optical lattices with pulsed cooling. *Phys. Rev. A* **78**, 043418 (2008).

[37] Wilsmann, K. W., Ymai, L. H., Tonel, A. P., Links, J. & Foerster, A. Control of tunneling in an atomtronic switching device. *Comm. Phys.* **1**, 91 (2018).

[38] Lahaye, T., Menotti, C., Santos, L., Lewenstein, M. & Pfau, T. The physics of dipolar bosonic quantum gases. *Rep. Prog. Phys.* **72**, 126401 (2009).

[39] Tonel, A.P., Ymai, L. H., Wilsmann, K. W., Foerster, A. & Links, J. Entangled states of dipolar bosons generated in a triple-well potential. *SciPost Phys. Core* **2**, 003 (2020).

[40] Bloch, I. Ultracold quantum gases in optical lattices. *Nat. Phys.* **1**, 23-30 (2005).

[41] Müller, S. et al. Stability of a dipolar Bose-Einstein condensate in a one-dimensional lattice. *Phys. Rev. A* **84**, 053601 (2011).

[42] Dai, H.-N. et a. Four-body ring-exchange interactions and anyonic statistics within a minimal toric-code Hamiltonian. *Nat. Phys.* **13**, 1195 (2017).

Acknowledgements

D.S.G. and K.W.W. were supported by CNPq (Conselho Nacional de Desenvolvimento Científico e Tecnológico), Brazil. A.F. acknowledges support from CNPq - Edital Universal 430827/2016-4. A.F. and J.L. received funding from the Australian Research Council through Discovery Project DP200101339. J.L. acknowledges the traditional owners of the land on which The University of Queensland operates, the Turrbal and Jagera people. We thank Ricardo R. B. Correia and Bing Yang for helpful discussions.

Author contributions

All authors contributed to the conceptualization of the project, and actively engaged in the writing of the manuscript. D.S.G, K.W.W. and L.H.Y. implemented the theoretical analyses of the model, detailed the physical proposal, and processed the numerical computations. J.L. and A.F. designed the research framework, and directed the program of activities.

Supplementary Note 1: Energy bands and effective Hamiltonian

Here we give an overview of the origin for the effective Hamiltonian. Recall that the integrability condition is $U_{13} = U_{24} = U_0$ and $U_{12} = U_{23} = U_{34} = U_{14}$. When $J = 0$, the Fock state $|M-l, P-k, l, k\rangle$ is eigenstate of the Hamiltonian (2) with energy

$$E = C - U(M-P)^2 \tag{S.1}$$

where $C = (U_0+U_{12})N^2/4 - U_0/2$. The result is independent of l and k, indicating degeneracies. For small values of J, the degeneracies are broken and lead to energy levels in well-defined bands, each with $2(M+1)(P+1)$ energy levels, except for N even, where the band with the highest energy, $M = P$, will have $(M+1)(P+1)$ levels. The level energy structure of the case we are analyzing, with $N = 15$, is shown in Supplementary Figure 1. In it, we highlight in cyan the band with $M = 4$ and $P = 11$ (and vice versa), while the vertical lines marks the two sets of parameters pointed in the main text (repeated here, expressed in Hz):

Set 1: $\{U/\hbar = 75.876,\ J/\hbar = 24.886,\ \mu/\hbar = 20.870\}$;
Set 2: $\{U/\hbar = 76.519,\ J/\hbar = 73.219,\ \mu/\hbar = 15.168\}$.

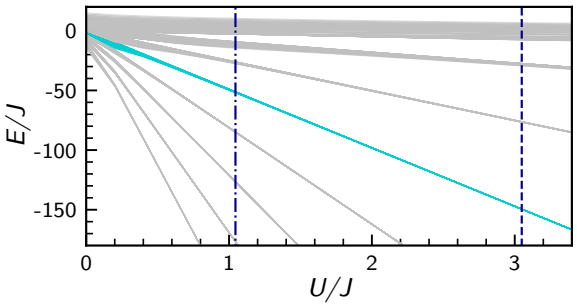

Supplementary Figure 1. Energy band formation. Dimensionless energy eigenvalues E/J as a function of dimensionless coupling U/J, where $U = (U_{12} - U_0)/4$ and considering $C = 0$ in (S.1). The dashed vertical line marks $U/J \sim 3$ (concerning parameter Set 1) and the dot-dashed line marks $(U/J \sim 1)$ (concerning parameter Set 2), while cyan depicts the band containing the expectation energy of the initial state $|\Psi_0\rangle = |4, 11, 0, 0\rangle$. The formation of the bands is due to the quadratic dependence of $(M-P)$ in the energy (S.1).

An effective Hamiltonian for each band is obtained by consideration of second-order processes. Associated to labels M and P, such that $N = M + P$, we obtain

$$\begin{aligned}
H_{\text{eff}} = &\frac{J^2}{16U(M-P+1)}\left(a_1a_3^\dagger + a_3a_1^\dagger\right)\left(a_2^\dagger a_2 + a_4^\dagger a_4\right)\\
&+\frac{J^2}{16U(M-P+1)}\left(a_1a_1^\dagger + a_3a_3^\dagger\right)\left(a_2^\dagger a_4 + a_4^\dagger a_2\right)\\
&-\frac{J^2}{16U(M-P-1)}\left(a_2a_2^\dagger + a_4a_4^\dagger\right)\left(a_1^\dagger a_3 + a_3^\dagger a_1\right)\\
&-\frac{J^2}{16U(M-P-1)}\left(a_2a_4^\dagger + a_4a_2^\dagger\right)\left(a_1^\dagger a_1 + a_3^\dagger a_3\right)\\
&+\frac{J^2}{16U}\left(\frac{1}{M-P+1} - \frac{1}{M-P-1}\right)\\
&\times\left(a_1^\dagger a_2 a_3 a_4^\dagger + a_1^\dagger a_2^\dagger a_3 a_4 + a_1 a_2^\dagger a_3^\dagger a_4 + a_1 a_2 a_3^\dagger a_4^\dagger\right).
\end{aligned}$$

For a given initial Fock state, the resonant regime is achieved when the expectation energy lies in a region characterized by an energy band. There, the values of the integrability-breaking parameters μ, ν may be as large as the band-separation allows, which is depicted in Supplementary Figure 2.

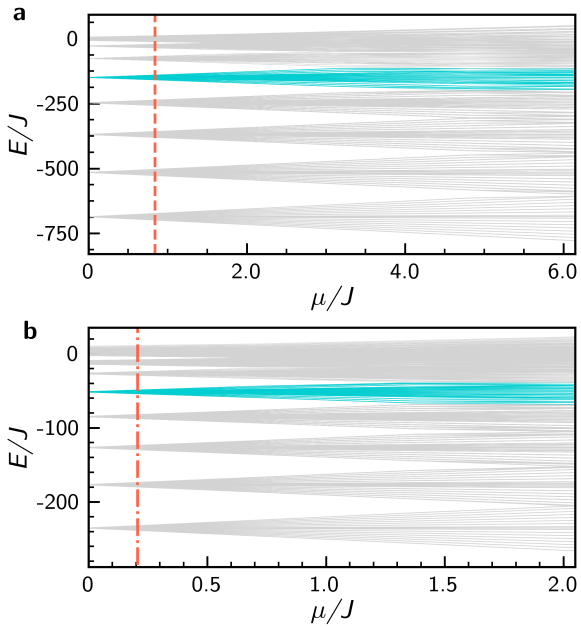

Supplementary Figure 2. Energy bands for broken integrability. Four-well model energy distribution for the two sets of parameters U and J, as in the main text. **a** Set 1: $U/J \sim 3$ and **b** Set 2: $U/J \sim 1$. The vertical lines indicate the respective integrability-breaking parameters $\mu/\hbar = 20.870$ Hz (**a**) and $\mu/\hbar = 15.168$ Hz (**b**). The cyan lines represent the energy band associated to the initial state $|\Psi_0\rangle = |4, 11, 0, 0\rangle$.

Supplementary Note 2: Probabilities and fidelities

Supplementary Table 1 shows the measurement probabilities of Protocol I, as well as the fidelity of the resulting state with the respective NOON state, for $M = 4$, $P = 11$ and the two aforementioned sets of parameters. The resulting NOON state from Protocol I can be either symmetric ($r = 0$) or antisymmetric ($r = M$). For intermediate values for the outcome of measuring N_3, we calculate the fidelity of the resulting state with the symmetric NOON state ($r = 0, 1$) or the antisymmetric state ($r = 2, 3, 4$), respectively.

Protocol I:

Set 1

	Phase ($P\theta$)											
Measurement	0		$\pi/6$		$\pi/4$		$\pi/3$		$\pi/2$		π	
r	$\mathcal{P}(r)$	F_{I}	$\mathcal{P}(r)$	F_{I}	$\mathcal{P}(r)$	F_{I}	$\mathcal{P}(r)$	F_{I}	$\mathcal{P}(r)$	F_{I}	$\mathcal{P}(r)$	F_{I}
0	0.5009	0.9977	0.5009	0.9977	0.5009	0.9978	0.5009	0.9978	0.5009	0.9977	0.5009	0.9978
1	0.0006	0.0488	0.0006	0.0489	0.0006	0.0494	0.0006	0.0499	0.0006	0.0501	0.0006	0.0512
2	0.0003	0.0164	0.0003	0.0160	0.0003	0.0155	0.0003	0.0162	0.0003	0.0169	0.0003	0.0155
3	0.0013	0.0447	0.0013	0.0450	0.0013	0.0452	0.0013	0.0453	0.0013	0.0454	0.0013	0.0463
M=4	0.4956	0.9996	0.4957	0.9996	0.4956	0.9996	0.4956	0.9996	0.4957	0.9996	0.4957	0.9996

Set 2

	Phase ($P\theta$)											
Measurement	0		$\pi/6$		$\pi/4$		$\pi/3$		$\pi/2$		π	
r	$\mathcal{P}(r)$	F_{I}	$\mathcal{P}(r)$	F_{I}	$\mathcal{P}(r)$	F_{I}	$\mathcal{P}(r)$	F_{I}	$\mathcal{P}(r)$	F_{I}	$\mathcal{P}(r)$	F_{I}
0	0.4922	0.9642	0.4922	0.9643	0.4922	0.9644	0.4922	0.9644	0.4922	0.9645	0.4923	0.9649
1	0.0097	0.1219	0.0097	0.1221	0.0097	0.1219	0.0097	0.1214	0.0097	0.1221	0.0096	0.1214
2	0.0053	0.0400	0.0053	0.0384	0.0053	0.0378	0.0053	0.0375	0.0053	0.0363	0.0053	0.0320
3	0.0139	0.1336	0.0139	0.1338	0.0139	0.1333	0.0139	0.1332	0.0139	0.1332	0.0139	0.1325
M=4	0.4629	0.9886	0.4631	0.9886	0.4632	0.9887	0.4633	0.9887	0.4635	0.9887	0.4640	0.9888

Supplementary Table 1. Measurement probabilities and NOON state fidelities. Probability of measuring r particles at site 3 of Protocol I, and fidelity of the resulting state with the symmetric NOON state ($r = 0, 1$) or the antisymmetric NOON state ($r = 2, 3, 4$). In this calculation, we employed the parameters Set 1 and Set 2 and considered $M = 4$ and $P = 11$.

Supplementary Note 3: Readout statistics

For less ideal choices of parameters, it is possible to perform a fitting on the readout probabilities amplitudes, such that

$$\text{Protocol I} \begin{cases} \mathcal{P}(0,0) = \mathcal{P}(M,0) = \dfrac{c_{00}}{2}\cos^2\left(\dfrac{P\theta}{2}\right) \\ \mathcal{P}(0,M) = \mathcal{P}(M,M) = \dfrac{c_{MM}}{2}\sin^2\left(\dfrac{P\theta}{2}\right) \end{cases}$$

$$\text{Protocol II} \begin{cases} \mathcal{P}(0) = c_0\sin^2\left(\dfrac{P\theta}{2} - \dfrac{\pi}{4}\right) \\ \mathcal{P}(M) = c_M\cos^2\left(\dfrac{P\theta}{2} - \dfrac{\pi}{4}\right) \end{cases}$$

where c_{00}, c_{MM}, c_0 and c_M are constants that are obtained by fitting the numerically-evaluated data with the analytic models. By choosing the parameters of Set 2, we obtain the following constants from a least-squares fitting: $c_{00} = 0.938$, $c_{MM} = 0.893$, $c_0 = 0.954$ and $c_M = 0.909$. The results are shown in Supplementary Figure 3.

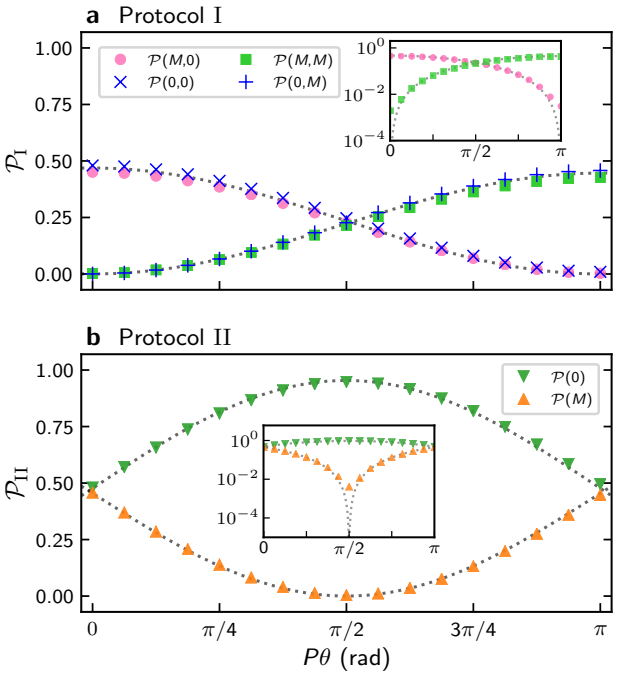

Supplementary Figure 3. Readout probabilities. Comparison between analytic and numerically-calculated probabilities relating to the parameters of Set 2 with $\mu/\hbar = \nu/\hbar = 15.168$ Hz, for different values of $P\theta$. **a)** Probability distributions for measuring $N_3 = 0$ ($N_3 = M$) after time evolution subsequent to Protocol I. **b)** Probability distributions of measuring $N_3 = 0$ ($N_3 = M$) after time evolution subsequent to Protocol II. In both cases, the dotted lines refer to the analytic probabilities adjusted to the numerical points according to the Eqs. (S.2). The coefficients used were $c_{00} = 0.938$, $c_{MM} = 0.893$, $c_0 = 0.954$ and $c = 0.909$. The insets show the accordance between predicted and calculated probabilities in semilogarithmic scale.

Supplementary Note 4: Robustness

Here we analyze the system's robustness in the presence of a perturbation parameter, and outline a method to enhance performance. Supposing that the integrability condition is subject to an error, denoted by ξ:

$$\xi = U_0 - U_{13}. \tag{S.2}$$

We find that the fidelities for the parameters Set 1 are above 0.9 for an error parameter ξ/J up to $\sim 0.01\%$, while the parameter Set 2 is able to produce NOON state with fidelities above 0.9 up to $\xi/J \sim 0.03\%$.

To enhance the fidelity, we propose a procedure that consists of both positive ($+\xi$) and negative ($-\xi$) deviations in Eq. (S.2). This can be done, for instance, by considering a sequence of pulses[1]. This is appropriate when considering an error parameter in the physical setup: after fixing the desired (approximate) s-wave scattering length, the trapping frequency adjustment may not have the required precision, allowing for a minimum-error of $\pm\xi$.

Considering perturbations $H^{\pm}(\mu,\nu)$ of the Hamiltonian, with the form

$$H^{\pm}(\mu,\nu) = H(U^{\pm}, J^{\pm}) + \mu^{\pm}(N_2 - N_4) + \nu^{\pm}(N_1 - N_3) \pm \xi(N_1N_3 + N_2N_4),$$

set $\bar{U}$, $\bar{J}$ and $\bar{\mu}$ as the mean values for the two cases $+\xi$ and $-\xi$. We then calculate the times $t_{\rm m}$ and t_μ from these mean values. Next, running a simulation that alternates $N_{\delta t}$ times between the extreme coupling values during the integrable time evolution over $t_{\rm m} - t_\mu$ leads to an increase in the system's tolerance to the error, as depicted in Supplementary Figure 4.

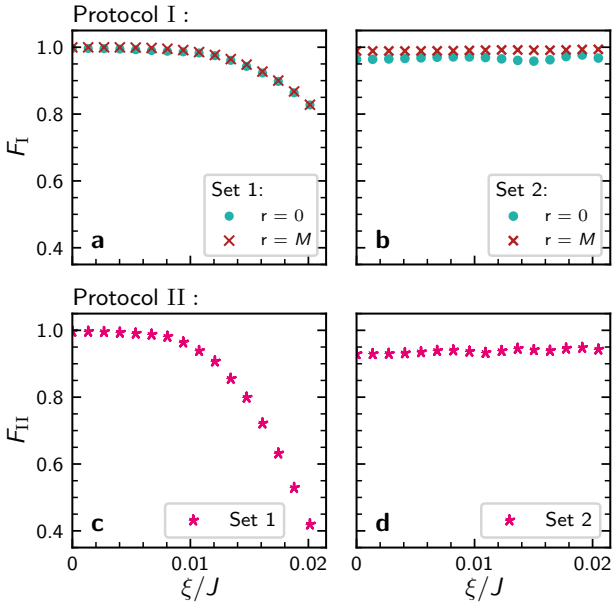

Supplementary Figure 4. Robustness. NOON states fidelities with respect to a perturbation parameter ξ, for Protocols I (panels **a** and **b**) and II (panels **c** and **d**). Panels **a** and **c**: Set 1. Panels **b** and **d**: Set 2. We considered $\nu = \mu$ in Protocol II evaluations. For every ξ, we evaluate the fidelities, with $P\theta = \pi/2$, for the Hamiltonian parameters obtained by solving for $\omega_{\rm r}$ that corresponds to Eq. (S.2) (cf. Figure 4 of the main text). With $N_{\delta t} = 100$ oscillations between $+\xi$ and $-\xi$, NOON states are produced with fidelities higher than 0.9 for ξ/J up to 1.2% on the left, and more than 2.0% on the right.

.

Supplementary Reference

[1] Zhou, X., Jin, S. & Schmiedmayer, J. Shortcut loading a Bose–Einstein condensate into an optical lattice. *New J. Phys.* **20**, 055005 (2018).